Advanced hyperspectral imager design for single-device pansharpening

Timothy Peter Snailham

A thesis submitted in fulfilment of the requirements for the degree of Doctor of Philosophy.

School of Physics
Faculty of Science
The University of Sydney
Australia
February 2026

Supervisors: Prof. Sergio Leon-Saval and Dr. Christopher Betters

Statement of Originality

This is to certify that the content of this thesis is my own work. This thesis has not been submitted for any other degree or purpose.

I certify that the intellectual content of this thesis is the product of my own work, and that all assistance received in preparing this thesis and all sources have been acknowledged.

Timothy Snailham
February 24, 2026

Acknowledgements

This research reported in this thesis was supported by the award of a Research Training Program domestic student fee offset. This research was supported by a scholarship from the CUAVA ARC Training Centre for CubeSats, UAVs and their Applications.

There are many people who helped me along this journey over the past five years, and without all their help I certainly would not have reached this final submission. Firstly I want to thank my faithful supervisors, Chris Betters and Sergio Leon-Saval. Chris was an incredible source of knowledge in both optics and software, and I will always be grateful for the amount of time and effort he put into guiding and correcting my research and writing, especially in my final year. Sergio kept this project on track and made sure I had a full body of thesis-worthy work, with a perfect mixture of tough love and genuine approachability. Iver Cairns was the first person I talked to in relation to this thesis; his infectious enthusiasm won me over and has endured throughout the years. I also express my gratitude for the funding of this project through the CUAVA group and Iver.

Naif Alsalem was a great source of companionship in my early research through COVID, and was an invaluable lab-mate, helping to troubleshoot my numerous issues. He also pushed me back on track at a moment I was certain I would quit and I am forever thankful for that rousing speech in Office 232. I'd like to thank my parents, Lyn and Pete, and sister Kate for their support and willingness to lend an ear to my problems. The prospect of facing "How goes the PhD?" at get-togethers so often spurred me on in troughs of motivation. Thanks to my mates Matt, Jourdon, Joey, Nat, Dave, Hoges, Rhys and Saveen who made me feel like my research was cool and worth doing, which did a lot to get me back to work. Thanks to my cat, Chai, for her unfailing companionship and warmth. And finally my deepest gratitude to my partner Suzie, who patiently listened to every single doubt, complaint, and minor inconvenience I experienced doing this thesis, and always had my back. Over the course of five years, those small bits of juice built a mountain of energy, without which I would not be here.

Author Attribution Statement

This thesis is fully comprised of material not previously published. A paper submission was in-progress but not submitted for this work.

During the preparation of the thesis the author used ChatGPT 5 for the purposes of text enhancement. The use of this generative AI tool includes minor sentence restructuring, and clarity enhancement. The author confirms that, where text was modified by generative AI, the content was reviewed for possible errors, inaccuracies, and bias. The author takes full responsibility for the submitted thesis, confirms that the work is their own, and has used generative AI in accordance with University guidelines and policies.

In addition to the authorship attribution statements above, in cases where I am not the corresponding author of a published item, permission to include the published material has been granted by the corresponding author.

Timothy Snailham
February 24, 2026

As supervisor for the candidature upon which this thesis is based, I can confirm that the authorship attribution statements above are correct.

Sergio Leon-Saval
Lead Supervisor
February 24, 2026

Abstract

Hyperspectral imaging (HSI) provides unparalleled spectral detail for remote sensing, yet accessible pushbroom imagers often suffer from limited or anisotropic spatial resolution. Super-resolution techniques such as pansharpening can address this; by fusing high-resolution panchromatic images with hyperspectral datacubes, however its typical reliance on external, third-party imagery limits flexibility for small-scale research or unique targeting. To overcome these constraints, this thesis presents the design, development, and application of a compact, dual-modality imaging device, integrating both hyperspectral and high-resolution panchromatic sensors. By simultaneously capturing both modalities, the system enables intra-device pansharpening without external datasets. The co-aligned panchromatic sensor also provides a live video feed for region targeting.

The research first explores the optical design of two spectrometers: a custom-lens theoretical model developed to maximise photon throughput and spatial resolution, and a redesign of the open-source OpenHSI architecture, similarly using commercial-off-the-shelf (COTS) components to improve spectral uniformity. The COTS model is physically assembled into a dual-detector setup with custom 3D-printed housing, followed by calibration for wavelength, radiance, and aberration correction. To validate the system, datacubes of contrast targets and natural scenes are captured and processed using a modified Gram-Schmidt Adaptive (GSA) pansharpening algorithm. Comparisons of pre- and post-fusion datacubes confirm significant spatial resolution enhancements while preserving spectral integrity.

This work demonstrates the viability of intra-device pansharpening to deliver high spectral resolution alongside isotropic spatial contrast. The findings establish a scalable, cost-effective pathway for advancing compact, dual-modality hyperspectral imaging technologies.

Contents

List of Figures

List of Tables

Chapter 1

Introduction

1.1 Hyperspectral Imaging

Hyperspectral Imaging (HSI) has its origins in remote sensing technologies developed in the late 1960s and early 1970s, when systems such as the Landsat Multispectral Scanner (MSS) first enabled imaging of the Earth's surface in a small number of discrete spectral bands[1]. This multispectral approach extended conventional RGB imaging, a practice limited to three primary colour channels, adding additional bands for greater spectral information. The distinction between hyperspectral and multispectral is not universally consistent. Some definitions emphasise the presence of contiguous bands, others simply require a higher number of bands than multispectral systems. The shift toward a truly hyperspectral approach (defined here as imaging across many contiguous, narrow spectral bands rather than a limited set of broad multispectral bands) emerged in the 1980s with airborne instruments such as NASA's Airborne Imaging Spectrometer (AIS)[2] and later the Airborne Visible/Infrared Imaging Spectrometer (AVIRIS)[3]. These pioneering systems demonstrated the capacity to classify and discriminate surface materials based on subtle spectral differences, establishing the foundation of imaging spectroscopy as a discipline[4].

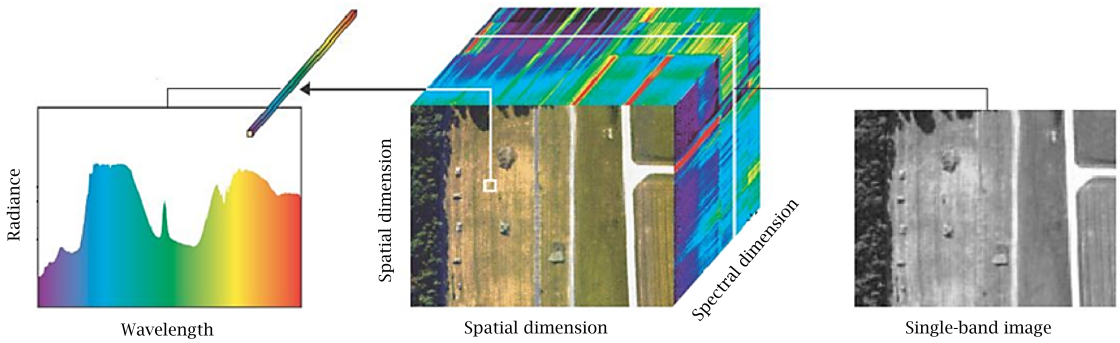

Figure 1.1: The basic structure of a hyperspectral datacube. Adapted from Wang et al. 2020[5].

1.1.1 Nomenclature

Spatial resolution describes the fineness of detail captured in the scene, determined by the portion of the scene imaged onto each pixel. It is shaped by optical design, detector pitch, and the datacube acquisition method, which varies by imaging modality.

Spectral resolution refers to the narrowness of each wavlength measurement band, typically measured in nanometres, and is governed by slit width, grating dispersion, focal length, and detector pixel pitch.

Across-track refers to the spatial dimension aligned with the slit of a pushbroom spectrometer. Each detector column samples a strip of the scene simultaneously, so across-track resolution is fixed by pixel pitch and optical magnification.

Along-track denotes the spatial dimension built by platform motion in a pushbroom system. Resolution depends on slit width, integration time, and platform velocity, with motion blur further degrading dimensional sharpness.

Ground Sampling Distance (GSD) is the projected size of one pixel on the ground, usually expressed in metres. In pushbroom sensors, GSD is defined separately for across-track (optics and pixel pitch) and along-track (slit projection and motion parameters).

Signal-to-Noise Ratio (SNR) expresses the relative strength of the measured signal to background noise. In HSI it depends on detector quantum efficiency, slit width, illumination, and integration time, and is often wavelength dependent.

Instantaneous Field of View (iFOV) is the angular extent of the scene viewed by a single detector element. In pushbroom imagers, the across-track iFOV sets spatial sampling per pixel, while along-track iFOV is determined by the projected slit height.

Field of View (FOV) is the total angular span of the imaged scene. For pushbroom systems, the FOV corresponds to the angular coverage across the slit and determines the swath width on the ground.

Pixel swath describes the physical ground width imaged by the full detector array in one pushbroom line. It is the product of the across-track GSD and the number of pixels across the detector.

1.1.2 HSI Fundamentals

A hyperspectral imager captures reflected or emitted light across a large number of contiguous spectral bands, producing a three-dimensional datacube with two spatial and one spectral dimension. Many instruments implement this through a spectrograph, consisting of a telescope or field lens for light collection, collimating optics to ensure parallel propagation, a dispersive element such as a prism or diffraction grating, focusing optics, and a detector array [6]. The dispersive element separates incoming light into its constituent wavelengths, which are then projected onto the detector such that each spatial pixel along the slit dimension contains a full spectral profile. Alternative architectures, such as tunable-filter imagers and pixel-level filter arrays, achieve the same outcome through different optical layouts but share the principle of recording a signature spectrum for each spatial location [7].

A fundamental challenge in hyperspectral imaging is balancing spectral and spatial resolution. Narrower bands allow finer discrimination of spectral signatures, for example detecting trace atmospheric gases with narrow absorption features [8]. Higher spatial resolution enables discrimination of small structures across diverse domains, such as areas of unique vegetation or tissue morphology[9]. These gains must also be balanced against signal-to-noise ratio (SNR), since spectral resolution, spatial resolution, and photon throughput all compete for the same detector real estate.

Since early developments, HSI has advanced significantly in both spectral and spatial resolution. Early instruments suffered from low detector sensitivity, narrow spectral range, and modest spatial resolution. Improvements in detector technology enabled finer spectral sampling and higher sensitivity across broader ranges of the electromagnetic spectrum[10]. Parallel progress in optical engineering, particularly efficient reflective and transmission gratings, further refined the ability to resolve adjacent wavelengths[6]. Trade-offs between spatial fidelity and swath coverage have also become fundamental in remote sensing, with different configurations optimised either for fine-scale analysis or wide-area surveys[11]. The resulting increase in discrimination capability, combined with reductions in instrument size and weight, expanded operational platforms and applications from airborne systems such as AVIRIS to compact designs for field deployment[12]. Today, hyperspectral imaging supports disciplines ranging from precision agriculture[13] to environmental monitoring [14] and medical diagnostics[15].

1.1.3 Pushbroom Imagers

Pushbroom hyperspectral imagers acquire datacube slices consisting of one spatial dimension and the full spectral dimension, recorded line by line. The second spatial dimension is built sequentially as the platform advances. This mode of operation is highly photon-efficient and supports fine spectral sampling, which is why pushbroom instruments such as AVIRIS dominate airborne and satellite-based Earth observation[16].

Spatial resolution in pushbroom systems is defined separately in the two spatial dimensions. Across-track resolution is governed by the instantaneous field of view (iFOV) of each detector element, set by pixel pitch and optical magnification. Along-track resolution is linked to the iFOV imposed by the projected slit width, and is affected by platform velocity and integration time, which together determine both the spacing and sharpness of successive image lines. Longer integration times and fast motion can increase the spacing of successive lines and the effect of motion blur, reducing effective along-track resolution[6], [18]. In practice, the degree of anisotropy depends on system design. For most accessible instruments such as OpenHSI, where the slit is wider than the detector pixel pitch, across-track sampling is finer than along-track, producing images where spatial detail is noticeably sharper across-track than along-track. This anisotropy distorts fine structures and limits the reliability of quantitative analyses.

Imbalance in spatial fidelity is a fundamental drawback of the architecture and a central motivation for this thesis. Greater spatial resolution in pushbroom imagers would improve boundary detection, sharpen small-object identification, and increase the reliability of quantitative mapping in Earth observation applications. By

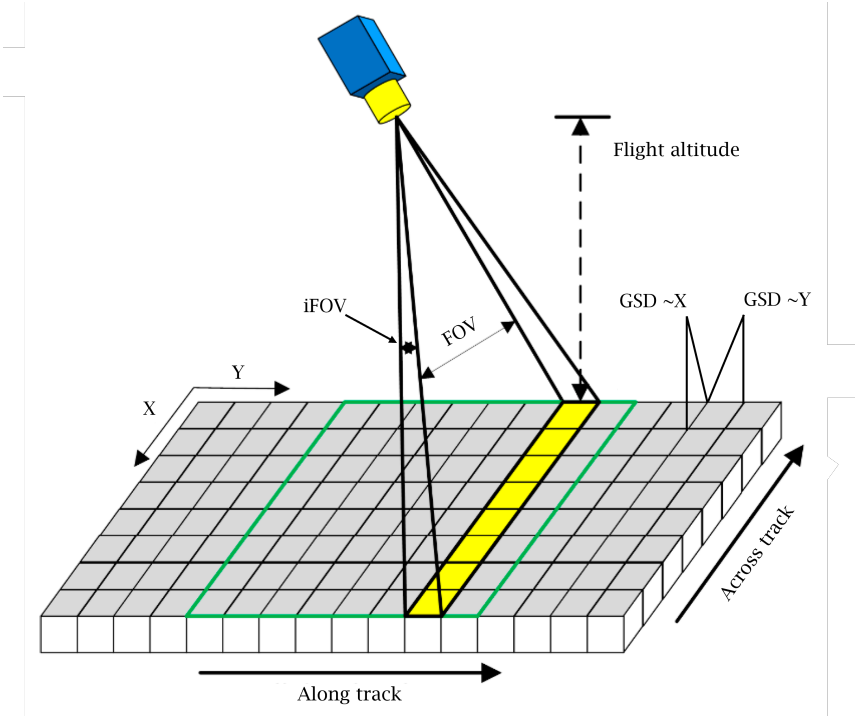

Figure 1.2: The operating function of a pushbroom hyperspectral imager showing the angles of iFOV and FOV. Adapted from Wang et al. 2024[17].

combining two imaging modalities (hyperspectral datacubes and 2D high-definition panchromatic images) into one device, this body of research aims to enhance along-track sampling through data fusion.

1.1.4 Optical Design Considerations

Hyperspectral imager design is defined by trade-offs between spatial fidelity, spectral resolution, and throughput. Systems demanding high spatial accuracy require complex optics with minimal aberrations, while those prioritising spectral coverage or light efficiency adopt simplified layouts such as Offner designs[19]. Operation under low-light conditions adds further constraints, where high-quantum-efficiency detectors, large apertures, and cooled arrays extend sensitivity at the cost of portability and simplicity[20], [21].

Balancing spectral and spatial resolution is a core design challenge. Narrower bands improve spectral discrimination but reduce photon counts per channel, requiring longer integration times and slowing acquisition[3]. Higher spatial resolution requires smaller detector elements or stronger magnification, which reduces throughput and SNR[18]. Detector real estate compounds this balance: for a fixed array, allocating more pixels to spatial sampling leaves fewer for the spectral dimension, and vice versa. As a result, imagers are positioned along different points of this trade space rather than achieving both extremes simultaneously[22]. These limits motivate approaches that enhance spatial detail without sacrificing spectral coverage, such as pansharpening data fusion techniques.

These optical considerations are mirrored by device-level trade-offs. Larger apertures and longer focal lengths improve resolution and throughput but increase foot-

print, weight, and power requirements, limiting deployment on UAVs or handheld platforms[19]. Extending spectral range into the SWIR or thermal infrared requires cooled detectors, further raising system complexity and cost[23]. Commercial hyperspectral imagers such as the Headwall Nano-Hyperspec achieve high performance but at costs prohibitive for many research groups[24]. At the opposite end, DIY (Do-It-Yourself) and COTS (Commercial off-the-shelf)-based systems such as OpenHSI[25] offer accessibility and reduced cost by using commercially available and 3D-printed components through the assembly. Opting for cheaper, openly available components often impacts spatial/spectral resolution or SNR, but devices can be more easily tailored to specific applications. This thesis builds on the latter category, aiming to extend the capability of a COTS-based design by integrating panchromatic fusion to address anisotropy and enhance spatial performance.

1.2 Pansharpening

Pansharpening is an image fusion technique used to enhance the spatial resolution of multispectral or hyperspectral data by integrating them with high-resolution panchromatic images. It emerged to address the coarse spatial sampling of early multispectral sensors such as Landsat, which offered broad spectral coverage but limited detail[26], [27]. By combining the dense spectral information of hyperspectral or multispectral data with the fine spatial sampling of panchromatic images, pansharpening produces composite imagery that retains spectral fidelity while achieving sharper spatial detail[28], [29]. This fusion is possible because of the spectral overlap between modalities, allowing the high-resolution spatial content to be correlated with and injected into the spectral data. The central challenge is then to sharpen spatial detail without distorting spectral signatures[30], [31].

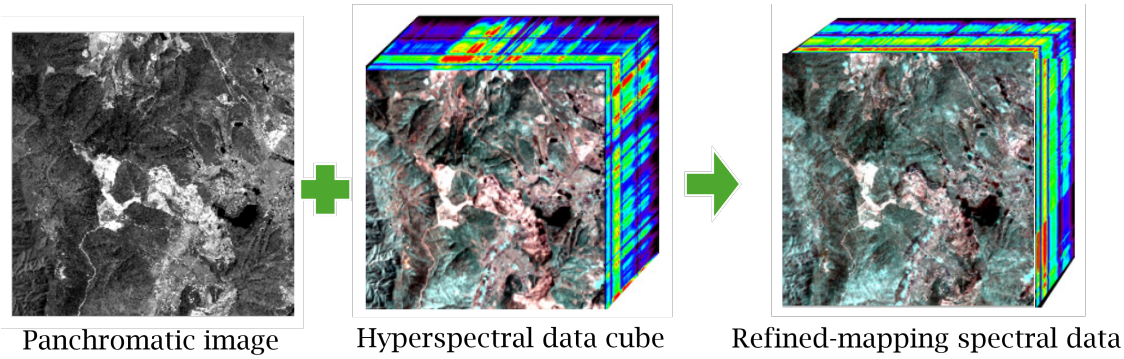

Figure 1.3: Simple schematic of pansharpening data fusion.

Although originally developed for multispectral satellites, pansharpening remains relevant for modern hyperspectral systems. Pushbroom imagers continue to face anisotropic resolution in many applications where higher spatial sampling is a key performance metric. Fusion with high-resolution panchromatic data can mitigate this imbalance, improving isotropy and enabling more reliable mapping and classification.

Integrating pansharpening into hyperspectral workflows therefore offers practical benefits: enhanced feature identification, sharper boundary delineation, and im-

proved classification accuracy[32], [33] across applications ranging from agriculture[34] to environmental monitoring[21]. These benefits rely on achieving a balance between spatial enhancement and spectral preservation, which is assessed using quantitative metrics and will be examined in detail in Chapter 6.

1.3 Thesis Contributions and Structure

This thesis advances hyperspectral imaging through two complementary contributions. The first is a theoretical Zemax-based optical design using customised lenses to explore performance limits in spectral accuracy and throughput. The second, and primary, contribution is a dual-modality hyperspectral-panchromatic device built from COTS components. This system integrates pansharpening directly into acquisition, enabling real-time panchromatic targeting as well as high spatial resolution images easily coregistered with datacubes.

The custom optical model, designed in Zemax, prioritises throughput and spectral reliability. In this context, reliability refers to the maintenance of spectral uniformity across the spatial dimension, ensuring that wavelength accuracy is preserved from the centre of the slit to the edges. By refining lens geometry and the slit-to-detector optical path, the design achieves improved light collection and reduced spectral distortion, providing a reference for uniform spectral resolution across the field.

The COTS hybrid device forms the core outcome of this work. Incoming light is divided between a high-resolution detector and the spectrograph, enabling simultaneous hyperspectral and panchromatic capture. This dual-detector setup allows pansharpening to be applied between datasets produced by a single instrument rather than relying on external imagery. The device is supported downstream by a dedicated processing framework, where a modified Gram-Schmidt Adaptive (GSA) algorithm is evaluated using spatial modulation transfer function (MTF) metrics and spectral consistency measures. The final chapter of this thesis focuses on the evaluation of sharpened datacubes from a spatial/spectral viewpoint as well as application-based metrics.

The thesis is organised as follows:

Chapter 2 reviews the foundations, applications, and limitations of hyperspectral imaging, with emphasis on spatial anisotropy in pushbroom systems and pansharpening as a corrective strategy. The review establishes the need for compact solutions that balance manufacturability with quantitative fidelity.

Chapter 4 presents the optical design work. A custom Zemax model is developed to investigate theoretical performance limits, with emphasis on throughput, spectral uniformity and spatial resolution. In parallel, the OpenHSI model is redesigned using COTS components, similarly targeting spectral accuracy across the slit/wavelength range, and forms the basis of the dual-modality system that follows.

Chapter 5 details the COTS dual-modality device, describing its opto-mechanical design, calibration methods, and field deployment. Key contributions include a compact housing assembly that enables simultaneous hyperspectral

and panchromatic capture, and raw datacube capture using two models from different stages of development.

Chapter 6 examines the integration of pansharpening into hyperspectral data processing. A virtual-camera interface is presented for datacube compilation and adds to the data preparation stage alongside feature matching image coregistration and calibration corrections. The modified Gram-Schmidt Adaptive (GSA) algorithm is then implemented and performance is quantified using spatial MTF analysis together with spectral and application-level metrics including SAM, ERGAS, and NDVI consistency. Results demonstrate measurable improvements in spatial fidelity while maintaining acceptable spectral deviation, validating intra-device pansharpening as a practical strategy for compact imagers.

Chapter 2

Literature Review

The establishment of hyperspectral imaging (HSI) as a distinct discipline within remote sensing set the stage for the development of diverse instrument architectures. These various device designs correspond to different modes of capture, the strengths and applications of which will be explored below.

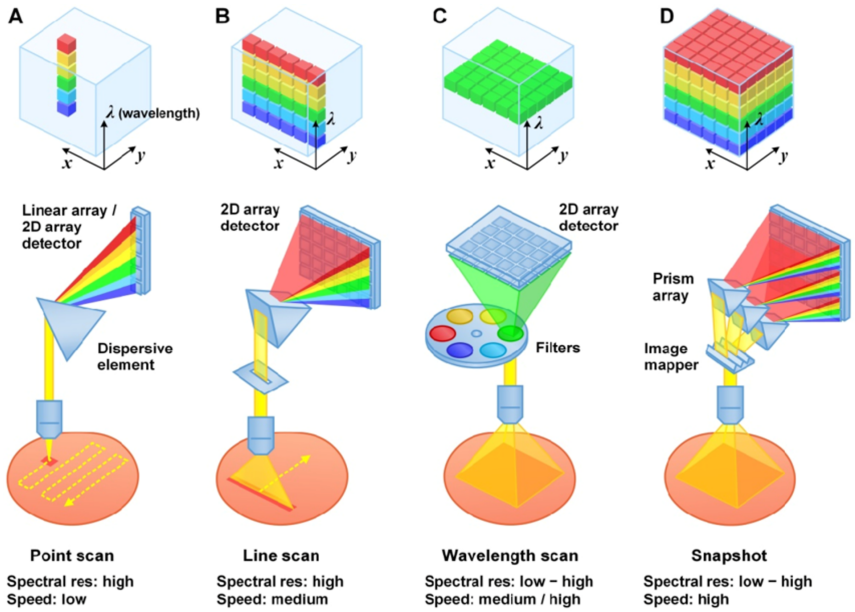

Figure 2.1: Various image modes of capture across hyperspectral imaging. Figure adapted from Wang et al. 2017[35].

2.1 Architectures of Hyperspectral Imagers

HSI architectures are generally categorised as pushbroom, whiskbroom, snapshot, or spatiospectral (tunable-filter) systems, each defined by how they sample spatial and spectral dimensions[36], [37].

Pushbroom imagers capture spectral profiles along a single spatial line of the scene in each exposure. Unlike snapshot cameras, which acquire full two-dimensional images per frame, pushbroom systems use a two-dimensional detector where one

axis corresponds to across-track spatial pixels and the other to dispersed wavelength channels[7]. The second spatial axis is reconstructed through platform motion (e.g., UAV, aircraft, satellite), line by line, to form the datacube. This capture method leads to higher SNR than other techniques, as the full detector space can be used for single slices of the final datacube. AVIRIS exemplifies the pushbroom sensor, achieving signal-to-noise ratios exceeding 1000:1 while maintaining broad spectral coverage from 400–2500 nm for mineral mapping and vegetation studies[3].

Whiskbroom systems employ a scanning mirror to sequentially direct light from the ground scene to a single detector or small array, building images pixel by pixel. While this yields uniform spatial resolution, it introduces mechanical complexity and slower acquisition speeds, making them less suitable for dynamic platforms[4]. Early Landsat missions with MSS and TM sensors are representative examples[1].

Snapshot systems capture entire datacubes in a single exposure using integral field units, interferometers, or filter mosaics integrated onto detectors. They provide excellent temporal resolution, critical for monitoring dynamic processes such as physiological changes in plants or transient atmospheric events. In addition, calibration pipelines are more complex, and light throughput is reduced compared to scanning systems[36], [38]. Despite these trade-offs, snapshot systems are increasingly used in biomedical imaging and precision agriculture where temporal synchrony outweighs spectral detail.

Spatiospectral imagers rely on tunable filters, such as acousto-optic tunable filters (AOTFs) or liquid-crystal tunable filters (LCTFs), to sequentially isolate narrow wavelength bands across the scene. This design provides programmable spectral selection, with tunable step sizes as fine as 1–5 nm, but overall throughput is reduced due to multiple sequential exposures. Acquisition speed is slower than pushbroom or snapshot instruments, restricting their utility in dynamic settings[39]. They are, however, well suited to laboratory and biomedical contexts where spectral flexibility and controlled conditions are prioritised[40].

Different architectures reflect different application specialisations. Pushbroom systems such as AVIRIS and Hyperion emphasise photon throughput and wide spectral coverage/fidelity, making them effective for detailed scientific analysis but less suited for rapid or high-resolution spatial mapping[41]. This mode of capture is also well suited to moving-platform captures such as UAVs, satellites and planes due to the procedural datacube capture. Snapshot and spatiospectral scanners capture data rapidly with good spatial detail, although typically with fewer or broader bands [31]. Whiskbroom instruments maintain consistent spatial sampling and robust spectra but are limited by mechanical scanning. Compact and low-cost designs using commercial components extend accessibility, but usually at the expense of either spectral resolution, spatial resolution, or both. Within each of these modalities is an inherent balance between spectral and spatial information on the detector plane, with some using time-modulation to increase the total information captured.

2.2 Performance Trade-offs in Hyperspectral Imager Design

Beyond the choice of imaging architecture, hyperspectral imager performance is constrained by optical design, detector technology, and system-level factors. These constraints manifest as trade-offs not only between spectral resolution, spatial sampling, and photon throughput, but also temporal resolution, cost, and size-weight-power requirements. No system can optimise all parameters simultaneously, and instrument design reflects the balance demanded by specific applications.

2.2.1 Slit and Detector Constraints

The entrance slit of a pushbroom spectrometer defines the along-track sampling at the object plane (by its width) and sets spectral resolution together with dispersion and focal length. Narrower slits improve bandpass but cut photon throughput, lowering SNR unless compensated for with longer integrations or increased illumination. In practice, most pushbroom systems use slit widths between 10–80 µm, with the choice closely linked to detector pixel size for efficient sampling[42]. Instruments often select 25 µm to prioritise resolution over speed; for example, a pushbroom elemental-mapping setup reports a 25 µm slit with a 1024×1024 Intensified Charged Coupled Device (ICCD) and a $\sim$68.5 nm spectral window in a single setting[43]. When slit width dominates the system point-spread function, the spectral full width at half maximum (FWHM) scales linearly with the slit, so halving the slit width nearly halves the instrumental bandwidth $\Delta\lambda$. These dependencies show why UAV and field systems frequently relax slit width (e.g., to $\sim$50–80 µm) to maintain flux at short integration times, whereas airborne research instruments pair narrower slits with larger apertures and longer dwell times to support finer spectral sampling[44].

2.2.2 Dispersive Elements

The dispersive element spreads the collimated slit image across the detector in the spectral dimension, and thus controls both spectral resolution and throughput. Transmission gratings are compact and inexpensive, and can achieve high diffraction efficiency in the visible and near-infrared[45]. Gratings fabricated from fused silica with anti-reflection coatings often outperform reflective gratings by reducing integration times and illumination requirements, a significant advantage for portable or battery-powered instruments[16]. This advantage, however, is not universal and efficiency depends on blaze angle, polarisation, and wavelength range. Typical values for efficiency can lie between 70–90% under ideal conditions at the "blaze wavelength" and falls away either side for both grating types[46], [47]. Reflective gratings retain higher performance in the ultraviolet and shortwave infrared, where transmission substrates absorb strongly. They also fold the optical path and support concentric geometries such as Offner relays, which are effective at suppressing aberrations. Reflective gratings have been extensively adopted in hyperspectral spectrometer design, with Mouroulis and Green providing a cornerstone analysis of their aberration control and broad spectral performance[16]. Open-source and low-cost instruments, including OpenHSI, often adopt transmission gratings to minimise size and complex-

ity[25]. The choice of dispersive element is therefore a balance between efficiency, spectral coverage, and packaging constraints. Prism-based dispersion remains useful in short-path laboratory instruments but is generally limited by chromatic aberration. Prisms also exhibit nonlinear dispersion, spreading shorter wavelengths more strongly than longer ones, which can lead to non-uniform spectral sampling unless corrective optics or resampling are applied. Gratings are more nearly linear, but blaze- and angle-dependent effects still cause wavelength-dependent resolution[48].

2.2.3 Aberrations and Optical Fidelity

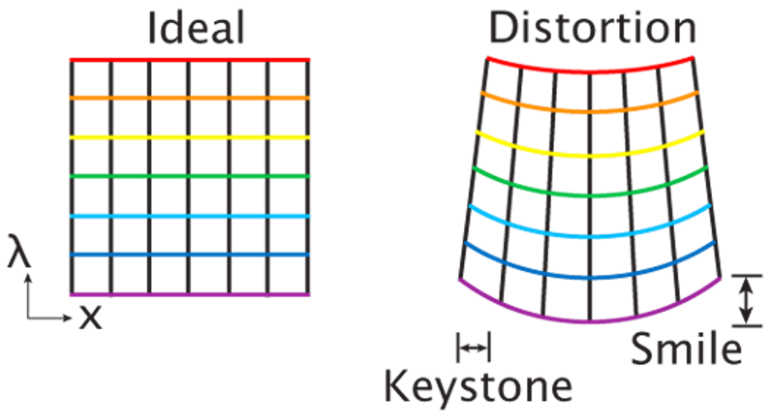

Figure 2.2: Diagram showing how the detector image can be altered by smile and keystone distortions. Here the spectral dimension is vertical (y), and the across-track spatial dimension is horizontal (x). Figure adapted from Ref. [49].

Aberration control is critical for quantitative analysis. Smile distortion, the curvature of spectral lines across the slit, arises because rays from different field angles strike the grating at different incidence angles, producing slightly different dispersion outcomes across the detector. This effect can also be exacerbated by misalignments in device assembly. Keystone, the geometric distortion of spatial information, occurs when imaging geometry is imperfect and causes straight features in the scene to appear tilted or bowed. Both effects complicate wavelength calibration and reduce the reliability of reflectance retrievals. Offner relays suppress these aberrations through concentric reflective surfaces, while transmission-grating layouts are more prone to distortion at field edges. Lower F ratios (focal length divided by aperture) improve photon throughput but enlarge the optical package, adding mass and power demand. High-performance airborne and spaceborne instruments typically prioritise resolution and throughput, while UAV and handheld systems may accept lower performance in favour of compactness and manufacturability[50].

2.2.4 Spectral Resolution versus Throughput

The balance between spectral resolution and throughput is one of the defining challenges of HSI. Achieving narrow spectral bands requires strong dispersion and a narrow slit, which reduces the number of photons reaching the detector. The slit then is the limiter for both resolution types, as maximising spectral resolution by increasing pixel density at the detector also spreads the input light thinner, resulting in decreased SNR. This loss of SNR is especially detrimental in low-light environments

or high-speed capture platforms. Airborne systems such as AVIRIS-NG achieve high spectral fidelity with 5 nm bands and long integration times, but this requires low F ratios, high optical quality, and stable platforms to avoid motion blur[3], [51]. Field-deployable or UAV-mounted instruments often accept band widths of 10–15 nm to maintain throughput, a compromise that constrains applications requiring subtle spectral discrimination, such as overlapping mineral features in Short Wave Infra-Red (SWIR) regions or water quality retrieval in aquatic environments[52]. The need to balance resolution and throughput drives many design decisions in compact imagers and motivates the use of fusion-based strategies to recover spatial or spectral detail.

2.2.5 Detector Technologies and Noise Sources

Detector technology defines the accessible spectral range of hyperspectral imagers. Silicon CCD and CMOS arrays dominate the visible to near-infrared (400–900 nm). They are inexpensive, offer high pixel counts, and benefit from mature readout electronics, but suffer from rising dark current and declining quantum efficiency beyond this range. SWIR imaging relies on indium gallium arsenide (InGaAs) detector arrays, which extend sensitivity to about 2500 nm but at much higher cost and with smaller array sizes. Mid- and long-wave infrared instruments use mercury cadmium telluride (HgCdTe, or MCT) detectors, which are generally restricted to defence or specialised research due to cost, complexity, and export control regulations on infrared sensor technology[23]. Alternative technologies such as type-II superlattices (T2SLs) show promise for rivaling HgCdTe performance with improved uniformity, but remain costly and immature for mainstream hyperspectral applications[53].

Noise sources further constrain detector performance. Shot noise, read noise, and thermal noise all reduce signal-to-noise ratio, with thermal dark current becoming dominant in the SWIR if cooling is not employed. In portable systems without cooling, this can overwhelm weak reflectance signals and degrade retrieval accuracy. Cooling suppresses and stabilises dark current but adds size, weight, and power consumption, limiting applicability on UAV platforms. Changes in the dark current signal are challenging to calibrate for in a system, and can introduce random variability to data outputs. Detector nonuniformity introduces pixel-to-pixel gain and offset variations, while optical distortions such as spectral smile and keystone alter the geometry of spectral and spatial mapping. These effects complicate wavelength and radiometric calibration, as corrections must account for both detector variability and optical distortion. The resulting pipelines add computational overhead and can reduce efficiency in field operations[54], [55].

2.2.6 Motion Artifacts, Anisotropy, and Calibration Drift

Pushbroom sensors acquire datacubes line by line and are therefore highly sensitive to motion. Variations in platform velocity or pointing angle lead to geometric distortions, while turbulence and vibration cause spatial jitter. Gimbal stabilisation and motion compensation can reduce these errors but add mass and processing requirements[51]. These inconsistencies can also be corrected in post-capture data processing by georectification which aligns each scanline of the hyperspectral cube to geographic coordinates using sensor position, orientation, and terrain models[56].

Along-track resolution is also limited by slit width and integration time, since longer exposures or higher platform velocities lead to motion blur and increased spacing between successive lines. This produces anisotropy relative to the across-track dimension. The subsequent imbalance in spatial fidelity is a critical drawback of the architecture and central to the motivation for this thesis. Calibration stability adds further constraints, as spectral registration can drift with temperature, mechanical stress, or long-term misalignment of dispersive elements, reducing the accuracy of radiance/reflectance retrievals in field conditions. Laboratory-grade instruments incorporate gas-cell or lamp references to maintain accuracy, but these increase system complexity. Portable systems often rely on less rigorous methods, which reduce spectral fidelity in the field[25].

2.2.7 Cost, Size, and Accessibility

Cost and accessibility remain major barriers. Commercial airborne sensors such as Specim FENIX or Headwall Nano-Hyperspec exceed $100,000 and require specialised mounting and calibration infrastructure. These instruments deliver excellent spectral fidelity and calibration robustness but are beyond the reach of many research groups. As a result it is common for companies to offer the use of these high-end devices as a service. COTS-based and DIY systems can reduce costs by multiple orders of magnitude[12], but at the expense of spectral resolution, calibration stability, and spatial isotropy. Expensive commercial devices often come with bespoke software, which represented a significant obstacle in using open-source devices, one that was targeted by the OpenHSI calibration, capture and processing library[25]. Low-cost instruments are often restricted to academic or experimental contexts rather than operational deployment. High component costs, particularly for SWIR detectors and precision gratings, together with processing demands and calibration requirements, keep HSI less accessible than multispectral approaches. This motivates the need for advanced development of low-cost imaging technology to bridge this performance gap.

2.3 Comparative Analysis of Hyperspectral Imagers

The hyperspectral imaging market has diversified significantly, encompassing high-performance commercial instruments, low-cost systems built from commercial off-the-shelf (COTS) components, and bespoke instruments tailored to niche applications. This section reviews representative devices across these categories and evaluates their unique characteristics.

2.3.1 Commercial High-Performance Imagers

Established vendors such as Specim, Headwall Photonics, and BaySpec dominate the high-performance end of the hyperspectral market. These instruments are designed for airborne campaigns, laboratory spectroscopy, and industrial inspection where stability, spectral fidelity, and throughput are paramount.

The Specim AisaFENIX is a benchmark airborne sensor offering full-range coverage

from 380–2500 nm through multiple dispersive channels. It delivers spectral resolutions of 3–10 nm depending on region, with high SNR enabled by cooled detectors and precision fore-optics and an F-number of 2.4[57]. This specialised performance also comes at the cost of portability as the unit is 15–23kg depending on model, and roughly 50x50x20cm. Another of Specim's core product line is the FX10, a widely deployed unit in industrial settings, covering the visible-NIR range (400–1000 nm) with 5.5nm spectral resolution and up to 327 fps capture rate. The FX10 also captures at a notably fast F-number of 1.7. These instruments feature pushbroom operation, integrated calibration units, and proprietary software pipelines for real-time spectral classification[58].

Headwall Photonics offers a comparable portfolio, including the Nano-Hyperspec for UAV integration and the Micro-Hyperspec for laboratory and field applications. These sensors employ aberration-corrected reflective gratings to achieve low smile and keystone distortions, ensuring robust calibration over extended deployments [24]. Their systems emphasise compactness and robustness while maintaining spectral resolutions of 5–6 nm at a 400–1000nm wavelength range. The Micro-Hyperspec series extends to instruments configured for the SWIR region (900–2500nm) with spectral resolution of 8–10nm[59]. All systems across these two lines operate at a 2.5 F-number.

BaySpec specialises in compact hyperspectral solutions, particularly in the SWIR and Raman domains. The OCI-1000 & 2000 series are designed for portable field use, balancing reduced spectral coverage (600–1000nm, 5nm spectral resolution, undisclosed F#) with affordability and ease of integration [60]. BaySpec's innovations in volume-phase holographic gratings have yielded systems with high diffraction efficiency across broad bands.

The cost of these commercial instruments typically exceeds $50,000-$100,000, reflecting precision optics, cooled detector arrays, and integrated calibration mechanisms. Their reliability and vendor support make them attractive for government agencies, well-funded laboratories, and industrial users, but the price and proprietary architectures limit accessibility for small research groups and businesses.

2.3.2 COTS and DIY Devices

The past decade has seen the emergence of low-cost hyperspectral imagers built from COTS optics and consumer-grade detectors. These designs typically trade spectral fidelity, calibration stability, and robustness for accessibility, replicability, and reduced cost, but they collectively demonstrate that functional HSI can be achieved at a fraction of the cost of commercial systems.

The V6 system of Henriksen et al.[61] builds on an earlier prototype developed by Sigernes et al.[12]. The V4 model demonstrated that a functioning pushbroom spectrometer could be built with low-cost optics and 3D-printed mounts, but suffered from low throughput and residual aberrations. The V6 addressed these constraints by adopting faster C-mount optics (f/2.8), a wider 50 µm slit, and a lower groove density grating. These changes reduced spectral resolution from 1.4 to 3.5 nm but increased light collection efficiency by nearly an order of magnitude, enabling stable operation under natural illumination. Long-term calibration tests showed

reflectance stability within ±5 %, and field deployments demonstrated utility for mapping vegetation and water targets. The design illustrates a deliberate trade-off: sacrificing ultimate spectral fidelity in favour of improved SNR, and maintained portability.

Figure 2.3: Exploded view of the Henriksen et al. V6 DIY spectrometer. Figure adapted from Ref. [61]

OpenHSI by Mao et al.[25], represents one of the most fully developed open-source imagers, and was inspired by the devices introduced by Signernes et al. The design combines off-the-shelf lenses and transmission gratings with 3D-printed components and a transparent calibration pipeline. It spans roughly 400–830 nm with effective resolution of about 4 nm after binning using a 25μm slit. A key novelty is the open-source framework: full parts list, capture and calibration scripts, and example datasets are available, enabling replication by small research teams. While limited in throughput compared with professional-grade instruments, OpenHSI has been validated on ecological targets such as vegetation and minerals, and has catalysed a community of derivative DIY designs.

Chang et al.[62] presented the Hyper Spectral Camera Analyzer (HyperSCAN), a modular COTS-based design that covers both VNIR and SWIR regions through interchangeable modules. HyperSCAN prioritises broad adoption by combining modest resolution with flexible spectral coverage and stable SNR. The work also links hyperspectral capture with pansharpening workflows, drawing directly from Landsat datasets and reinforcing the role of fusion techniques in enhancing spatial resolution.

Salesin et al.[63] demonstrated a polarisation-filter based alternative that replaces dispersive optics with rotatable filter assemblies. This design is mechanically simple and provides tunable bands in the VNIR. While slower due to sequential acquisition, classification accuracies for vegetation and soils were reported within 5 % of pushbroom benchmarks. Such systems are well suited to education and proof-of-concept deployments where affordability outweighs performance.

Pechlivani et al. [64] described a Raspberry Pi-based imager with a 3D-printed housing and compact optical train. The system spans 379–937 nm with sampling of 1.9 nm, delivering nearly 300 bands at low cost. Despite modest spatial resolution (127 × 125 pixels), the instrument integrates automated acquisition software and calibration routines, making it attractive for student projects and laboratory demonstrations. This design exemplifies the accessibility gains enabled by consumer electronics, while highlighting ongoing trade-offs in spatial coverage, calibration stability, and SNR compared with established airborne systems.

System	Spectral Range (nm)	Spectral Resolution /Sampling (nm)	Bands /Format	Detector Pixels	Mass /Power	Cost
Sigernes (2018) DIY [12]	400–800	Not explicitly specified	Pushbroom, visible range	1900 × 1200 px	∼200 g, portable	∼€700
Sigernes V6 (2022) [61]	400–800 (usable), full detector 300–900	3.3 nm (theoretical), 3.7 nm (measured at 546 nm)	Pushbroom, 50 μm slit, 300 g/mm grating	1900 × 1200 px	∼350 g	€2600
Mao (2022) OpenHSI [25]	400–830	∼4 nm (binned)	Pushbroom, 100+ bands after binning	2048 × 1536 px	119 g	∼$2000
Pechlivani (2023) DIY Pi [64]	379–937	1.9 nm sampling interval	Pushbroom, 290 bands	3280 × 2464 px	∼2kg, ∼10 W	€195
Chang (2025) HyperSCAN [62]	450–850	∼10 nm FWHM	Pushbroom, 162 bands	2492 × 2048 px	1.4 kg, <5 W	CubeSat-class (prototype)
Salesin (2022) DIY Prototype [63]	∼400–700	Not fixed; reconstructed from filters	Filter-based, tunable bands	Consumer camera pixels	DSLR-camera function	Low-cost consumer components
Commercial Systems [24], [58], [60]	380–2500 (VNIR+SWIR)	∼2–12 nm depending on band	Pushbroom, hundreds of contiguous bands	UAV: submeter GSD; Airborne: broad coverage	0.5–20+ kg, tens of W	>50k

Table 2.1: Specifications of representative DIY/COTS hyperspectral imagers compared with commercial high-performance systems.

Taken together, these DIY and COTS instruments highlight the growing accessibility of HSI outside traditional aerospace and defence domains. They demonstrate that functional systems can be built with budgets under $5000, leveraging consumer detectors, 3D-printed mechanics, and open-source software. Rather than competing directly with professional systems, these designs provide research platforms that broaden participation, and allow modification for varous use-cases. The specification of these devices are benchmarked against commercial imagers of similar wavelength range in Table 2.1.

2.4 Applications of Hyperspectral Imaging

The versatility of HSI stems from its ability to resolve detailed spectral signatures that correspond to material properties, chemical composition, and physiological states. This section reviews the major domains where HSI has demonstrated impact, including agriculture, ecology, geology, industrial studies, medicine, food safety, and space-based applications.

2.4.1 Agriculture and Vegetation Monitoring

Precision agriculture has been one of the most prominent fields for HSI. Studies have used imagers to detect subtle variations in chlorophyll, water content, nutrient status, canopy temperature, and pigment composition, providing early indicators of crop stress at accuracies above 80%[13]. Beyond stress detection, these measurements enable yield prediction, optimisation of fertiliser and irrigation strategies, and monitoring of disease onset before visual symptoms appear[65], [66]. More recent portable snapshot HSI systems for handheld and tripod use have extended these capabilities to field-level monitoring, enabling real-time diagnosis of crop health. Their performance is closely tied to spectral sampling: finer sampling (on the order of 5 nm or below) resolves narrow chlorophyll and red-edge features, improving sensitivity to subtle physiological changes and maintaining classification accuracies comparable to airborne systems [67].

Forestry and ecological studies similarly benefit from the ability to differentiate species and quantify canopy properties. Hyperspectral sensors such as (manned-aircraft) and Hyperion (satellite-mounted) have been employed to classify tree species in mixed forests with accuracies of 70-95% across various studies, to estimate biomass, and to monitor pest damage with improved sensitivity over multispectral approaches[68], [69]. UAV-mounted imagers have further expanded ecological monitoring, resolving invasive species distributions at plot scales with ground sampling distances under 20 cm, providing insights into biodiversity dynamics at fine spatial scales[70].

2.4.2 Aquatic and Coastal Applications

Hyperspectral sensors are uniquely sensitive to absorption features of chlorophyll-a (near 675 nm), suspended sediments, and colored dissolved organic matter (CDOM) in the visible to near-infrared range. Studies using AVIRIS and HyMap have successfully quantified algal blooms with detection thresholds as low as 1–2 μg/L chlorophyll-a, mapped seagrass beds with overall classification accuracies above 80%

based on field-validated confusion matrices distinguishing seagrass, macroalgae, bare substrate, and water classes, and monitored sediment plumes in estuaries[71]. Hyperspectral data have also been applied to coral reef health monitoring, distinguishing bleaching stages through shifts in pigment absorption bands[72]. These capabilities are increasingly being extended to UAV-based sensors, enabling metre-scale mapping for coastal conservation and management.

2.4.3 Geology and Mineral Exploration

Geological applications of HSI are particularly significant in the short-wave infrared (SWIR) domain, where minerals exhibit distinct absorption features. Imaging spectrometers have been widely used for mineral exploration, enabling mapping of alteration zones and ore deposits with accuracies exceeding 85% when distinguishing clay, mica, and carbonate minerals[10], [73]. Reflectance features such as the Al-OH absorption near 2200 nm or the CO_3 overtone near 2340 nm can be resolved at spectral resolutions on the order of 10–20 nm[74]. Bedini (2009; [74]) demonstrated that HyMap's 13–20 nm bands were capable of mapping carbonatite and alteration zones with overall accuracies above 85%, indicating that this resolution represents a practical threshold for geological applications.

Figure 2.4: The HyMap device developed by HyVista Corporation has been employed by many Earth-observation studies[75].

2.4.4 Industrial and Cultural Studies

In mining, hyperspectral systems have been used for rapid classification of ore bodies and for monitoring acid mine drainage through detection of iron oxides and sulfate minerals, achieving >80% accuracy relative to geochemical assays[76]. Also in construction imagers have been used to monitor concrete curing and detect subsurface moisture variation at depths of several centimetres[77]. Cultural heritage applications have also been established where HSI devices have mapped pigment composition in paintings, identified restoration layers, and detected degradation

phenomena such as salt efflorescence or surface weathering on stone monuments with sub-millimetre resolution[78], [79]. The narrow spectral resolution of HSI (typically 2–5 nm in VNIR cultural heritage studies) provides information not available to conventional imaging, supporting the preservation of historical assets.

2.4.5 Medical Applications

HSI has emerged as a diagnostic and intraoperative imaging tool due to its sensitivity to biochemical and physiological variations. Applications range from dermatology, where it has diagnosed melanoma at sensitivities above 90%[80], to endoscopy, where spectral differences in hemoglobin absorption support identification of malignant tissue[15]. More recently, HSI has been trialled intraoperatively to monitor tissue perfusion in reconstructive and gastrointestinal surgery, providing quantitative oxygenation maps with errors under 5% relative to reference probes[81]. These developments highlight how compact sensors and computational pipelines are enabling the transition of HSI from remote sensing into the clinical domain.

2.4.6 Food Quality and Safety

The food industry has adopted HSI as a rapid, non-destructive quality control method. Hyperspectral analysis can detect bruising in fruit up to three days before visible symptoms appear, with classification accuracies over 90% in apples[82], and contamination on meat surfaces with over 85% accuracy in real-time conveyor belt settings[83]. Unlike traditional inspection methods, which rely on manual sampling, HSI provides spatially comprehensive data that improves efficiency and reduces waste. Portable and conveyor belt mounted HSI systems are increasingly being deployed in industrial contexts.

2.4.7 Space Exploration

Spectrographs such as the Multi-Unit Spectroscopic Explorer (MUSE) integral field spectrometer, installed at the Very Large Telescope (VLT) use hyperspectral imaging to investigate astronomical phenomena. They achieve exceptional spectral fidelity by employing large-format optics, cryogenically cooled CCDs, and adaptive optics correction, but their size and cost place them outside terrestrial remote sensing[84]. At these ranges, throughput and resolution trade-offs become paramount where detectable signals can be weak and difficult to locate. In line with Earth-based geological studies, a bespoke hyperspectral device is also integrated into the Mars Reconnaissance Orbiter. The CRISM spectrometer covers 370–3920 nm, enabling mineralogical mapping of Mars with high spectral precision[85]. Planetary imagers are engineered for extreme environments, requiring radiation-hard detectors and robust calibration systems.

2.5 Pansharpening

Pansharpening fuses a high-spatial-resolution panchromatic image with a lower-spatial but spectrally rich image to produce data that are simultaneously sharp and spectrally faithful. The technique originated in satellite remote sensing, where

multispectral sensors provided pixels with 10–30 m spatial resolution while companion panchromatic channels offered 1–5 m resolution. By fusing the two, analysts achieved both spectral discrimination and fine spatial mapping[86]. The same logic is now applied to hyperspectral imagery at airborne and UAV scales, although the much higher band count and tighter tolerances on spectral preservation make the problem more challenging. Acceptable distortions in multispectral fusion (e.g., a few percent RMSE or 3–5° SAM[a]) are not tolerable in hyperspectral data, where narrow-band signatures are more sensitive and these kinds of deviations can render data unusable.

2.5.1 Historical context and early methods

The earliest families of data fusion methods were based on component substitution. Intensity-Hue-Saturation (IHS) transforms inject the panchromatic image into the intensity channel of an RGB or multispectral stack and invert the transform[26]. Principal Component Analysis (PCA) substitutes the first component with the panchromatic image[27]. Gram-Schmidt (GS) introduced an orthogonalisation framework in which a synthetic intensity, derived from the low-resolution bands, is replaced by the panchromatic image before inversion[28]. These approaches are attractive for their speed, low computational cost, and spectral consistency but differences between the panchromatic sensor's spectral response and the narrower HS bands can produce hue shifts and spectral biases of 5–10% in reflectance.

2.5.2 Multiresolution Analysis

Another major family of pansharpening methods is based on multiresolution analysis (MRA). MRA methods inject only high-frequency spatial information, reducing spectral bias. Wavelet and Laplacian-pyramid schemes decompose both the panchromatic and multispectral images into scale spaces, align the high-frequency components, and reconstruct the sharpened bands[30], [87]. Because only detail is transferred, the low-frequency radiometry of the hyperspectral data is preserved. Performance depends critically on how well the low-pass filters approximate the point spread functions of the sensors. In benchmark studies on IKONOS[88] and QuickBird[89] imagery, wavelet-based MRA achieved ERGAS (Erreur Relative Globale Adimensionnelle de Synthèse) scores under 3 and Spectral Angle Mapper (SAM) (See Chapter 3) below 3°, improving significantly over PCA and IHS[30]. For hyperspectral data, higher band count demands careful MTF-matched filtering to prevent distortions accumulating across hundreds of bands. Despite this added complexity, MRA remains more efficient than variational or learning-based methods and can be applied to full hyperspectral cubes without prohibitive runtimes.

2.5.3 Variational and Bayesian Formulations

Variational methods pose pansharpening as an optimisation problem. The fused image is constrained to match the observed low-resolution spectrum after blur and downsampling, while being consistent with the gradients of the panchromatic image[90]. Variational methods add penalty terms that favour properties such as

[a]Spectral Angle Mapper (SAM) is a spectral distortion metric, detailed in Chapter3

smoothness in space or correlation between bands. Bayesian approaches extend this by estimating full probability distributions, explicitly modelling factors like spectral smoothness, sparsity, or noise [31], [91]. These approaches deliver state-of-the-art spectral preservation, with 30–40% lower SAM and RMSE than component substitution in comparative studies[30]. Their drawback is computational burden: solving high-dimensional optimisation problems or sampling Bayesian posteriors is orders of magnitude slower than GS or MRA, often requiring minutes per image. This restricts their use to offline analysis rather than real-time or embedded applications.

2.5.4 Machine Learning Methods

Learning-based methods train models to approximate the nonlinear mapping from low-resolution bands and a panchromatic image to a fused output. Convolutional neural networks (CNNs) introduced a step change, outperforming GS and MRA with ERGAS (See Chapter 3) reductions of 15–20% and SAM improvements of 1–2° in WorldView-2 and QuickBird benchmarks[32]. Domain-trained and fine-tuned CNNs further reduced spectral bias when training and test sensors differed [92], [93]. More recent spectrally-predictive frameworks expand on this area with field-leading spectral preservation and ERGAS scores of 1.747[94]. For hyperspectral fusion, however, the lack of representative training data is a major limitation, and models risk overfitting to specific sensors. Computational cost is another barrier: training requires large datasets and GPUs, and inference, while faster than training, remains significantly more computationally intensive than methods like GS or MRA. Self-supervised strategies have abandoned the need for model training, instead using coefficient weighting and band-by-band progressive training across the datacube[95]. This method sacrifices some qualitative spatial resolution in favour of quick processing times low SAM and ERGAS scores (3–4 for both).

2.5.5 Gram-Schmidt Adaptive: formulation and practical use

The classical GS method constructs a synthetic intensity from the low-resolution bands, orthogonalises the panchromatic image against it, and substitutes the true pan image before inversion[28]. The Gram-Schmidt Adaptive (GSA) algorithm improves this procedure by introducing per-band regression gains, allowing the spatial detail injected into each band to scale with its correlation to the high-resolution image[87], [96].

A synthetic intensity is formed as a weighted sum of the bands, with weights w_i approximating the pan spectral response:

$$I = \sum_{i=1}^{B} w_i H_i. \tag{2.1}$$

High-frequency detail from the pan, D, is then injected into each band with an adaptive gain:

$$H_i^{\text{fus}} = H_i + g_i D, \tag{2.2}$$

where g_i is estimated by regression between band residuals and D. Gains may be computed globally or locally and are typically regularised to avoid over-injection in noisy bands.

With MTF-matched filtering, GSA achieves strong spatial enhancement while preserving spectra to within 1–2% reflectance RMSE in airborne and simulated hyperspectral datasets[97]. Its efficiency is another advantage: runtime scales linearly with pixel and band count, making the method suitable for near-real-time or onboard processing. For low-SNR bands, grouping wavelengths and interpolating g_i across them stabilises the regression without degrading fidelity. These properties have established GSA as a reference method for both multispectral and hyperspectral pansharpening, and it serves as the baseline for the work in this thesis.

Figure 2.5: Schematic showing the increased ground sampling afforded by various pansharpening techniques[98].

2.5.6 Applications of Pansharpening

Pansharpening has been widely applied in agriculture, where enhanced spatial fidelity improves the detection of crop stress, water availability, and nutrient deficiencies through sharpened NDVI and red-edge indices. Airborne and UAV studies have shown that pansharpened hyperspectral data can resolve patterns at the level of individual plants, supporting more precise interventions in precision farming[99] A recent study fused PRISMA hyperspectral data (30 m native) with its panchromatic band (5 m) and used pansharpened imagery to classify urban tree species. All species classes saw F1 (an accuracy-based metric for identification) score improvements of 10–20 % post-fusion [100].

In the geological domain, pansharpened hyperspectral images also from the PRSIMA imager have been shown to support archaeological and lithological mapping by enhancing the spatial resolution of absorption feature delineation. This has enabled the detection of small-scale features that would otherwise be spatially blurred in native resolution HSI [98].

Urban and built-environment studies have leveraged pansharpening for detailed classification of roofing and construction materials, monitoring of infrastructure, and cultural heritage preservation, where small-scale heterogeneity demands both high spectral and spatial accuracy. Pan-sharpened imagery has enabled roofing material classification (including hazardous materials such as asbestos, tiles, metal roofing) with $>$ 85% accuracy in WorldView-2 and WorldView-3 studies[101], [102].

2.5.7 Recent Advances in Pansharpening

Recent advances have focused on hybrid approaches and machine learning. Convolutional neural networks (CNNs) introduced significant gains by learning nonlinear mappings between low-resolution hyperspectral and high-resolution panchromatic inputs, improving ERGAS and SAM scores over classical methods[92]. Transformer-based architectures have further extended receptive fields and improved global consistency, reporting QNR (Quality without Reference) values above 0.95 on multispectral test sets[94].

Hybrid methods that combine classical frameworks with learned components, such as Gram-Schmidt detail injection constrained by CNN-based spectral correction, have demonstrated improved spectral preservation while maintaining computational efficiency[103].

Applied systems are beginning to incorporate these methods. HyperSCAN, a dual-module VNIR/SWIR imager, demonstrated the integration of CNN-based sharpening into its processing pipeline, highlighting the feasibility of embedding learning-based fusion in field-ready instruments[62]. Ref. [42] further advanced this direction with a pushbroom-specific enhancement strategy, showing that CNN-driven pansharpening can mitigate along-track anisotropy in microscopic HSI and deliver measurable gains in spatial resolution. Together these developments suggest a trajectory toward fusion methods that are both spectrally robust and accessible, bridging the gap between experimental algorithms and operational hyperspectral sensing.

2.6 Research Motivation

The literature reviewed above highlights both the transformative potential of HSI and the limitations that constrain its small-scale, deployable systems. Advances in spectrometer architectures, detector technologies, and data processing have steadily expanded the range of applications, from environmental monitoring to medical diagnostics. However, the goal of developing low-cost compact imagers suitable for UAV or field deployment remains elusive due to several unresolved technological gaps.

Foremost among these is the issue of spatial anisotropy in pushbroom sensors. Studies of open-source and COTS instruments such as OpenHSI and the V6 imager have shown aspect ratios as high as 10:1 between across-track and along-track sampling. This asymmetry restricts the utility of captured data for applications requiring isotropic spatial detail, such as fine-scale biodiversity assessment or urban mapping[104], [105]. Commercial systems from manufacturers such as Specim, Headwall, and BaySpec achieve high spectral and spatial performance, but their cost and integration requirements limit accessibility for small teams. Bridging this divide remains a popular theme in hyperspectral instrumentation.

The literature on pansharpening provides an opportunity to address these challenges from a different angle. Originally developed for satellite imagery, fusion of a high-resolution panchromatic image with lower-resolution spectral data has demonstrated consistent improvements in spatial clarity while maintaining acceptable spectral fidelity. While pansharpening methods are mature in the context of remote sensing, their application within a single compact device has been largely unexplored.

This thesis positions intra-device pansharpening as a practical strategy to mitigate the anisotropy inherent in accessible pushbroom imagers. By capturing panchromatic and hyperspectral data simultaneously within a shared optical housing, and by applying fusion methods adapted from the remote sensing literature, the system developed here looks to deliver datacubes with more isotropic spatial sampling than currently available. The approach draws on the open-source ethos of recent DIY hyperspectral projects, and introduces a new integration between hardware and processing.

Chapter 3

Evaluation Metrics

The assessment of hyperspectral pansharpening requires metrics that capture both the spatial enhancement of the sharpened image and the preservation of spectral information. Because no single index is sufficient, evaluations typically combine optical system metrics, full-reference fusion metrics, and task-specific indices, alongside qualitative examination of RGB-composite representations. The choice of metric also reflects the evaluation protocol: when ground-truth high-resolution data are available, full-reference comparisons are possible; otherwise, reduced-resolution or no-reference indices must be used [27], [30], [106].

Modulation Transfer Function (MTF)

The modulation transfer function (MTF) describes how an imaging system transfers contrast at different spatial frequencies. It is defined as the Fourier transform of the point spread function and is the standard measure of optical sharpness in protocols such as ISO 12233 [107]. MTF curves provide wavelength-dependent information: a higher MTF at a given frequency indicates stronger contrast retention. In hyperspectral imagers, the MTF is influenced by slit width, diffraction, optical aberrations, and detector sampling, and typically varies with wavelength. MTF-based metrics therefore provide a quantitative foundation for comparing intrinsic instrument sharpness and the impact of spatial enhancement techniques such as pansharpening. MTF is generally reported in line pairs (one dark and one bright bar) per millimetre at the detector, since this provides a system-level measure of contrast transfer relative to the sensor sampling limit, irrespective of object distance. This can be calculated by comparing line pairs in the raw captured datacube to known pixel-length of the detector. In anisotropic systems such as pushbroom imagers, representative line/mm measurements from the higher sampling dimension can be used as a reference point.

MTF at Nyquist or resolvable limit. For many hyperspectral and imaging spectrometer systems, performance is often benchmarked by the MTF at the detector's Nyquist frequency[108], [109]. The Nyquist frequency is exactly half the sampling rate of the detector. In an imaging sensor, this corresponds to one cycle (a dark–bright line pair) spanning two pixels. At frequencies higher than this, the sensor cannot represent the detail correctly and aliasing occurs. However, in com-

pact or laboratory-scale systems, contrast can collapse to 0 before that frequency. In these cases, contrast at the highest resolvable frequency can be reported, or contrast at a chosen benchmark line pairs/mm value[110].

Normalised AUC (Area Under MTF). A more holistic measure of contrast transfer is the area under the MTF curve (AUC), integrated over the measured frequency band:

$$\mathrm{AUC} = \int_{u_{\min}}^{u_{\max}} \mathrm{MTF}(u)\, du.$$

To make this comparable across systems and independent of the bandwidth of measurement, a normalised form can be adopted:

$$\mathrm{AUC}_{\mathrm{norm}} = \frac{1}{u_{\max} - u_{\min}} \int_{u_{\min}}^{u_{\max}} \mathrm{MTF}(u)\, du,$$

which yields a dimensionless value from 0 to 1. A value of 1 would correspond to an idealised brick-wall system that transmits all frequencies perfectly up to the cutoff, which is not physically realisable. Because hyperspectral MTF typically varies with wavelength (due to diffraction, spectrograph slit projection, and detector sampling), AUC are often computed (with their normalisations) as a band-averaged summary[111].

Full-reference fusion metrics

ERGAS. ERGAS (Erreur Relative Globale Adimensionnelle de Synthèse) or error-relative global dimensionless synthesis quantifies average radiometric distortion across bands under a reduced-resolution protocol [27]. With scale ratio h and per-band means μ_i, it is defined as

$$\mathrm{ERGAS} = 100\, \frac{1}{h} \sqrt{\frac{1}{B} \sum_{i=1}^{B} \left(\frac{\mathrm{RMSE}(i)}{\mu_i} \right)^2}. \tag{3.1}$$

Lower values indicate better spectral fidelity. High-performing methods on multispectral benchmarks typically report ERGAS between 2 and 4, while poor spectral preservation can push values beyond 10. For hyperspectral fusion, ERGAS tends to increase with band count, but careful MTF-matched injection (e.g., GSA) has been shown to maintain values in the 6–12 range [31], [97].

SAM. The Spectral Angle Mapper (SAM) looks at the similarity between two spectra by treating them as vectors in a n-dimensional space, where n is the number of bands. Each reflectance or radiance value is one component of the vector, so a spectrum is represented as $t = (t_1, t_2, \ldots, t_n)$. Two spectra t (test) and r (reference) can then be compared by computing the angle (a) between these vectors as per Figure 3.1:

$$a = \cos^{-1}\left(\frac{\sum_{i=1}^{n} t_i r_i}{\sqrt{\sum_{i=1}^{n} t_i^2}\, \sqrt{\sum_{i=1}^{n} r_i^2}} \right) \tag{3.2}$$

If the spectra are identical up to a scaling factor (e.g. one is brighter than the other but with the same shape), the vectors are collinear and the angle is zero.

Distortions in spectral shape, such as shifted or suppressed absorption features, cause the vectors to diverge, increasing the angle. SAM is therefore insensitive to overall gain differences but sensitive to changes in relative band structure. Conceptually, it measures whether two spectra ”point” in the same direction in spectral space.

On multispectral benchmarks, strong methods often achieve mean SAM values below 5°, while PCA or IHS substitutions can produce errors of 8–12°. For hyperspectral pansharpening, mean SAM below 5° is generally considered indicative of high spectral fidelity. This threshold is critical, as even small angular deviations in narrow-band data can result in incorrect material classification [112].

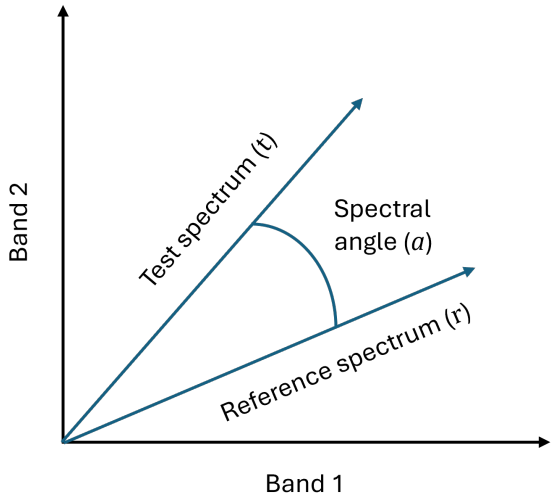

Figure 3.1: Diagram demonstrating the calculation of Spectral Angle Mapper values between a test and reference spectrum.

NDVI consistency (task-driven index). The Normalised Difference Vegetation Index (NDVI) is one of the most widely used spectral indices for vegetation monitoring, defined as

$$\mathrm{NDVI} = \frac{\rho_{\mathrm{NIR}} - \rho_{\mathrm{Red}}}{\rho_{\mathrm{NIR}} + \rho_{\mathrm{Red}}}, \tag{3.3}$$

where ρ_{NIR} is the surface reflectance in a near-infrared band (typically 750–900 nm) and ρ_{Red} is the reflectance in a red band (typically 630–690 nm). The index exploits the strong absorption of chlorophyll in the red region and high reflectance from leaf cellular structure in the NIR to provide a proxy for vegetation health and density.

Together, MTF-based measures, full-reference indices such as ERGAS and SAM, and task-driven checks like NDVI consistency provide a complementary framework for evaluation. MTF metrics probe the optical and system-level performance, ERGAS and SAM quantify the spectral fidelity of the fused data, and NDVI consistency tests whether sharpened imagery remains suitable for application-level analysis. These should all be coupled with visual evaluation of true ground-truth image sharpness improvement.

Chapter 4

Optical Design - Optimisation and Validation

4.1 Introduction

The early work of this thesis project focused on refining and enhancing the performance of the open-source spectrograph field, a domain that has gained prominence in recent years due to its ability to provide low-cost, modular solutions for hyperspectral imaging. This investigation was informed by a thorough review of existing devices and an evaluation of their performance within the confines of academic and research applications. Open-source spectrographs, such as the OpenHSI, have revolutionised accessibility in this field, enabling researchers to construct and use powerful imaging systems at a fraction of the cost of commercial devices. These devices can be more specialised than their commercial counterparts, and target specific characteristics or applications without fulfilling as wide a range of needs.

Within this project's parent research group, SAIL, hyperspectral imagers are used in UAV-based surveys of coastal and aquatic vegetation, underwater imaging of marine environments, and potential defence and security applications. Each of these applications demands a specific balance of performance criteria, including high throughput for low-light imaging, reliable spectral resolution for feature identification, and adequate spatial resolution/contrast for material and object detection. These requirements served as the guiding principles for this thesis, which began with an optics-based exploration of hyperspectral imager design and concluded with the development and production of the dual-imaging hybrid device.

To establish a starting point for this work, the original OpenHSI [25] was selected as a benchmark due to its alignment with open-source design principles. The OpenHSI is a compact, lightweight spectrograph intended for affordability, and demonstrates the potential for modular, do-it-yourself hyperspectral imaging. Operating across the visible spectrum (400–830 nm), it features a 3D-printed housing and uses accessible components from suppliers such as Edmund Optics and Thorlabs (a render is shown in Fig. Fig. 4.1). While well-suited for a wide range of research tasks, the system's spectral resolution, throughput, and spatial accuracy are limited relative to the requirements of high-performance applications. In particular, its pushbroom design introduces anisotropy in spatial resolution across scan and slit axes, which

Figure 4.1: A physical Openhsi model showing 3D-printed two-part housing and small field optics for portable applications.

can reduce the utility of the datacube in contexts requiring uniform spatial detail. These constraints reflect a necessary trade-off in favour of low-cost, open-access design. They also defined the focus of the optical work presented in this chapter, which explores two complementary design improvements: a custom optical system optimised for throughput and spatial resolution, and a COTS-based model developed to maintain accessibility while addressing specific limitations of the original OpenHSI.

4.2 Custom-lens model

An area of potential enhancement in the OpenHSI design is its limited optical throughput, a consequence of its F-number of 4. This restricts the amount of light collected, resulting in longer exposure times and reduced signal-to-noise ratio (SNR) under low-light conditions. These constraints reduce the system's suitability for light-limited scenarios such as UAV-based imaging, where shorter exposures and higher frame rates are necessary to avoid motion blur. A redesign of the device with higher throughput would resolve the existing issue in high-velocity scanning, and could also open up low-light underwater imaging opportunities.

In addition to throughput constraints, the OpenHSI system exhibits spectral inaccuracies, particularly off-axis and at shorter wavelengths. Chromatic aberrations at these positions introduce distortions that compromise spectral uniformity. Spatial resolution is also constrained; at the center of the field, MTF analysis at 670 nm shows usable contrast (contrast > 0.1) up to approximately 215 cycles/mm, but performance declines substantially off-axis. These results do not account for the field lens and may therefore underestimate final system performance, but they nonetheless indicate limitations in resolving fine detail. This limits the consistency of spatial detail across the slit, reducing the system's suitability for tasks requiring uniform resolution, such as long-range imaging or the analysis of intricate scene

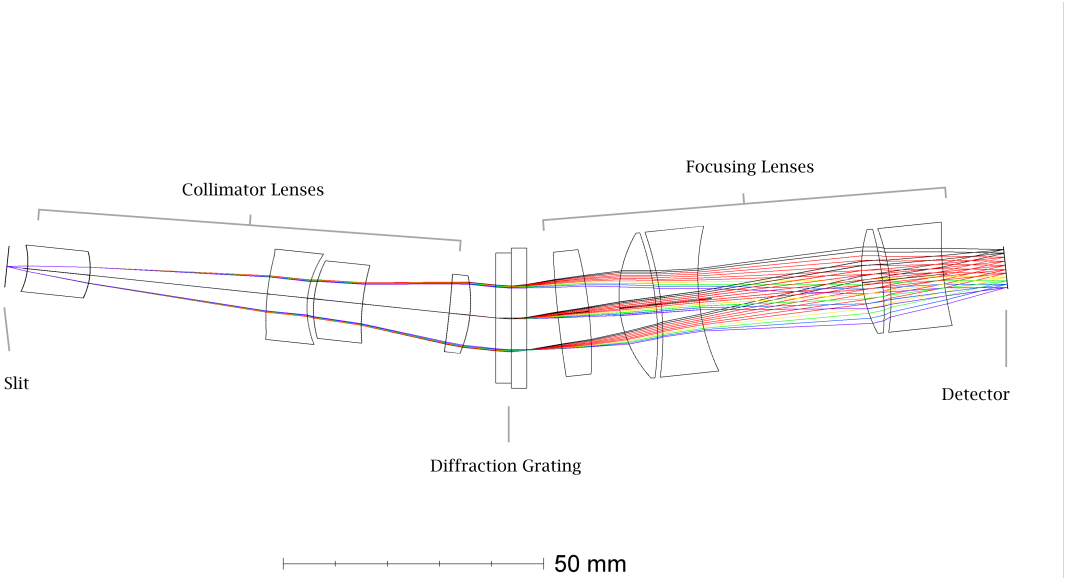

Figure 4.2: Optical layout of the custom-lens redesign of OpenHSI. The model was created to theoretically maximise both throughput and spectral fidelity.

features. These areas informed the design objectives of the custom optical model, which aimed to improve resolution and throughput without compromising the system's portability or modularity.

Three primary objectives informed this task: reducing the F# of the device to facilitate higher light collection and SNR, increasing spectral accuracy to ensure reliable data across the wavelength range, and enhancing image contrast to improve spatial resolution. This effort aimed to rebalance the inherent trade-offs in spectrograph design and further the optical performance of a system of this size. The redesigned model incorporated a custom lens system optimised for aberration control and was developed within the manageable physical footprint of a shoebox. This form factor ensured that the spectrometer remains portable and suitable for a range of research-based activities, including drone flights, static field captures, and laboratory work.

The optimisation process for this re-design was carried out using the Ansys OpticStudio (Zemax) software. This design relied on a framework of constraints to guide the iterative optimisation process, mostly aimed at ensuring the physical feasibility of the lenses. A numerical aperture (NA) of 0.25 was selected, corresponding to an F-number of 1.9, throughput higher than this was found to compromise the device's portability. Specific restrictions were implemented within the Merit Function Editor to control the optimisation process, including an effective focal length of 50 mm for the focusing lenses and 29 mm for the collimator lenses. These values produced a system magnification of approximately 1.75, resulting in a projected slit image height of 5.25 mm on the detector from the original 3 mm slit. Additional constraints included limits on lens thickness (kept below 12 mm to comply with manufacturing standards), curvature values greater than 1 to avoid structural overlap, and positive thickness values to ensure all elements were physically realisable(see Table 4.1.

4.2.1 Spot Diagram Analysis

An important aspect of evaluating the optimised design was the analysis of spot diagrams, which provide a visual representation of the system's ability to focus light across the field. These plots provide a visual representation of the system's ability to focus light and serve as a geometric approximation of the Point Spread Function (PSF). The PSF describes the spatial response of the system to a point source, effectively characterising the blur introduced by optical aberrations. The diagrams for the original OpenHSI show spot enlargement and aberrations at the edges of the slit and wavelength extremities, with spot sizes exceeding the Airy disc in several regions. The Airy disc, calculated from the system's F-number and central wavelength, approximates the smallest spot size achievable under diffraction-limited conditions. Achieving spot sizes close to this limit is important for maximising resolution and minimising optical aberrations.

In the optimised design (Figure 4.3), the matrix spot diagrams show tighter, more symmetric spot distributions across the field and wavelength range. Spot spread is noticeably reduced at shorter wavelengths, where chromatic aberration previously led to elongation and asymmetry. A key improvement is the system's ability to maintain sharp focus across all field positions and wavelengths across the detector plane. This consistent resolution reduces field-dependent variation in both spatial and spectral fidelity. As a result, the system is easier to calibrate and more reliable in producing spatially uniform hyperspectral data. Quantitatively, the RMS spot size at the centre field improved from 4.30 µm in the original OpenHSI to 1.33 μm in the optimised design; a reduction of approximately 69%. The tighter and more uniform spots help concentrate energy into fewer pixels, narrowing the PSF to reduce spatial crosstalk and enhance pixel-level resolution. These refinements contribute to improved spectral fidelity and more consistent spatial performance across the field, aligning the system more closely with the diffraction limit.

4.2.2 Spatial Resolution and MTF Analysis

The modulation transfer function (MTF), which quantifies contrast retention across spatial frequencies, reveals substantial improvements in the custom model's spatial resolution compared to the original design. Since real-world application MTF is limited by the pixel size of the detector, both models will be compared based on the detector used in the 2022 OpenHSI model (Sony IMX273 sensor) with 3.45μm pixel pitch. This equates to a Nyquist (limiting) frequency of ∼145 line pairs/mm at the detector. To assess the contrast ability of the device across the usable visible range, MTF values were averaged across 3 RGB channels shown in Figure 4.5. To better assess contrast across the full data cube, contrast values were also averaged across the slit. The custom-lens model achieved an 92% improved MTF@Nyquist value of 0.52 over the original OpenHSI model value of 0.27. Integration of this RGB MTF curve shows a 37% increase in area under the curve (AUC) (from 0.55 to 0.76), reflecting enhanced overall contrast transfer. These values reflect a significantly improved ability to resolve spatial contrast at high frequencies.

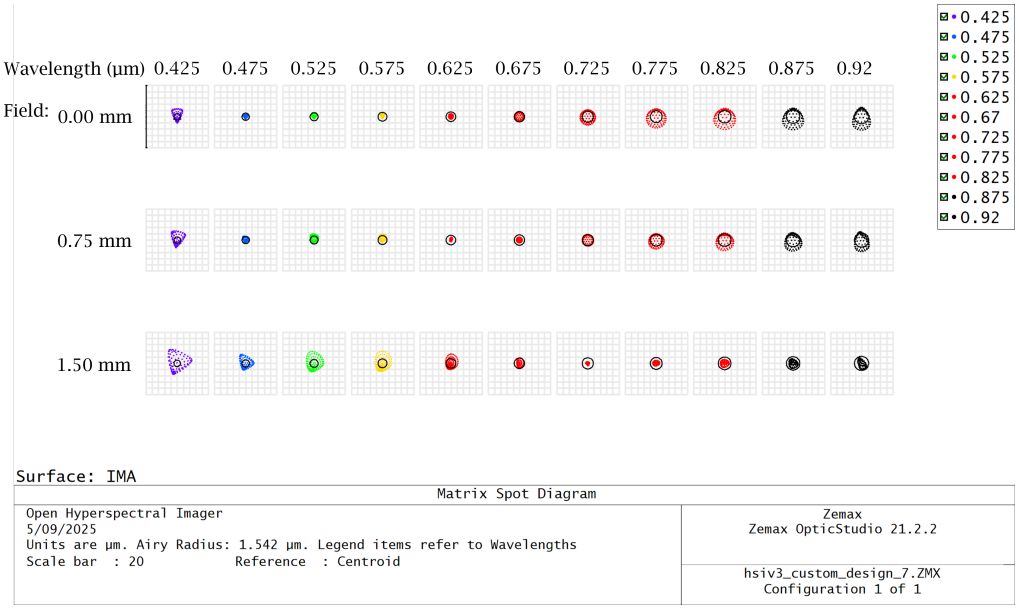

Figure 4.3: Matrix spot diagram of the custom hyperspectral imager lens design. Spots show ray intersections for 11 sampled wavelengths (425–920 nm) at three field positions (0, 0.75, and 1.5 mm off-axis). The dashed circle marks the Airy disk radius (1.54 µm), representing the diffraction limit. On-axis spots remain largely contained within the Airy circle, indicating near-diffraction-limited performance, while off-axis positions show modest chromatic spread but remain well-controlled across the field.

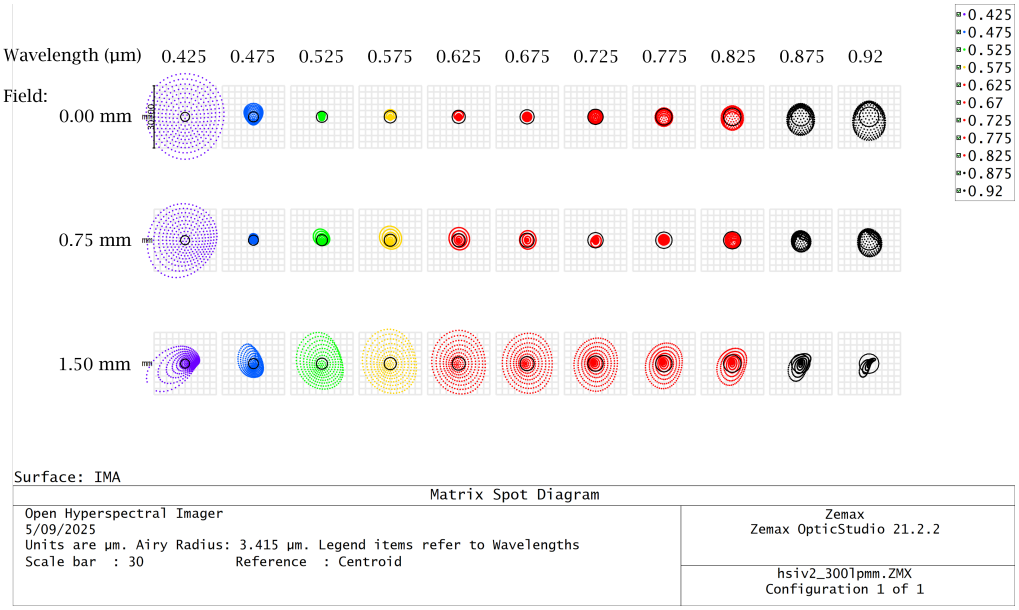

Figure 4.4: Matrix spot diagram of the foundation design OpenHSI for comparison.

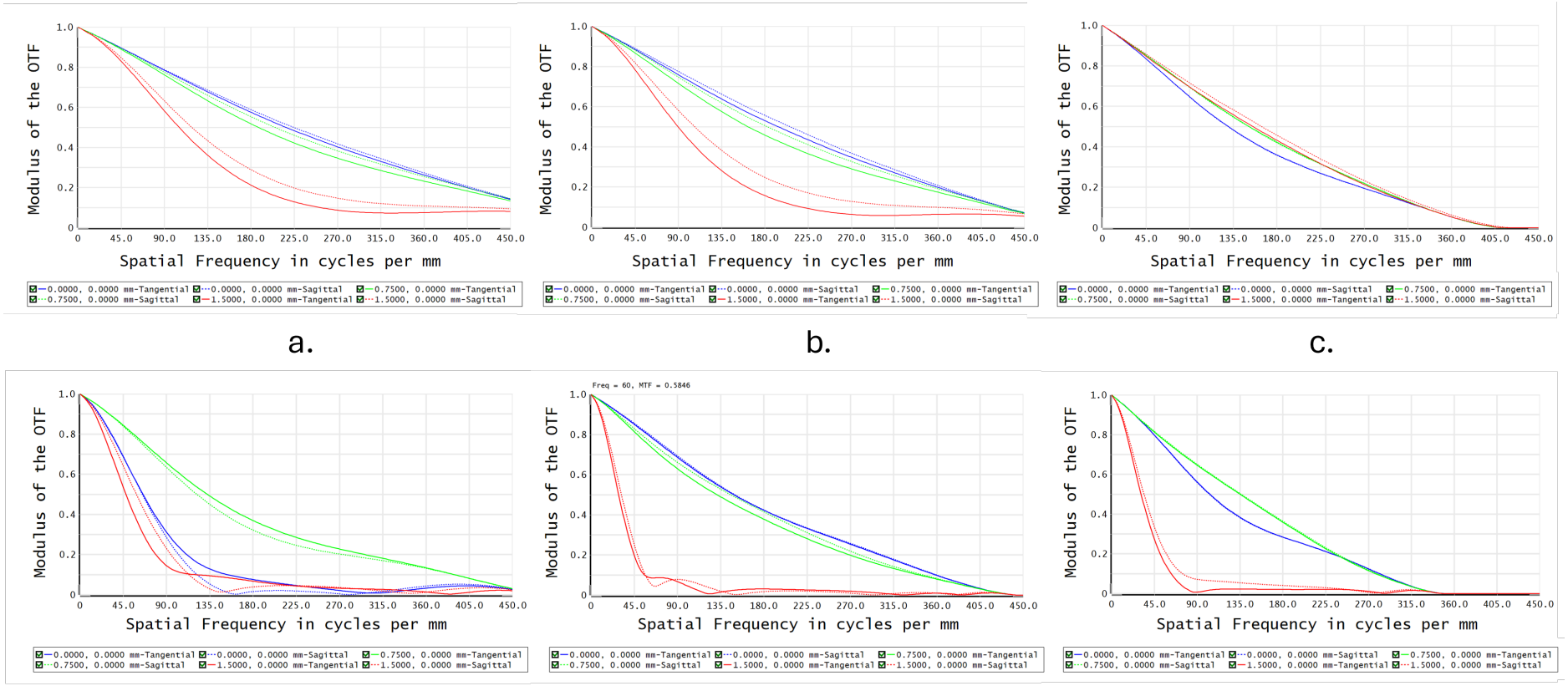

Figure 4.5: Modulation transfer function (MTF) of the custom-lens optical model at a representative blue (a.), green (b.) and red (c.) wavelength. OpenHSI data for blue (d.), green (e.) and red (f.) are included for comparison.

4.2.3 Aberration Balancing and Seidel Analysis

To further assess the optical performance of the custom model, a Seidel diagram was generated to visualise the contribution of third-order aberrations across the system. While individual components introduce significant spherical and coma aberrations, these are largely cancelled by opposing terms later in the optical path. This is reflected in the low net values in the `SUM` column of the diagram, which indicate effective aberration balancing through the lens stack. This cancellation is a direct consequence of the optimisation process, where surface curvatures and spacings were tuned to manage aberration propagation across the system.

The presence of strong intermediate terms alongside near-zero net aberrations is consistent with the observed improvements in RMS spot size and MTF performance. Figure 4.6 shows the Seidel aberration contributions for each surface in the custom design at a central wavelength of 625 nm.

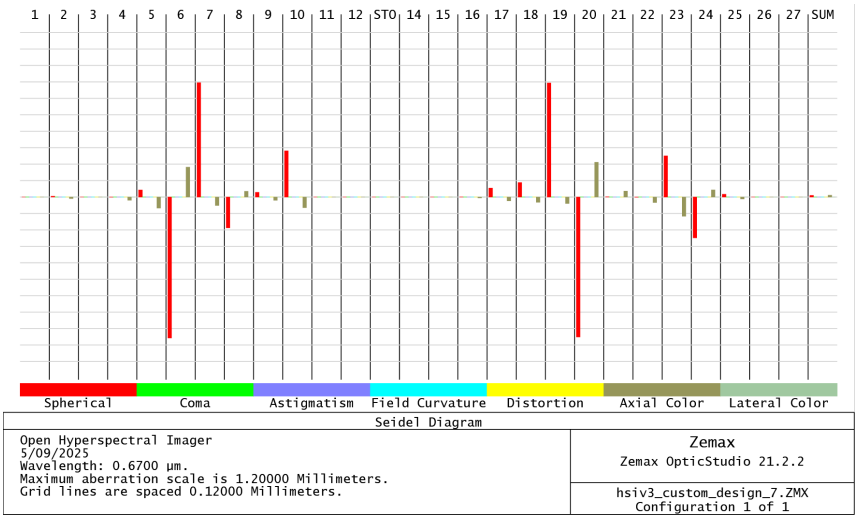

Figure 4.6: Seidel diagram of the custom optical model at $\lambda = 625$ nm, showing effective cancellation of spherical and coma aberrations across the system.

4.2.4 Optimisation Workflow and Merit Function Design

The optical design was refined in Zemax OpticStudio using a sequential merit function approach. The goal of the optimisation process was to balance key performance parameters; minimising spot size, improving focus uniformity, and preserving manufacturability and device footprint. The merit function was structured primarily around spot quality metrics. Core operands included transverse ray error minimisation (TRCX, TRCY) across multiple field points and wavelengths, which helped reduce geometric aberrations and tighten spot focus. While many of the low-level operands were automatically generated using Zemax's operand wizard, the broader structure was guided by the system goals. Final convergence was achieved at a merit function value of 0.112.

4.2.5 Material Selection and Coating Considerations

The choice of materials for the custom optical system was made manually based on optical performance requirements, manufacturability, and availability from com-

Parameter	Value / Constraint	Justification
Focusing lens EFL	50 mm	Required to achieve desired image magnification
Collimator lens EFL	29 mm	Balanced system size and projection onto detector
System magnification	∼1.75	Projects 3 mm slit to 5.25 mm on detector
Lens thickness	<12 mm	Matches COTS availability and mechanical tolerances
Surface curvature	>1	Avoids extreme or unmanufacturable geometries
F-number	1.9	Improves throughput without compromising compactness
Element spacing	Mechanically constrained	Determined by housing envelope and alignment clearance

Table 4.1: Summary of key optical and mechanical constraints used during design optimisation.

mercial suppliers. No automated glass substitution optimisation (e.g. Hammer) was applied, instead glasses were selected for their refractive indices, dispersion characteristics, and physical properties.

The final design includes a combination of crown and flint glasses such as N-BK7, N-SF11, N-FK5, and N-LAF33. Glasses with higher Abbe numbers, such as N-BK7 and N-FK5, were chosen to minimise chromatic dispersion and axial colour aberration. Lower Abbe number glasses like N-SF11 and N-LAF33 were used in complementary roles to balance the system and support achromatic correction. All materials used were compatible with typical manufacturing tolerances and could be sourced in common stock sizes.

Coatings were applied to nearly all lens surfaces to improve transmission and minimise reflection losses. Most elements use VIS-NIR broadband anti-reflective coatings (EO_VISNIR_673), for operation from 400–900 nm [113]. Several critical surfaces, particularly in early-stage and high-incidence-angle elements, used THORASLHA64, a specialty coating optimised for high transmission under low lighting conditions [113]. These coatings improve overall system throughput and can help reduce ghosting.

The selected materials also offer suitable thermal and mechanical stability for UAV deployment and field conditions. For instance, N-BK7 and N-FK5 exhibit low thermal expansion and high hardness, reducing sensitivity to alignment drift and mechanical stress. These properties can contribute to maintaining focus integrity and geometric consistency during extended imaging sessions. Table 4.2 provides a summary of the optical materials and coatings used in the design, including their roles in the lens configuration.

Material/Coating	Type	Purpose / Role
N-BK7	Crown glass	Low-dispersion element, general-purpose broadband optics
N-SF11	Flint glass	Dispersion balancing, used for chromatic correction
N-FK5	Fluor crown glass	Low-dispersion, supports achromatic correction in rear group
N-LAF33	Dense flint glass	High-index element, assists in compact folding and correction
EO_VISNIR_673	AR Coating	Broadband AR (400–900 nm), used on most lens surfaces
THORASLHA64	AR Coating	Specialty AR, enhanced NIR transmission, applied to key elements

Table 4.2: Optical materials and coatings used in the custom-lens design.

4.2.6 Summary of Custom Design Findings

The custom optical design explored here addressed key limitations of the original OpenHSI system by using bespoke lens geometries and constraint-driven optimisation in Zemax. The design targeted three core areas: increased light throughput via a faster F-number, improved spectral fidelity through achromatic correction, and more uniform spatial performance across the slit, as evidenced by consistent matrix spot diagrams. While spatial resolution improvements depend in part on the field lens and detector design, the simulated modulation transfer function (MTF) plots demonstrate greater contrast retention at high frequencies, particularly in off-axis regions.

Although the system was not fabricated, primarily due to the high cost of commissioning custom lens manufacturing, it serves as a validated simulation model. The results establish a clear optical pathway for future custom-lens hyperspectral imagers, with quantitative performance benchmarks.

The insights gained from this design process underscore the value of iterative simulation and performance-driven modelling in optical research. By combining accessible materials, geometric constraint management, and tailored coatings, the design remained manufacturable while demonstrating improvements in output quality. This work reinforces the potential of custom optics to meet the increasing demands of applications in low-light, high-contrast, and mobile imaging environments.

4.3 Improved Low-Cost Redesign of the OpenHSI System

To address the limitations of the OpenHSI system whilst still preserving affordability and accessibility, a new optical design was developed using only commercially available components. This model maintains the philosophy of the OpenHSI architecture but improves upon its spectral performance by redesigning the lens choices

and assembly. The goal was to create a replicable, field-ready spectrometer with improved spectral uniformity, retained spatial resolution, and a compact footprint suitable for UAV deployment, benchtop spectroscopy, or potential integration into cubeSAT payloads. The COTS model advances earlier work on the OpenHSI and Sigernes variants by correcting field-dependent aberrations and ensuring greater optical consistency across the image plane.

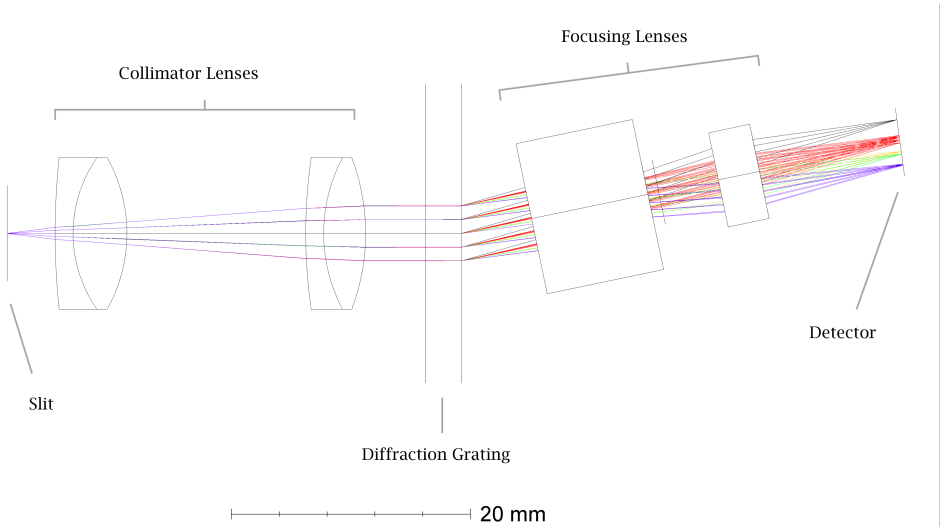

Figure 4.7: Final iteration of the optical layout of the COTS model shown via the simulated ray diagram. The model differs from its predecessor, the OpenHSI, in its use of achromatic lenses for collimation, an air gap at the slit and a tilt introduced at the detector plane.

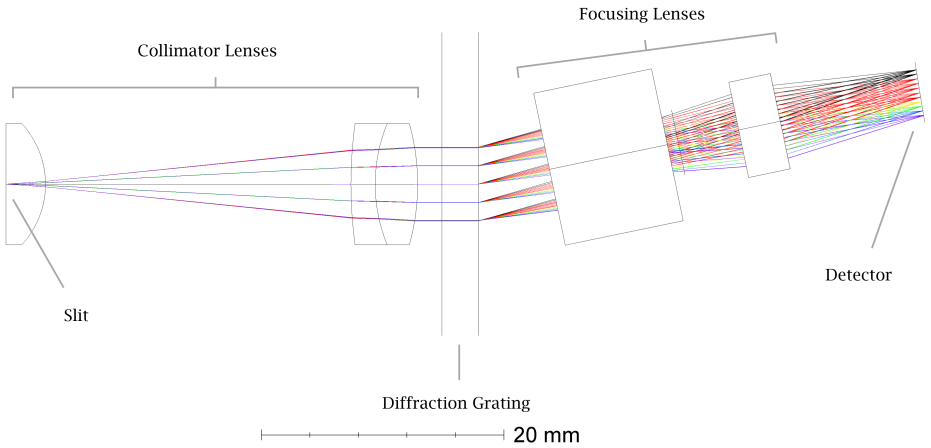

Figure 4.8: The ray diagram for the 2022 OpenHSI optical layout, used as the design baseline for the COTS model.

4.3.1 Design Philosophy and Implementation Constraints

The design followed strict constraints to balance cost, size, and performance. All optics, including lenses, gratings, and spacers, were sourced from COTS catalogs

from Edmund Optics and Thorlabs. The total system length was kept under 300 mm, with all lens diameters restricted to 12.7 mm. This miniaturisation preserved compatibility with small-scale imaging platforms, particularly UAVs and portable field units.

The target spectral resolution remained consistent with the original OpenHSI (1.5–2 nm), but the redesign focused on improving spectral uniformity across the slit and wavelength range. Field-dependent chromatic blur (particularly evident at the short-wavelength edges of the OpenHSI) was reduced by lens selection and layout.

These benefits came with several trade-offs. The use of COTS lenses constrained the available surface curvatures and materials, limiting the extent of aberration correction. Additionally, while higher-dispersion gratings could have improved spectral sampling, they would have spread light across more detector pixels, reducing per-pixel signal. This effect, especially under low-light conditions, would have compromised SNR. The selected grating (300 lines/mm) thus balanced spectral resolution with photon efficiency for outdoor or underwater environments. Overall, the COTS design offers a practical and portable solution with enhanced field performance while maintaining the accessibility and usability of the original OpenHSI system.

4.3.2 Optical Design and Zemax Optimisation

The baseline configuration of the COTS device was derived from the OpenHSI architecture, retaining its transmission grating and focusing assemblies. However, all optical parameters; focal lengths, lens separations, and tilt angles were iteratively adjusted in Zemax to minimise aberration and improve spectral focus. A ray diagram of the final COTS configuration is shown in Figure 4.7, and the original OpenHSI diagram in Figure 4.8. A key structural adjustment involved introducing a 4 mm

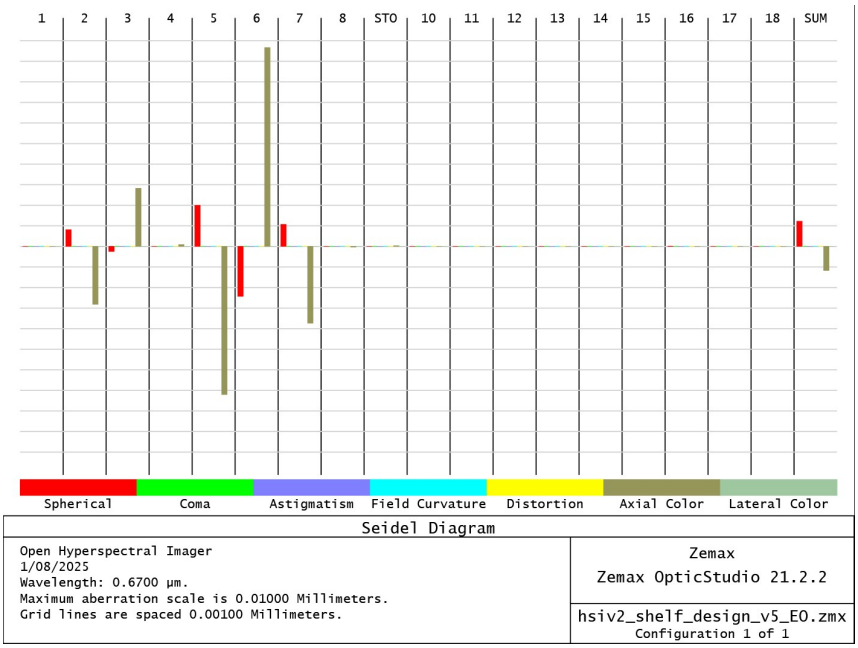

Figure 4.9: Seidel diagram for the COTS model at $\lambda = 670$ nm, showing individual aberration contributions and net cancellation effects.

gap between the slit and the first lens of the collimator. This spacing adjustment,

paired with the switch to achromatic collimating lenses (Edmund Optics #49-759 and #49-761), led to a 22% reduction in RMS spot radius at 550 nm (down from 15.3 μm to 11.9 μm) primarily by minimising spherical and axial chromatic aberrations. Compared to the plano-convex singlet used in the original OpenHSI, the doublet configuration offers better chromatic correction across the visible spectrum, particularly in edge field positions. To further optimise image focus and reduce field curvature, the focusing lens was tilted by 4° relative to the detector plane. This deviation introduces challenges in the physical device assembly, however produced greater image accuracy for the collimated light. The result is reduced spectral tilt and improved spectral line separation, particularly at shorter wavelengths where chromatic spread was largest.

The collimator assembly used a two-lens system consisting of a 19 mm and a 30 mm focal length achromatic doublet, spaced 4 mm apart. This arrangement ensured uniform collimation over the 400–900 nm range while preserving a compact mechanical footprint under 300 mm. Together, these design choices facilitated reduced chromatic blur, and delivered more consistent spectral performance across the image plane.

To support these findings, a Seidel diagram for the final optical configuration is presented in Figure 4.9. While there are aberration contributions, the total summed error remains low, particularly for spherical and chromatic components. This suggests that while some individual elements introduce aberrations, they are effectively compensated for downstream, validating the use of COTS components.

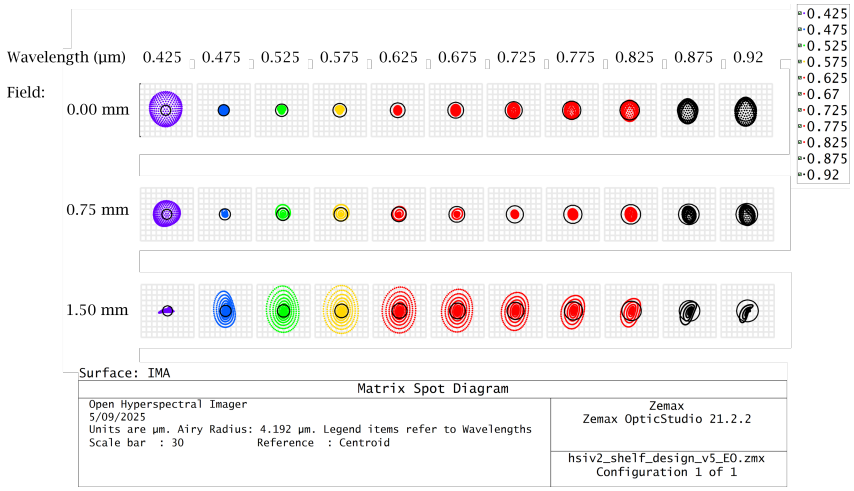

Figure 4.10: Matrix spot diagram of the COTS-based hyperspectral imager design. Spots are shown for 11 sampled wavelengths (425–920 nm) at three field positions (0, 0.75, and 1.5 mm off-axis). The dashed circles indicate the diffraction-limited Airy disk (radius = 4.19 µm). On-axis and mid-field positions show spots that remain largely contained within the Airy disk across most of the spectral range, while edge-field positions exhibit elongation and chromatic spread, particularly at shorter wavelengths.

4.3.3 Performance Validation: MTF and Spot Diagrams

The optical performance of the COTS-based model was verified through matrix spot diagrams and MTF analysis, benchmarked against the original OpenHSI design. Spot diagrams at key wavelengths (450 nm, 550 nm, and 750 nm) showed a 32% reduction in RMS spot radius at 550 nm (from 12.5 μm in OpenHSI to 8.5 μm in the COTS model) with improved shape symmetry and a sagittal-to-tangential ratio reduction from 1.8:1 to 1.2:1 (Figure 4.10). Compared to the diffraction-limited Airy radius at F/4 and 670 nm (approximately 3.27 μm), the COTS model's central RMS radius approaches 2.6× the limit, while OpenHSI exceeds 3.8×, indicating improved proximity to the diffraction limit. This symmetry reduces keystone distortion and spectral smearing across the slit.

MTF Performance

The modulation transfer function (MTF) analysis of the optical performance at red, green and blue wavelengths is highlighted in Figure 4.11. This design was also benchmarked against the SONY IMX273 sensor for detector-limited spatial performance and achieved very similar results to the OpenHSI model. Averaged across the three wavelength channels, the COTS redesign achieved contrast at the Nyquist limit of 0.27, identical to the OpenHSI value. Similarly, AUC for this device was marginally improved from 0.54 to 0.56, showing a small increase in overall spatial resolution. This was not a targeted area for improvement for this model, as the device was designed with a focus on downstream data fusion for spatial resolution enhancement, as detailed in Chapter 6.

4.3.4 Component Rationale and Trade-Offs

Component selection for the COTS model was guided by practical performance trade-offs and the need for accessibility. Achromatic doublets were used in both the collimator, and were preferred over singlets or aspheric elements due to their superior chromatic correction and more predictable off-axis performance. Their cost efficiency also supported the project's goals, with common Edmund and Thorlabs models priced at approximately $95 per lens, compared to over $300 for equivalent aspheric alternatives.

A 300 lines/mm transmission grating (Thorlabs GR25-0610, or Edmund Optics equivalent)[114] was chosen to balance spectral resolution and signal throughput. While higher groove densities offer narrower dispersion bands, they also spread light over more detector pixels, lowering signal intensity per band and reducing signal-to-noise ratio (SNR), a drawback particularly relevant for UAV or low-light applications. The focusing lens was inherited from the OpenHSI design due to its proven low-cost performance, and a slit width of 20 μm was selected to maximise spectral resolution where spatial information would be added in post-processing through data fusion.

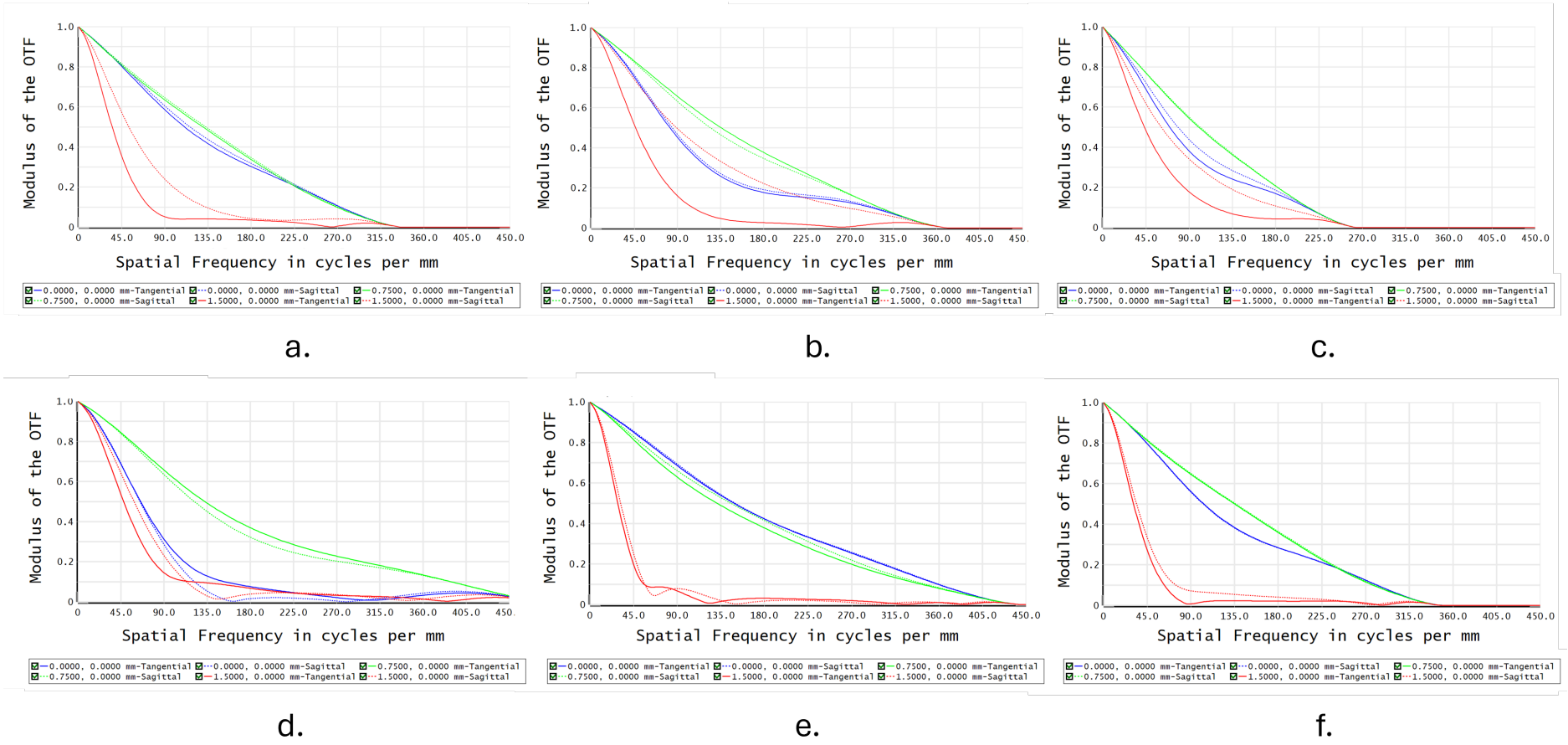

Figure 4.11: Modulation transfer function (MTF) of the COTS-redesign optical model at a representative blue (a.), green (b.) and red (c.) wavelength. OpenHSI data for blue (d.), green (e.) and red (f.) are included for comparison.

4.3.5 Final Optical Layout and Transition to Dual-Imager System

Compared to previous open-source imagers such as OpenHSI and the Sigernes design, this system achieves improved off-axis resolution uniformity, reduced chromatic aberration, and enhanced image stability. The improved field consistency provides a more stable optical baseline for the fusion algorithm introduced in Chapter 1.2. Together, these hardware refinements form the necessary foundation for real-time image acquisition and spectral-spatial post-processing.

The culmination of the optical development process is shown in Figure 4.12, which presents the final dual-modality hyperspectral system. This compact assembly integrates the COTS-based spectrometer module alongside a co-aligned panchromatic imaging channel and forms the foundation for the single-device pansharpening method developed in Chapter 1.2. The housing incorporates the mechanical adjustments discussed earlier, including a 4° detector tilt and compact lens spacing, while preserving modularity for sensor and optic interchangeability.

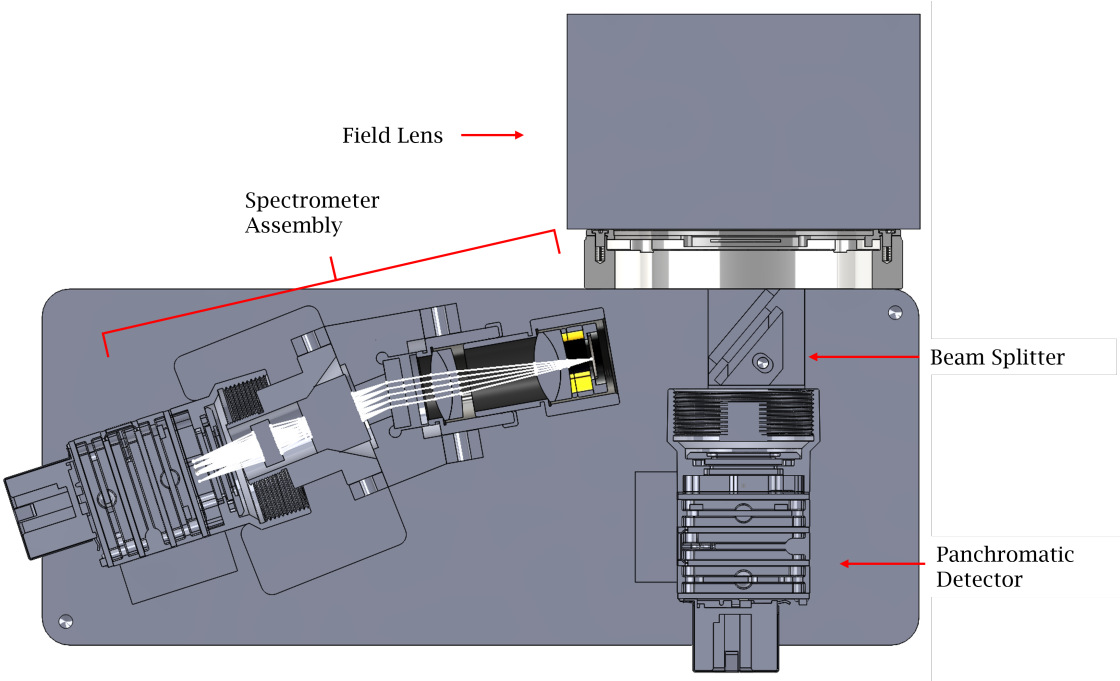

Figure 4.12: Full optical and mechanical assembly of the dual-imager hyperspectral device, showing the spectrometer ray simulation, splitter and panchromatic detector layout. A placeholder is used for the telescope lens.

Chapter 5

Hybrid Panchromatic Hyperspectral (HyPAN) Imager

5.1 Introduction

This chapter presents the transition from optical design to the physical implementation of the hyperspectral imaging device. Building on the design principles established in Chapter 4, the work here focuses on model design, assembly, and calibration of the system using the OpenHSI-derived, open-source framework.

The performance of a hyperspectral imager depends not only on its optical layout but also on its mechanical stability and assembly repeatability. These factors are particularly critical for UAV integration, where the system must withstand high-frequency vibrations from rotors and temperature fluctuations during flight. Consequently, the mechanical design prioritises rigidity to maintain optical alignment and heat-sinking material choice to withstand these dynamic conditions. The following sections describe the development of the device's mechanical layout, with attention to alignment and mounting strategies compatible with gimbal stabilisation. Iterative prototyping was used to identify practical limitations such as machining tolerances, component interference, and alignment complexity.

Beyond assembly, calibration of the device for wavelength, radiance, spectral windowing and aberration correction are detailed, alongside 1st-level processed datacube captures. This chapter establishes the opto-mechanical foundation of the dual-imager system described in Chapter 4(HyPAN), and completes the transition from theoretical design to a reproducible, field-deployable instrument.

5.1.1 Motivation and System Overview

The device developed in this chapter represents a shift in open-source hyperspectral imaging, combining a spectral imager with a co-registered panchromatic camera into a single, compact unit. This hybrid configuration supports both real-time scene interrogation and post-capture enhancement, addressing key limitations in spatial resolution, responsiveness, and integration faced by conventional HSI systems.

Current open-source imagers such as OpenHSI offer spectral resolution at low cost,

(a) Opteka 500 mm f/6.3 reflex lens **(b)** Nikon 50 mm f/1.8 standard lens

Figure 5.1: The field lenses from early development models (left) to the final device design (right). The Nikon lens was settled on for its high throughput, and short-range imaging for contrast-target assessment.

but suffer from anisotropic spatial sampling due to the pushbroom architecture. Spatial information is unevenly distributed across slit and scan axes, reducing the effective resolution of identifiable features. By introducing a panchromatic imaging channel that is co-aligned with the spectrometer slit, the device enables pansharpening correction on a datacube that is easily co-registered and captured live at the scene. As such, the Hypan device improves the spatial information of the final datacube product without the introduction of secondary devices or imagery.

Beyond post-processing, the panchromatic sensor also supports real-time visualisation and targeting. This capability allows users to navigate scenes, identify regions of interest via a live video feed, and position the slit accordingly, streamlining the capture process in field deployment. Complementing the scanning spectrometer with this live panchromatic feed thus reduces the amount of unneeded data in the raw datacube. This is a capability not currently available in small-scale or open-source HSI devices, which often require separate RGB cameras or blind scanning. The form factor of this device also ensures that it can be affixed to a wide range of rotational gimbals or stages.

5.1.2 Field Lens Design and Iterative Refinement

The field lens defines the incoming field of view (FOV) and directly influences light collection and spatial resolution in the final image. Early iterations of the Hypan device used the Opteka 500 mm f/6.3 reflex lens (hybrid mirror/refractive), selected for its long focal length and compatibility with T-mount adapters. This configuration was suitable for long-range remote sensing tests, producing datacubes of distant targets with minimal geometric distortion. However, its extremely narrow FOV (approximately 0.5°) and large physical footprint proved impractical for laboratory setups or low-altitude UAV imaging, prompting a transition to a more versatile lens.

The final device adopted the Nikon 50 mm f/1.8 lens. This shift enabled wider field coverage and improved light throughput, better aligning with the needs of aerial and field-based imaging. The f/1.8 aperture collects more light , improving SNR under overcast or dusk conditions. The Nikon F-mount standard (46.5 mm flange distance) also provides enough mechanical clearance for beam splitter insertion while supporting a wide range of alternative lenses.

At an imaging altitude of 50 m, the Nikon 50 mm lens and Sony IMX273 sensor (3.45 µm pixel pitch) achieve a theoretical across-track ground sampling distance (GSD) of approximately 0.35 cm per pixel.

$$\text{GSD} = \frac{\text{Pixel Pitch} \times \text{Altitude}}{\text{Focal Length}} = \frac{3.45 \times 10^{-6} \times 50}{0.050} = 0.00345 \text{ m} = 0.35 \text{ cm} \quad (5.1)$$

It is important to note that this value applies strictly to the spatial dimension perpendicular to the flight path. For pushbroom scanners, the along-track resolution is instead governed by the platform's flight speed and the detector's frame rate. To achieve isotropic (square) pixels, the integration time must be matched to the ground speed such that the platform moves exactly one GSD unit per exposure. Any deviation results in spatial anisotropy, via pixel-stretching or -squashing, which highlights the need for this project's pansharpening process to restore spatial consistency.

This resolution enables detection of sub-centimeter features in UAV-based coastal surveys, such as sediment transitions or fine vegetation structure. While environmental and motion blur factors may slightly reduce effective resolution, the lens selection offers a practical balance between sharpness, light collection, and system compactness.

5.1.3 Beam Splitter Integration and Dual-Modality Optimisation

A 75R/25T visible-band plate beamsplitter (12.5 × 17.5 mm, N-BK7, 1 mm thick) was positioned directly after the field lens to divide the incoming light between the hyperspectral and panchromatic imaging paths. The 75 % reflectance prioritises signal-to-noise ratio (SNR) in the hyperspectral channel, where optical losses more directly impact the quality of spectral data. By contrast, the panchromatic channel is used solely for spatial detail, and thus tolerates reduced light intensity.

The splitter was mounted at 45°, the standard angle for planar beam separation, using a custom 3D-printed bracket shown in Figure 5.10. This angle provided efficient beam path separation with minimal complexity in component overlap. While polarisation sensitivity can affect splitting ratios at oblique incidence, no practical artefacts were observed during imaging tests, and no further correction was required in the current configuration. The fixed-angle splitter ensures co-aligned optical axes between the two paths. While this provides a stable baseline for the overlapping fields of view, minor variations in sensor positioning and path-specific magnification necessitate the software-based co-registration described in Chapter 6.

5.1.4 Slit Optimisation and Spacer Geometry

The entrance slit sets the instantaneous field of view (IFOV) and the line-spread function (LSF) in a pushbroom spectrograph. We replaced the OpenHSI's 25 μm slit with a 20 μm slit to tighten the LSF and improve spectral separability. Under first-order imaging, the angular IFOV in the slit direction is

$$\theta_{\mathrm{IFOV}} \approx 2 \arctan\left(\frac{w/2}{f_{\mathrm{coll}}}\right), \tag{5.2}$$

where w is the slit width and f_{coll} is the collimator focal length. With $f_{\mathrm{coll}} = 29$ mm, the 25 μm and 20 μm slits give

$$\theta_{\mathrm{IFOV}}(25\ \mu\mathrm{m}) \approx 0.025^\circ, \qquad \theta_{\mathrm{IFOV}}(20\ \mu\mathrm{m}) \approx 0.020^\circ,$$

an 18% reduction in IFOV. Consistent with this reduction, the calibrated spectral sampling reached $\Delta\lambda \approx 0.44$ nm/pixel, reflecting the narrower LSF.

The throughput trade-off follows directly from the slit width. For uniform irradiance at the slit plane, photon flux scales linearly with w; moving from 25 μm to 20 μm therefore reduces flux by a factor of 0.8. The associated SNR impact depends on the noise regime: in the shot-noise limit, SNR $\propto \sqrt{N}$ (a $\sim$10.6% decrease), whereas in a read-noise-limited regime SNR $\propto N$ (a 20% decrease). In practice, the SNR change will lie between these bounds and varies with scene brightness and exposure. In Chapter 6.1 we show that while a narrower slit reduces photons, the downstream pansharpening recovers spatial sharpness loss by fusing with the high-SNR panchromatic channel; we therefore prioritised spectral fidelity at the slit while restoring spatial detail in post-processing.

5.1.5 Dual-Detector Integration and Panchromatic Enhancement

The HyPAN system uses a dual-detector layout to capture hyperspectral and panchromatic data from the same field lens. Both channels use the LUCID Phoenix camera with the Sony IMX273 global-shutter CMOS sensor (1.58 MP, 1456 × 1088, 3.45 µm pixels). The sensor achieves up to 226 fps at 10-bit depth, enabling short exposures when needed for bright daytime captures, and to support fast-moving UAV scans.

However, operating at this maximum frame rate generates data volumes that can overwhelm standard onboard storage (>400MB/s for captures). Capturing both streams simultaneously requires high-speed write capabilities to prevent data loss. For this research, a raw data logging approach was used, with all processing performed offline. To achieve real-time pansharpening on a UAV, the system would require a powerful onboard computer with dedicated acceleration to handle the computational load of the fusion algorithm during flight.

Shared sensor architecture ensures consistent pixel size and layout, simplifying calibration and image processing. The hyperspectral arm records a spatially scaled version of the scene due to spectrograph magnification, whereas the panchromatic arm captures a larger full-scale view. The hyperspectral detector records 1080 across-track spatial channels and 1440 spectral channels per scan line, supporting high spectral resolution when paired with the 20 µm slit.

Specification	Value
Camera Model	LUCID Phoenix
Sensor Model	Sony IMX273 CMOS (Global Shutter)
Resolution	1456 × 1088 pixels (1.58 MP)
Pixel Size	3.45 µm
Max Frame Rate (10-bit)	226 fps
Shutter Type	Global

Table 5.1: Key specifications of the LUCID Phoenix IMX273 camera used in both imaging channels.

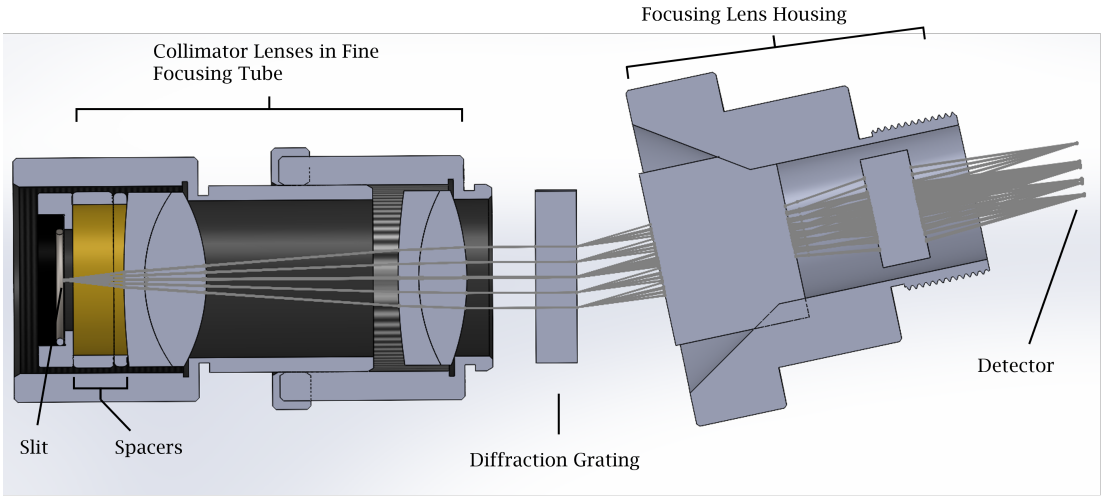

Figure 5.2: 3D render of the HyPan imager layout, Figure 4.7 with lens tube assembly from Solidworks.

Lateral alignment of the panchromatic detector was achieved via a precision shim, and longitudinal alignment via M2 mounting troughs in the aluminum baseplate. Further focusing adjustments are covered in Section 5.2. In operation, each channel records data simultaneously, this architecture keeps the system compact and self-contained.

5.1.6 Opto-mechanical Assembly

The opto-mechanical assembly of the HyPAN system brings together the optical subassemblies, detectors, and mechanical interfaces into a compact, field-deployable form. This section traces the progression from early prototypes to the final configuration, focusing on alignment strategies, modularity, and ease of manufacture.

To stabilise collimation and maintain repeatable alignment, we fixed the 4 mm mechanical gap between the slit and the first achromatic doublet (Edmund Optics #49-759), implemented with SM05 precision spacers (1 mm and 3 mm). This spacer geometry was selected from a Zemax sweep for optimisations as per §4.3.2.

The collimator assembly, positioned between the entrance slit and the diffraction grating, was implemented using Thorlabs SM05 lens tubes: a fixed-length SM05L05 (5 mm) and a variable-length SM05V05 (5–7 mm). The variable tube provided fine adjustment of the collimator separation during focusing, allowing small changes

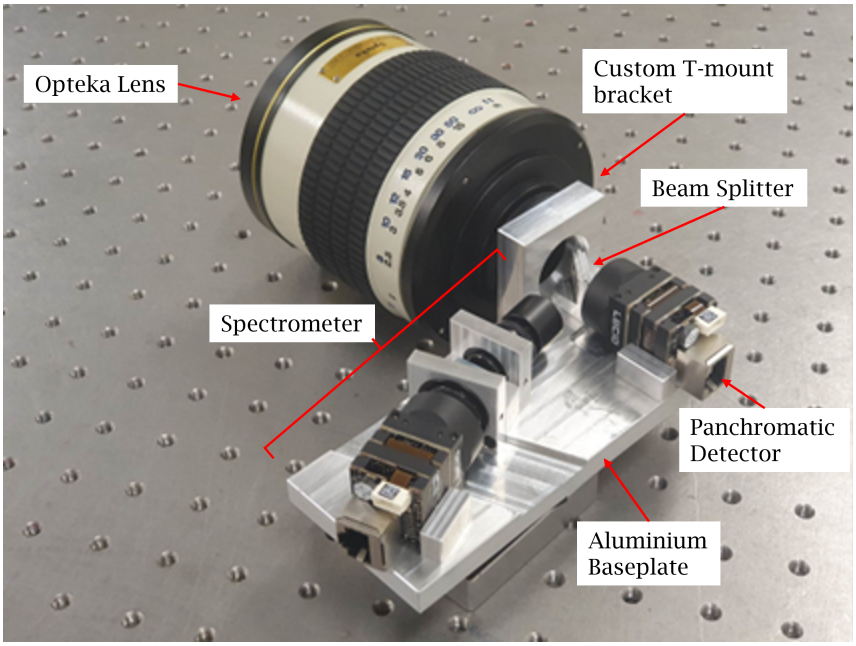

Figure 5.3: First manufactured HyPAN prototype using the Opteka 500 mm lens, attached via an Aluminium thread-milled adapter bracket. The device is mounted on a custom Al baseplate with alignment blocks for detectors, a trough-guided grating-unit and collimator and focusing assemblies either side.

in image distance without re-assembling the housing. Because the SM05V05 uses helical threading, length adjustments also rotate the mounted optics, changing the slit orientation. To decouple these effects, the grating block was machined with an integral cylindrical bore sized to closely fit the collimator tube but allow movement (Figure 5.9). A grub screw secures the tube once the slit is rotationally aligned, allowing the optical spacing to be adjusted without disturbing slit orientation.

The field lens mounting was developed through three design iterations. The first used a monolithic aluminium plate integrating the lens mount, detector mounts, and grating block. Unfortunately the embedded threads for the lens adapter and milled alignment troughs for the detectors increased machining complexity and limited flexibility for future changes. The design evolved to a modular layout in which the lens mount, detector brackets, and optical blocks were machined separately and secured to a flat baseplate with M3 counterbores.

The first functional prototype used the Opteka 500 mm f/6.3 telephoto lens, chosen for its long back focal distance (120 mm), which allowed clearance for the panchromatic detector's C-mount housing. A T-mount to SM1 adapter (Edmund Optics TMA1) connected the lens to a custom aluminium bracket fixed to the baseplate. This setup was effective for long-range field imaging but was bulky too for UAV payloads and unsuitable for short-range USAF target-based laboratory MTF testing, which required a wider field of view. The final configuration adopted a Nikon 50 mm f/1.8 F-mount lens, reducing the back focal distance to 46.5 mm and enabling a more compact optical path. The F-mount was secured using a modified commercial adapter (Figure 5.4) with SM2 thread flange removed and M3 counterbores machined directly into the body, allowing the lens to bolt directly to the baseplate without intermediate brackets.

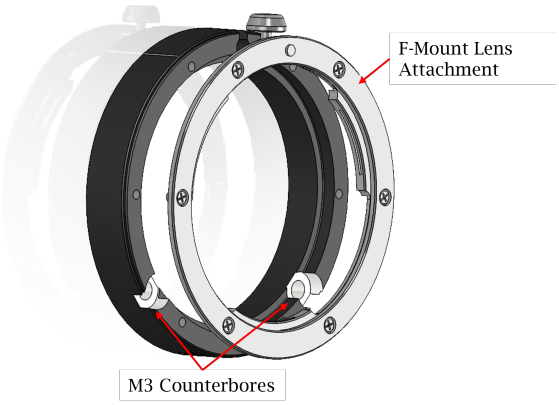

Figure 5.4: Modified F-mount adapter with M3 counterbore holes to screw into device baseplate. The adapter originally converted F-mount lenses to SM2 thread, however the threaded component of the product was milled off, and holes drilled through the base to attach the lens directly to the device.

5.1.7 Baseplate Development

The baseplate, serving as the structural foundation of the HyPAN imaging system, progressed through three design iterations (Versions 1–3) to balance manufacturing feasibility, optical alignment stability, and easy component replacement. Each version built on the lessons of its predecessor, refining the arrangement of optical and mechanical components for both laboratory and field use.

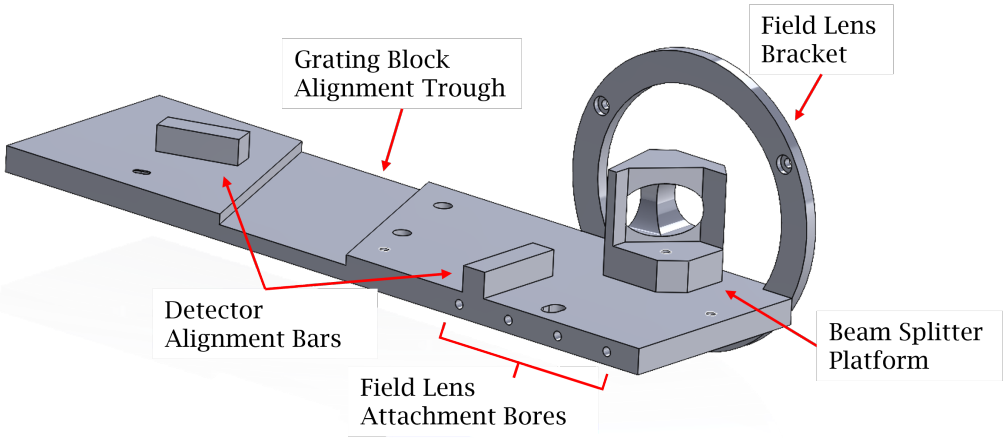

Figure 5.5: Version 1 baseplate — unibody design with integrated mounts for the field lens, detectors, and beam splitter.

Version 1 (Figure 5.6) adopted a unibody aluminium structure that integrated the beam splitter block, field lens mount, and detector alignment features into a single milled component (Figure 5.5). Two detector alignment blocks were incorporated to prevent rotation around the M2 mounting points, and a milled trough accommodated the C-mount housing of the hyperspectral sensor. This trough also served as an alignment reference for the grating block for added security. The panchromatic detector mount omitted the trough as the field lens back-focal distance required removal of its C-mount housing. Although this approach reduced assembly com-

plexity, the requirement to machine all features from a single block made the design complicated for manufacture. As a result, Version 1 remained at the CAD stage and was never produced.

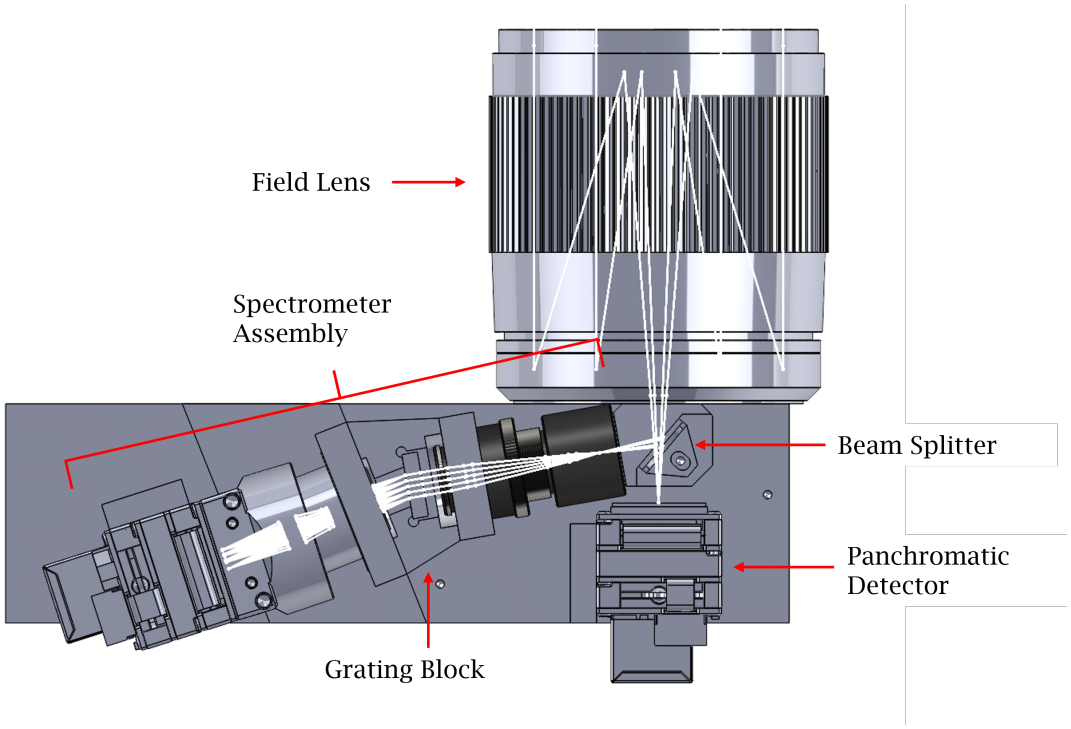

Figure 5.6: Version 1 3D model top-down view showing ray diagram and attached device components. The beam-splitter block and field lens attachment were both designed as part of the unibody plate, with the grating block attached via M3 bores, and aligned through a diagonal trough.

Version 2 moved to a modular architecture (Figure 5.7), separating the splitter block, detector brackets, and field lens mount from the baseplate. This allowed individual components to be replaced independently, improving adaptability. The revised plate included two machined troughs for grating block alignment and M3 counterbores to secure the modular components. Machined from a 10 mm aluminium block, the design offered increased thermal absorption and provided a stable platform for optical alignment. The optical path in this version used the Opteka 500 mm f/6.3 lens, whose 120 mm back focal distance accommodated the panchromatic detector's C-mount housing without modification. To reduce stray light and provide limited environmental protection, a 3D-printed PETG light hood was added, enclosing the full device.

Finally Version 3 refined this modular design, improving on compactness and rigidity (Figure 5.8). The baseplate thickness was increased to 20 mm, which provided greater stiffness and allowed the integration of a 1/4"-20 UNC threaded insert for direct mounting to tripods, UAV gimbals, or other fixtures. Additional M2 counterbores in the detector brackets improved stability with extra anchor points, and a slotted panchromatic sensor bore offered ±2.5 mm axial adjustment to fine-tune focus when paired with the Nikon 50 mm f/1.8 lens. Meeting this lens's 46.5 mm back focal distance required milling off the C-mount bracket from the panchromatic detector. The light hood (Figure 5.8a) was also redesigned with a small overhanging

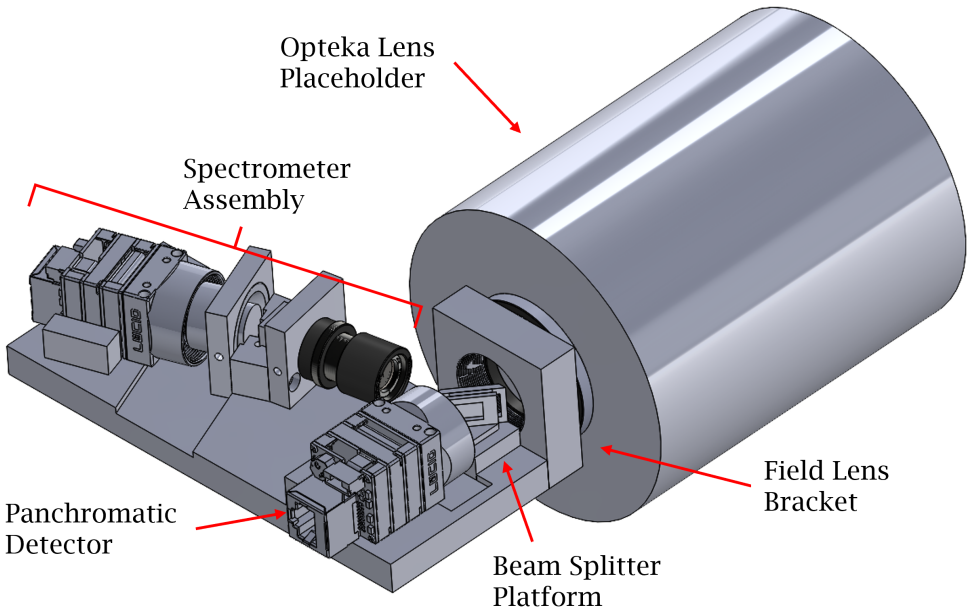

Figure 5.7: Version 2 3D layout with modular baseplate, beam splitter platform and field lens bracket units attached via M3 bores. Troughs are milled to assist component alignment and create room for C-mount flanges of detectors. A placeholder is used for the Opteka 500 mm lens.

lip and rounded corners to improve security. M3 counterbores were added at diagonal corners to secure it to the baseplate. These refinements produced a compact, rigid, and easily serviceable assembly. This configuration forms the platform used for focusing, wavelength calibration, and radiance calibration in Section 5.2.

5.1.8 Grating Block

The grating block formed the structural core of the spectrometer, securing the collimator, diffraction grating, and focusing optics in a rigid unit (Figure 5.9). Machined from three aluminium sections: a front collar for the collimator tube, a central recess for the 300 l/mm transmission grating, and a rear socket for the focusing lens assembly. The grating was mounted at an 11° blaze angle, matching the manufacturer's specified peak efficiency for 400–900 nm, and fixed in place using UV-cured optical adhesive (Norland NOA61). Both the collimator and focusing tubes were held by M1.6 grub screws, with ±2 mm of axial translation for focus adjustment during assembly.

5.1.9 Beam Splitter Block

The beam splitter block, shown in Figure 5.10, was designed as a modular component to partition light between the hyperspectral and panchromatic imaging paths. The aluminium frame incorporated a precision-machined slot to secure the 12.5 × 17.5 mm N-BK7 beamsplitter plate, allowing easy removal for maintenance or replacement. The slot also accommodated plate thicknesses between 1 mm and 3 mm, to allow alternative coatings or R/T ratios that may come in different forms. The block was mounted to the baseplate via a single M3 counterbore, with a milled

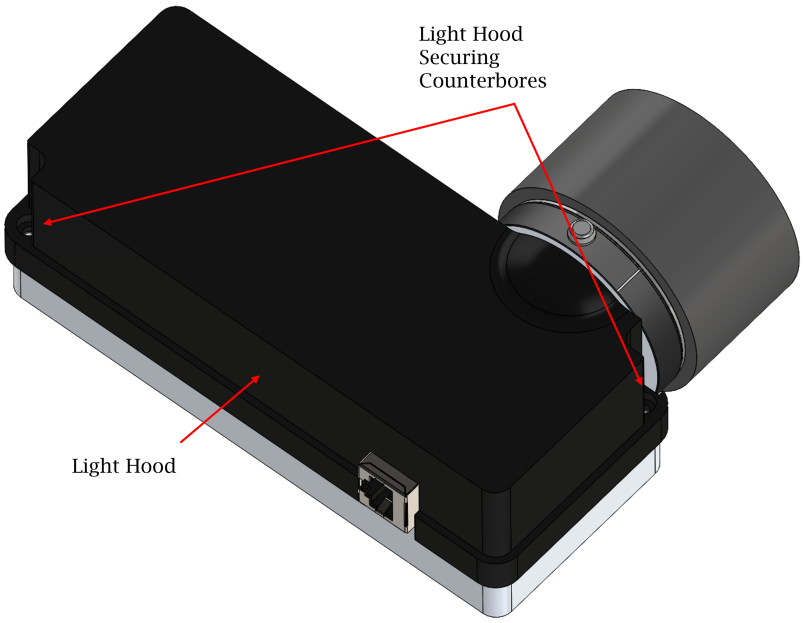

(a) Version 3 model including 3D-printed light excluder.

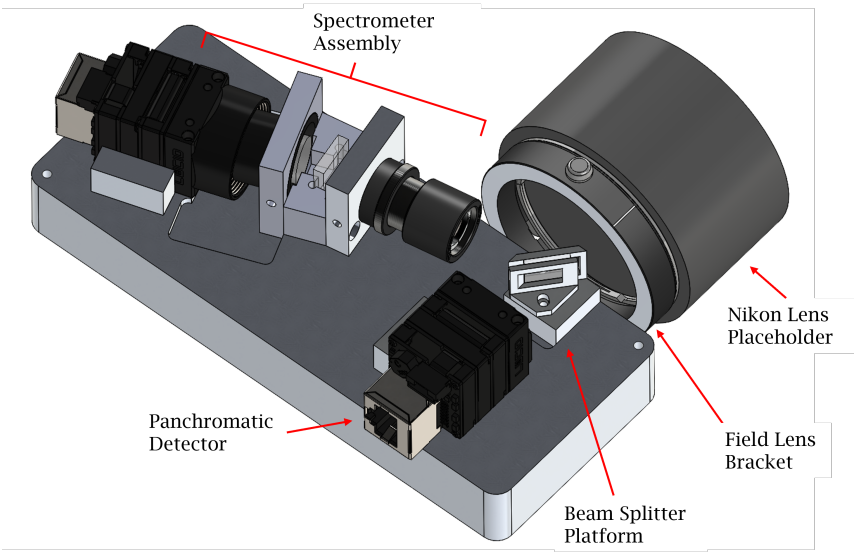

(b) Version 3 model showing internal components.

Figure 5.8: The final iteration of the HyPan device with (a.) and without (b.) the light hood for image capture. The design shows the C-mount flange milled off the panchromatic detector and the newly-added, customised F-mount adapter. A placeholder lens is used in place of the Nikon 50mm field lens.

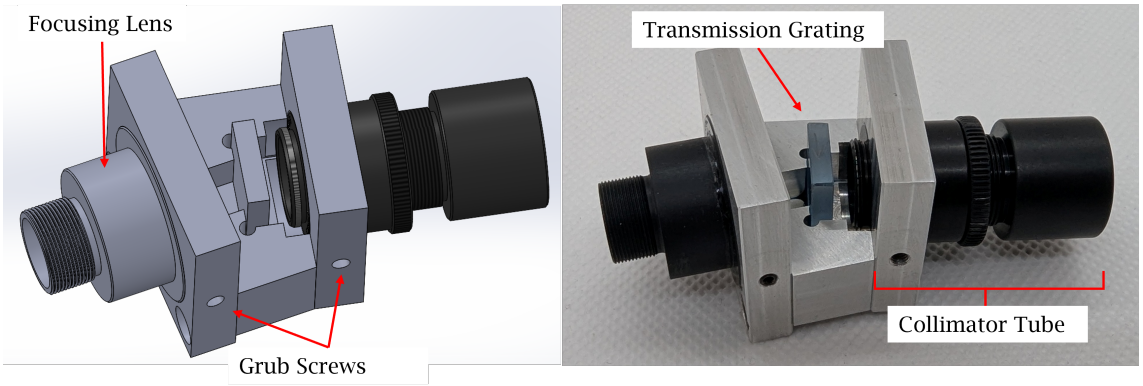

Figure 5.9: 3D model and Al-machined final product of the grating block showing the collimator collar, grating recess, and focusing lens socket.

alignment trough ensuring consistent location relative to both detectors. An excess section of platform aluminium was left on the physical model to add rigidity in the baseplate.

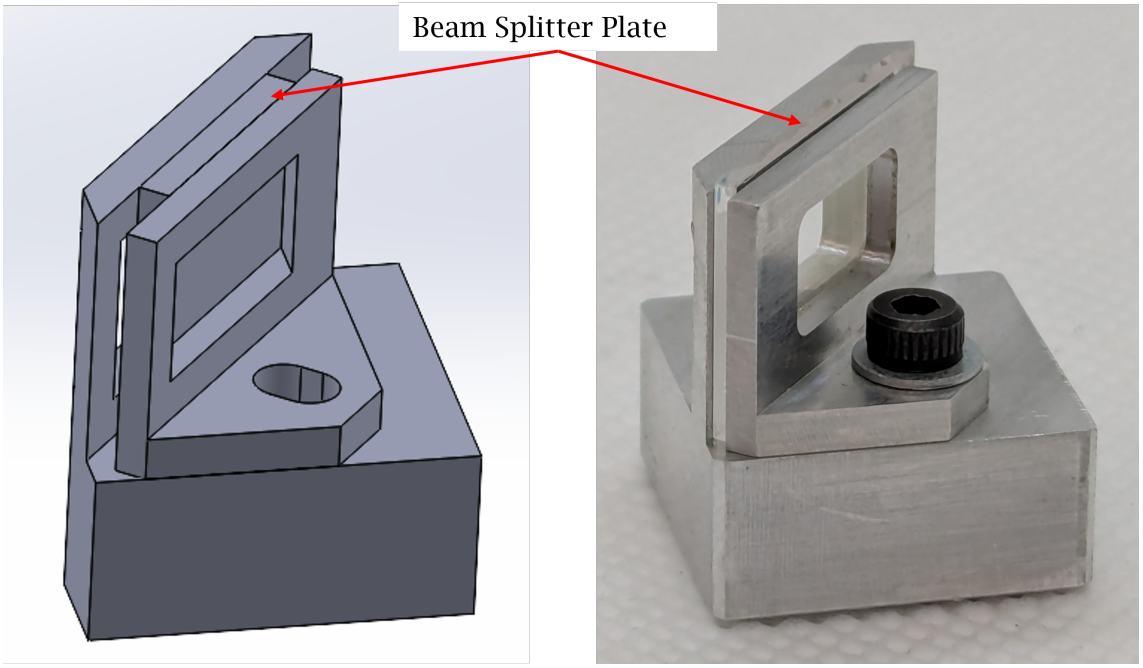

Figure 5.10: 3D model of the beam splitter block showing the platform unit and rear mounting bracket. The rear bracket is secured in place with an M1.5 screw through an adjustable trough, accommodating plates of varying thicknesses.

Overall, the evolution from Version 1 to Version 3 reflects a shift from an over-integrated, fabrication-intensive concept to a modular architecture that can be manufactured using standard CNC processes. The final design can be assembled with basic tooling, and adapted to different optical configurations without sacrificing stability.

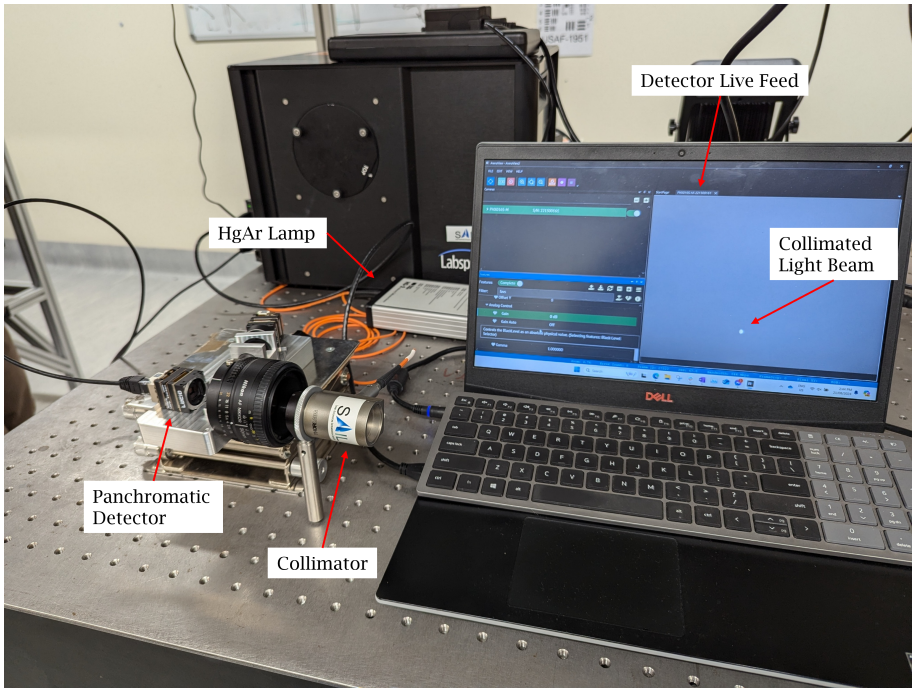

Figure 5.11: Panchromatic detector focusing using an FC/APC collimator and Hg-Ar light source. The white dot on the display corresponds to the collimated point-source used as the focus target. The light source is fed to the collimator which is mounted at the field lens, while the panchromatic detector is adjusted to maximise image focus.

5.2 Calibration and Focusing

The HyPAN system employs a beam splitter to direct part of the incoming light to a spectrometer and transmit the remainder to a panchromatic detector for pansharpening. To ensure accurate spatial-spectral registration, the focusing procedures for the two detectors were performed together.

The panchromatic detector was focused first using an FC/APC-connectorised UV-enhanced aluminium reflective collimator (Thorlabs RC12APC-F01) coupled via optical fibre to an Hg-Ar arc lamp (Ocean Insight HG-2). Light from the lamp was directed through the field lens to form a simulated point-source image on the detector. The detector position was then adjusted until the point-source appeared smallest and sharpest on the live capture display (Figure 5.11).

After panchromatic focusing, the beam splitter was removed to allow direct access to the spectrograph entrance slit. The Hg-Ar source was again used for illumination during the following steps:

1. Collimator adjustment: The variable-length tube was adjusted to change the separation between the collimating lenses while monitoring the hyperspectral detector output.
2. Horizontal line reference: A high-contrast horizontal line (marker on white paper, visible in Figure 5.12) was placed at the object plane; the collimator was adjusted back and forth through the block collar until the line edge was sharp.

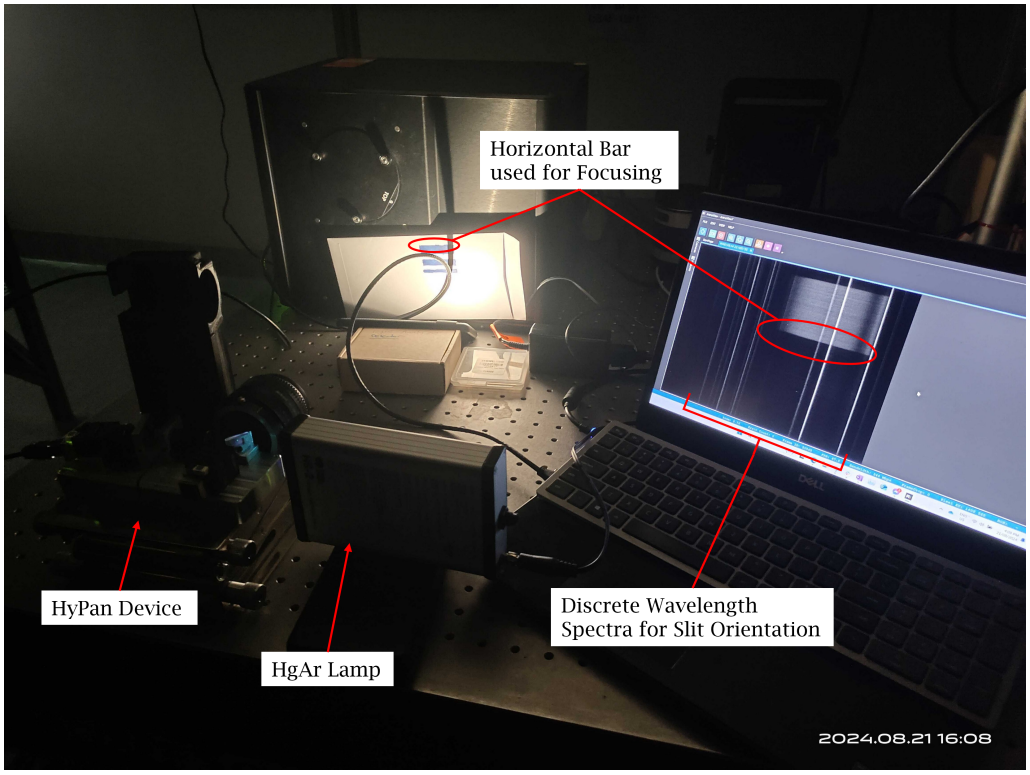

Figure 5.12: Spectrometer focusing with an Hg-Ar arc lamp and torch-lit dark line camera target. The horizontal marker line was used to focus the collimator-slit unit; position adjustment was altered back and forth through the grating-block holding bracket. Wavelength spectra were used to verify vertical position of the entrance slit.

3. Slit rotation check: The slit image was overlapped by the HgAr lamp, and its vertical orientation was adjusted by rotating the collimator tube within its bore before locking with the grub screw.

Wavelength calibration

Wavelength calibration maps detector columns to physical wavelengths so that spectral features are correctly identified. Inaccurate mapping shifts diagnostic lines, degrading material classification and any downstream quantitative analysis. We followed the OpenHSI calibration workflow [25], an open-source procedure designed to guide users from raw emission line captures to a fully parameterised wavelength model. The workflow provides tools for automated peak detection with verification with polynomial fitting, and outputs calibration files directly usable in later capture and processing.

For the calibration source, we used the same Hg-Ar lamp (Ocean Insight HG-2) positioned directly in line with the spectrometer slit as shown in Figure 5.13. The Hg-Ar lamp produces discrete emission lines at well-defined wavelengths spanning the visible and near-infrared range. The subset of lines used for fitting is listed in Table 5.2, chosen to give strong, isolated peaks distributed across the operational range. At the red end, the spectrum may be subject to contamination from second-order diffraction of blue wavelengths, as a long-pass filter was not used.

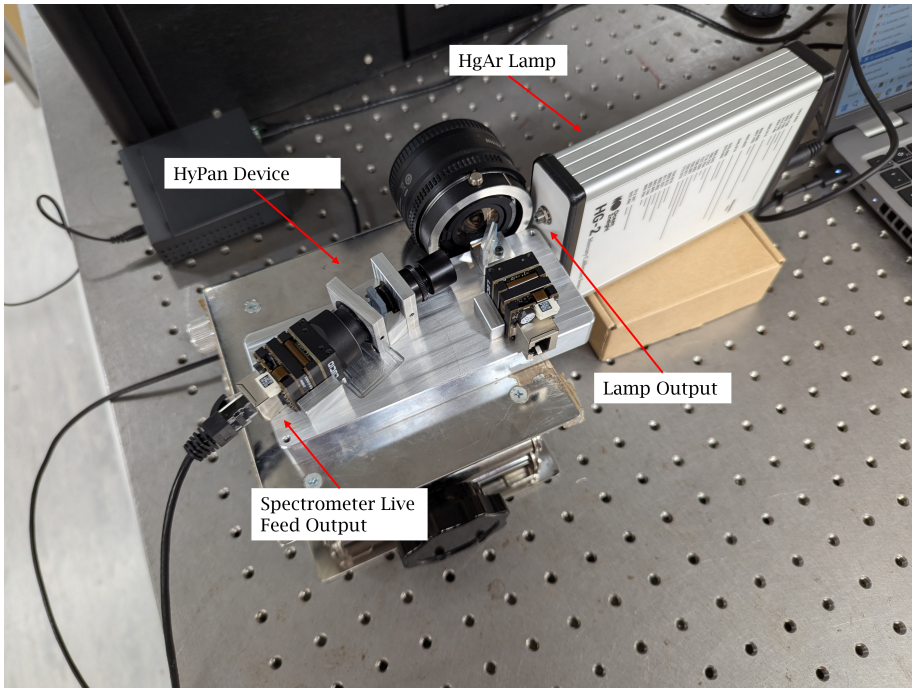

Figure 5.13: Device set-up for wavelength calibration using the HgAr lamp. Discrete emission lines from the lamp are directed through the spectrometer to calibrate the spectral axis of the detector.

Table 5.2: Hg-Ar emission lines used for wavelength calibration. Wavelengths in nm.

253.652	404.656	696.543	763.511	842.465
296.728	407.783	706.722	772.376	852.144
302.150	435.833	714.704	794.818	866.794
313.155	546.074	727.294	800.616	912.297
334.148	576.960	738.398	811.531	922.450
365.015	579.066	750.387	826.452	

Calibration data was acquired with 250 ms integration time and a gain setting of 10. These parameters were chosen to maximise line intensity without saturating the detector (75% of maximum pixel brightness).

The calibration window was initially set from 430–900 nm, capturing the strongest lines while avoiding sensor edge effects. A full spectrum was captured, after which the OpenHSI calibration routine automatically identified the four most intense peaks, used them to estimate the wavelength scale, and matched them against the known line list. Manual confirmation was used to verify peak IDs at 546.96, 435.833, 579.513, and 763.511 nm and a response curve was fitted to the emission spectrum in Figure 5.14. The initial set established the image scale and defined the spectral window (Figure 5.15a).

Additional lines were then manually confirmed, extending the fit to twelve peaks across the range (Figure 5.15b). Fit quality was quantified from the calibration parameters (`cam_settings_Mono8_bin1.pkl`). A linear model of wavelength vs. pixel achieved $R^2 = 0.9999945$ with an RMS residual of 0.35 nm, while a quadratic

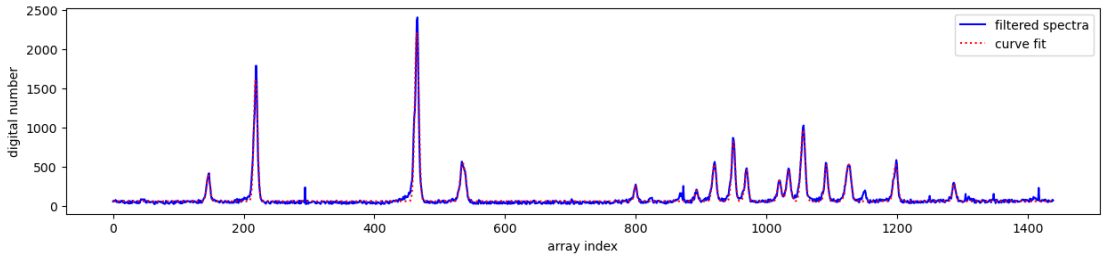

Figure 5.14: Curve-fitted emission spectrum of the wavelength calibration image, pulled from a cross-section of the spectrometer detector. This curve-fit is then used to set the window and pixel-binning for datacube capture.

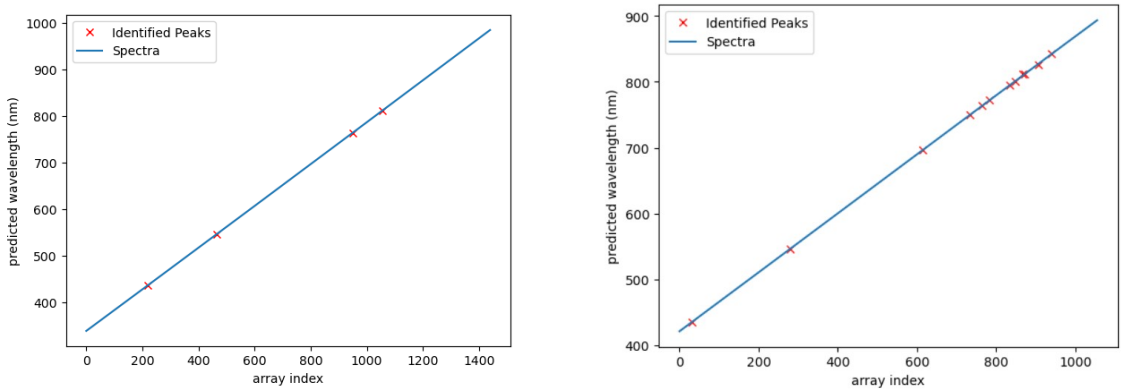

(a) Preliminary wavelength peak identification.

(b) Secondary confirmation with comprehensive peak identificaition.

Figure 5.15: 2-Stage quadratic calibration curve production relating pixel index to wavelength.

model improved to $R^2 = 0.9999994$ with an RMS residual of 0.11 nm. The quadratic model was thus adopted for the final mapping (later linearised during resampling for convenience). The calibration curve is shown in Figure 5.15.

As part of the calibration, smile distortion was also corrected. Smile distortion is the curvature of spectral lines across the spatial axis, which can introduce wavelength errors if uncorrected. This shift is compensated for by "flattening" the emission lines produced by a known source into vertical lines and using this shift as the standard for detector image alteration. Analysis of the calibration metadata indicated that this spectral curvature resulted in pixel shifts ranging from 4 to 7 pixels across the detector array. In the OpenHSI pipeline, this correction is implemented by applying a pre-computed index shift to each column of the raw sensor data, realigning the spectra before any downstream processing occurs. Figure 5.16 shows the effect of the correction: in the raw (pre-correction) image, emission lines curve downward toward the edges of the slit; in the corrected image, they are straightened, ensuring that wavelength assignments remain constant across all spatial positions. Keystone distortion (the variation of magnification with wavelength) was not digitally corrected in this processing pipeline, as the current OpenHSI framework is currently limited to include only simple smile correction to compromise complexity.

The OpenHSI calibration process produces two output files: a `.json` containing the pixel offset, calibration window limits, and spectral resolution, and a `.pkl` file

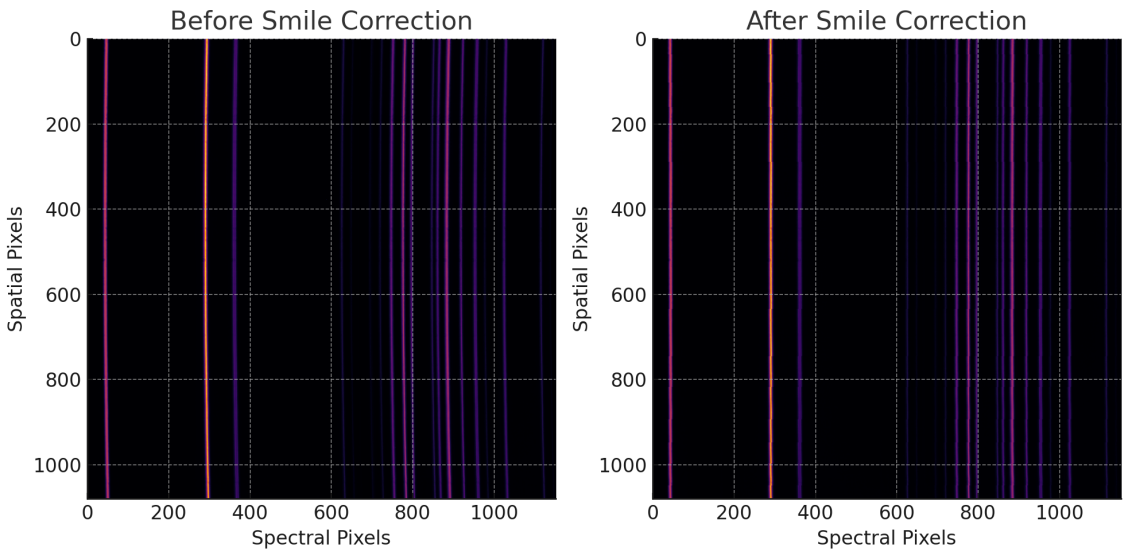

Figure 5.16: Smile distortion correction: pre-correction (left) shows curvature of spectral lines toward the edges; post-correction (right) shows straightened lines after polynomial spatial adjustment.

storing the wavelength assigned to each detector column and the spatial polynomial for smile correction. In the current OpenHSI version, `.nc` files replace `.pkl`, though the stored parameters are equivalent. These files are used directly in subsequent processing steps, including the binning stage, where the quadratic calibration is resampled to a linear wavelength scale for convenience. The final operable spectral range of the HyPAN system, set by the combined grating, detector, and optical path design, is 416–920 nm, covering the visible spectrum and part of the NIR region.

Radiance Calibration

Digital Numbers (DN), or raw detector counts, represent the raw output of the hyperspectral imaging detector by quantifying the number of electrons generated in each pixel, scaled by the sensor's electronic gain. While DN values provide a direct measure of detector response, they lack physical units and vary across devices due to differences in gain, quantum efficiency (QE), and other optical factors. For quantitative analysis, DN must be converted into spectral radiance $L(\lambda)$, typically expressed in $\mu\mathrm{W/cm^2/sr/nm}$, using a wavelength-dependent calibration factor $g(\lambda)$:

$$L(\lambda) = g(\lambda)\,[DN(\lambda) - DN_{\mathrm{dark}}(\lambda)] \tag{5.3}$$

Here, $DN_{\mathrm{dark}}(\lambda)$ is obtained from dark frames acquired with the lens capped, accounting for thermal and electronic noise (dark current). The calibration factor incorporates the combined optical throughput of the system, including detector QE, grating efficiency, and lens transmission, and is derived by comparison with a reference light source of known spectral radiance.

Calibration was performed using a Labsphere Spectra-CT Power Color tunable integrating sphere (CT-1000-S). This device produces stable, spectrally programmable output across the visible range. Luminance settings of 0, 1000, 2000, 4000, 8000,

10000, and 20000 were used, each measured at integration times of 0, 15, 30, 100, and 150 ms. This covered the full dynamic range from low-light laboratory conditions to typical midday sunlight levels (approximately 10^4–10^5 cd/m^2). Figure 5.17 shows example raw detector images at maximum integration time for each luminance setting.

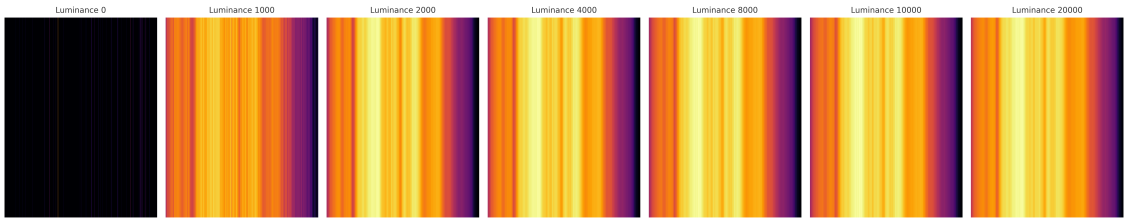

Figure 5.17: Radiance calibration raw detector outputs for each luminance setting at maximum integration time (150 ms). The variation in pixel intensity across the scene reflects the combined spectral output of the source and system response.

The calibration procedure followed the `openhsi` radiometric workflow [25]. For each wavelength channel, the measured DN values were compared to the known spectral radiance from the integrating sphere. The slope of this relationship provided $g(\lambda)$, establishing the mapping from DN to absolute radiance. Flat-field correction was applied throughout this process, as the calibration factor is determined per pixel, normalising pixel-to-pixel responsivity variations. The resulting calibration curve is stored as a set of wavelength-indexed scale factors in a `.json` file, which is automatically applied to all subsequent captures within the `openhsi` pipeline. This radiance calibration ensures that subsequent hyperspectral datacubes are physically meaningful and directly comparable between sessions, instruments, or environmental conditions. By covering a broad range of luminance and exposure settings, the procedure captures the non-linearities in detector response and allows accurate conversion of DN to radiance under both dim laboratory illumination and full-sunlight field conditions.

5.3 Spectrometer Performance

The spectrometer's performance was assessed through capture trials designed to evaluate its ability to generate high-quality hyperspectral datacubes under varied conditions. Two optical configurations, here referred to as Model 1 and Model 2, were tested to explore both long-range and controlled close-range performance. These trials established baseline spatial and spectral fidelity prior to pansharpening, providing a reference for later improvements.

The capture process was initially managed using the OpenHSI Python library, which communicates with the detector API through Jupyter notebook scripts. This interface provided control over exposure settings, bit depth, and wavelength binning, with data stored as sequential frames subsequently compiled into NetCDF4 hyperspectral cubes. However, under high-illumination conditions the Python-based workflow proved limited, as shorter exposure times and higher frame rates strained the available bitrate. To overcome this, frames were instead captured directly using

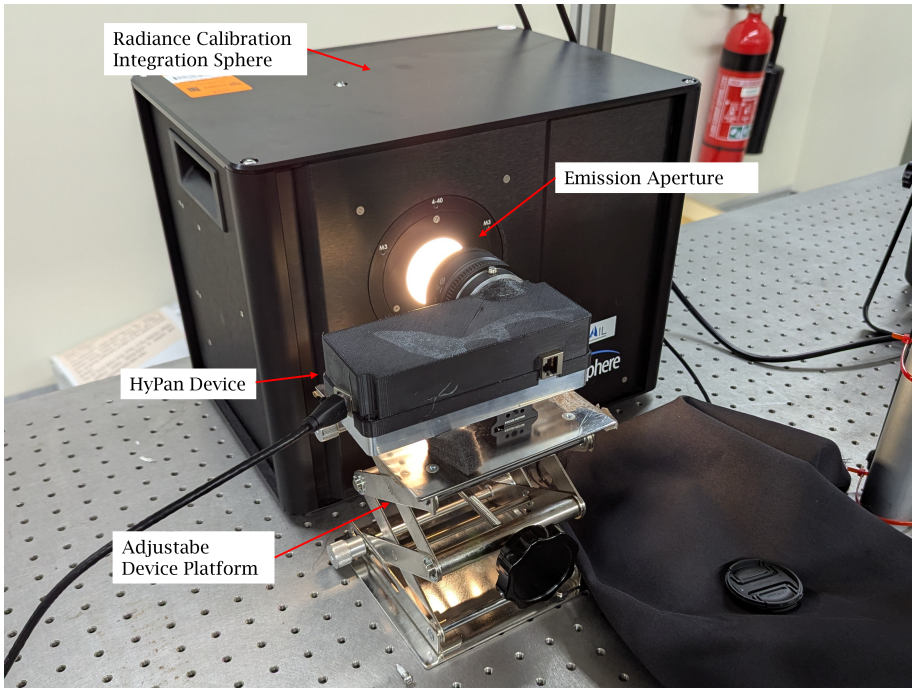

Figure 5.18: Radiance calibration setup procedure showing the device aligned with the emission aperture of the LabSphere calibrating lamp. The integrating sphere was cycled through chosen luminances, while the HyPan device cycled through 5 exposure times to gather a range of calibration points.

the LUCID Vision Labs ArenaSDK software and later compiled into datacubes via a custom Python script detailed in 6. This ensured consistent frame timing without skips and allowed calibration settings to be integrated into post-processing.

Model 1: Early Capture Trials

The first design, incorporating the Opteka 500 mm f/6.3 lens, was evaluated by targeting distant outdoor scenes at approximately 100–150 m. This configuration demonstrated the system's ability to acquire hyperspectral cubes at long range, but lacked standardisation in target characteristics, making it unsuitable for quantitative performance evaluation. In particular, the absence of a calibration target prevented contrast analysis, and environmental variability further reduced reproducibility. While useful as an exploratory test, these captures were limited to qualitative demonstrations.

Model 3: Controlled Capture and Quantitative Analysis

To obtain reproducible data for system characterisation, the spectrometer was reconfigured with a Nikon 50 mm f/1.8 lens for close-range captures. A USAF 1951 resolution target (Glass plate printed with contrast bar image shown in Figure 5.21a) was positioned at 60 cm, with a Spectralon reflectance standard (99%) as a background to enable reflectance calibration. Captures were performed in direct sunlight with the capture setup shown in Figure 5.20. While laboratory sources offer greater control, the available sources were found to limit the illuminated field of view. Sunlight on a clear day provided a practical balance, offering spatial uniformity across

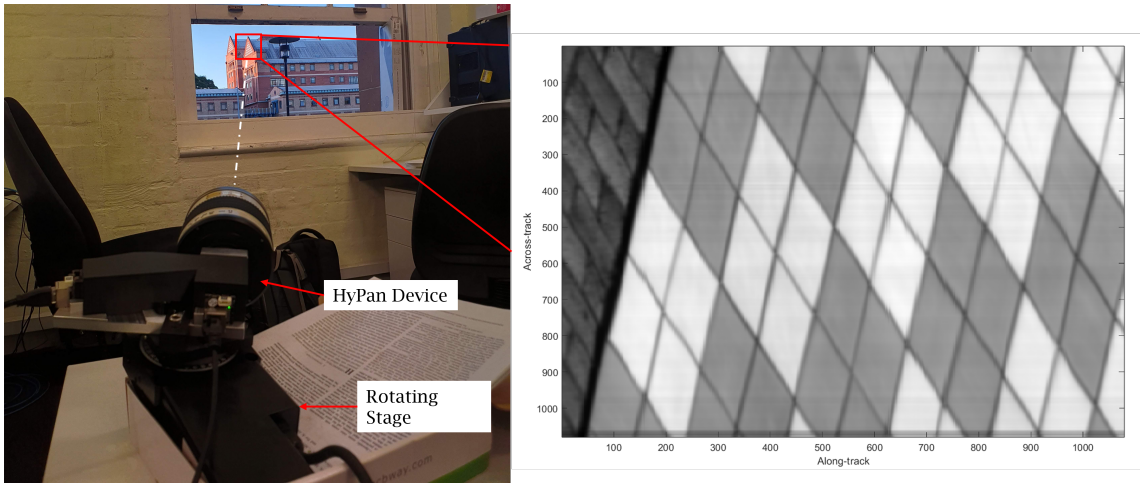

Figure 5.19: Model 2 long-distance capture setup showing a checkerboard pattern on a nearby building. This dataset was taken as an early model validation of efficacy.

the imaging target and the high intensity required for contrast measurement. A motorised rotation stage was employed to scan the target, with scan speed matched to the instantaneous field of view (iFOV) and exposure time to ensure continuous sampling. The iFOV is given by

$$\text{iFOV} = 2\tan^{-1}\left(\frac{w_{\text{slit}}}{2f_{\text{tel}}}\right), \tag{5.4}$$

where w_{slit} is the slit width and f_{tel} the focal length of the objective lens. For the 50 mm lens, the iFOV was 0.0229°, and an exposure time of 17 ms was selected by adjusting until the brightest pixels reached approximately 75% of the detector's maximum digital number. This yielded a frame rate of 58.8 Hz, corresponding to a rotational scan rate of 1.35°/s, ensuring near-contiguous spatial sampling without overlap.

The USAF target image capture was a core component of the validation of the HyPan device. By examining the reflectance difference between bright and dark points between the horizontal and vertical bars, an MTF curve was plotted for each wavelength slice of the datacube. The wavelength-averaged spatial image of the target is shown in Figure 5.21b. This data was then benchmarked against the same curve for the datacube after applying the pansharpening pipeline, to verify the enhancement achieved through data fusion across the wavelength range. Additionally, this data is useful in assessing the reduction in anisotropy, by comparing the data for vertical and horizontal line pairs across the same process.

Field Capture: Natural Scene

To complement target-based measurements, a scene comprising a sandstone building with surrounding foliage at the University of Sydney was captured using the Nikon lens focused at infinity, shown in Figure 5.22. This provided a test case for system performance on complex, natural structures at distances of approximately

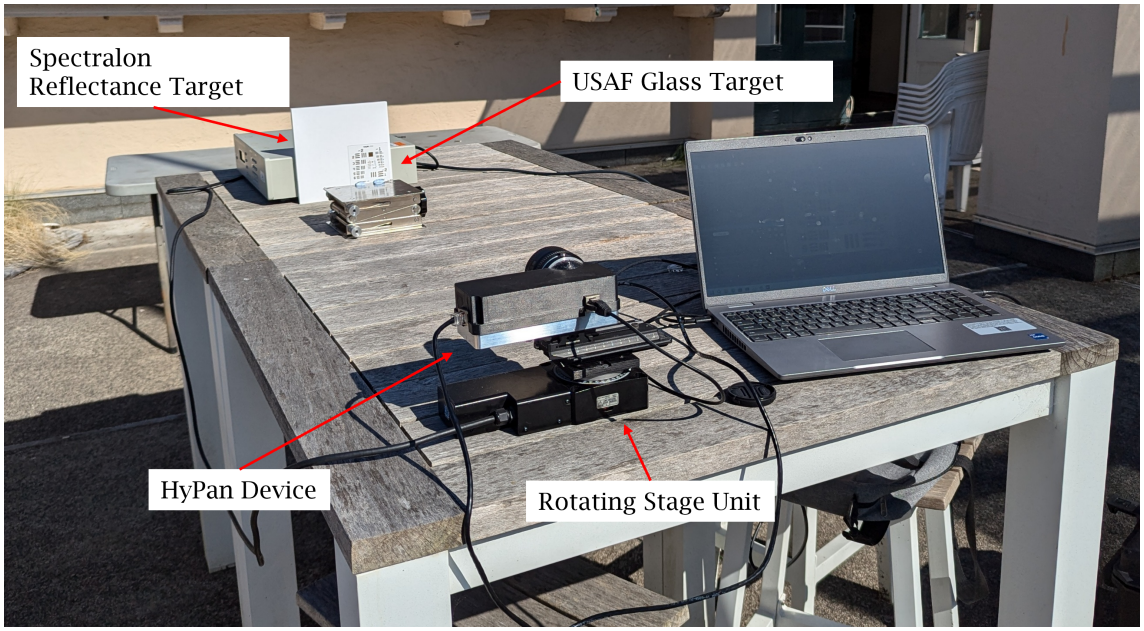

Figure 5.20: USAF contrast target capture setup; the HyPan device was mounted on a speed-tuned rotating stage while a live feed of the spectrometer detector was captured. A Spectralon reflectance target was used as the background of the image for reflectance-adjusted data in post-processing.

200 m. The capture demonstrated the anisotropic sampling directly: tree foliage appeared blurred in the along-track direction, while architectural features showed higher clarity across-track. These results illustrate the limitations of the unsharpened datacube and motivate the application of pansharpening for balancing spatial fidelity.

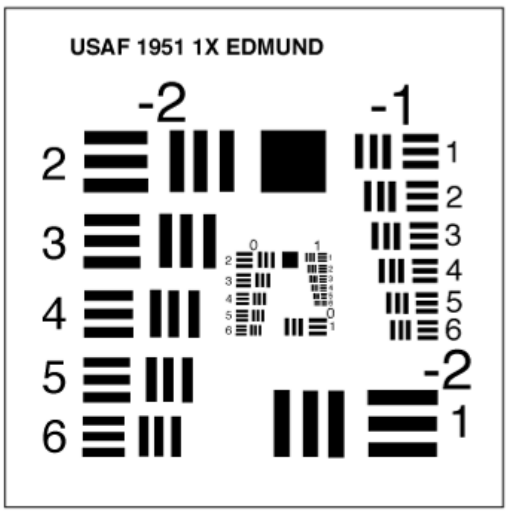

(a) USAF 1951 resolution target.

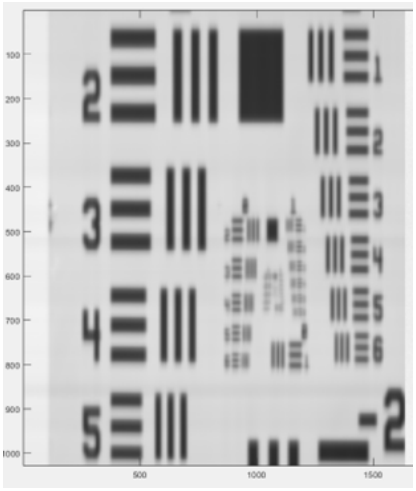

(b) Raw datacube capture of 1951 USAF target.

Figure 5.21: The ideal image (a.) and raw capture (b.) of the USAF 1951 target. The imaging target was a 3x3 inch glass plate, printed with the contrast target; a series of dark lines of descending spacing.

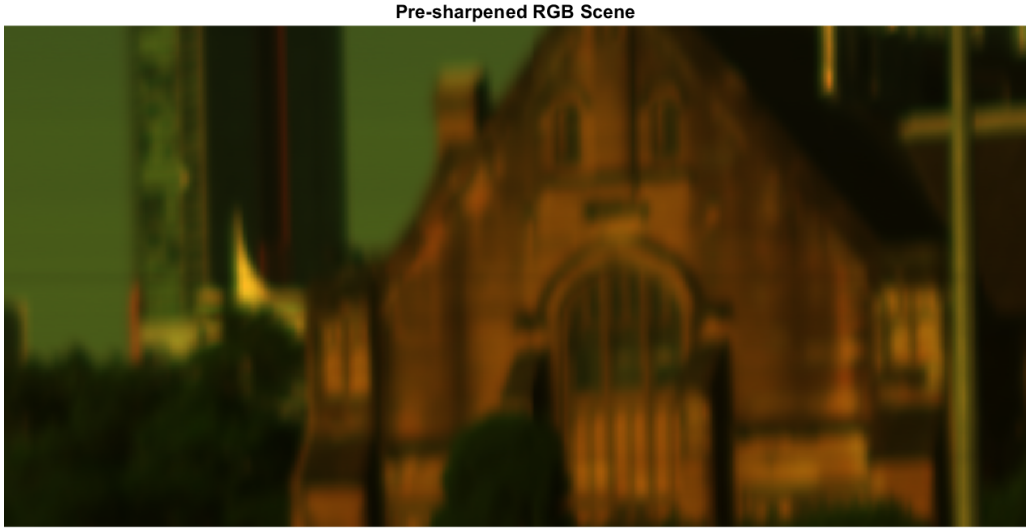

Figure 5.22: RGB-adjusted capture of a building, surrounding foliage and sky for evaluation of spatial scene enhancement in pansharpening process.

Chapter 6

GSA Pansharpening and Evaluation

6.1 Introduction

Building upon the raw spectrometer performance established in Chapter 2, this chapter addresses the challenge of enhancing the spatial resolution of hyperspectral datacubes produced by the HyPan device. While pansharpening methods are well established in satellite remote sensing, their use in ground-based and UAV platforms introduces additional complications, including spatial alignment, variable illumination, and the lack of specific third-party datasets. To prepare the data for fusion, a new compilation workflow was implemented, combining direct image acquisition with a virtual camera interface in the OpenHSI software, and a manual image co-registration-cropping stage to align the hyperspectral and panchromatic datasets.

The analysis presented here evaluates the sharpened results through both quantitative metrics (modulation transfer function, spectral similarity, and task-oriented indices) and qualitative scene comparisons. The focus is on resolving the anisotropy inherent in pushbroom hyperspectral systems, where along-track resolution is determined by platform motion and exposure timing, while across-track resolution is fixed by detector pixel pitch. In HyPan, as in similar slit-based designs such as OpenHSI, this results in rectangular pixels elongated in the flight direction, limiting the system's ability to resolve fine detail. Where the along-track dimension of a hyperspectral datacube such as Figure 6.11 may have 227 image slices captured, by fusing with the higher-density panchromatic frame (958 pixels in the same dimension), this imbalance can be reduced, improving the interpretability of small features. Later sections quantify these effects, while the following work provides an overview of the pipeline used to prepare data for sharpening.

6.2 Data Preparation

6.2.1 Datacube compilation

During initial testing, a limitation was identified in the use of the OpenHSI Python control scripts for high-light acquisitions. When the python scripts communicated

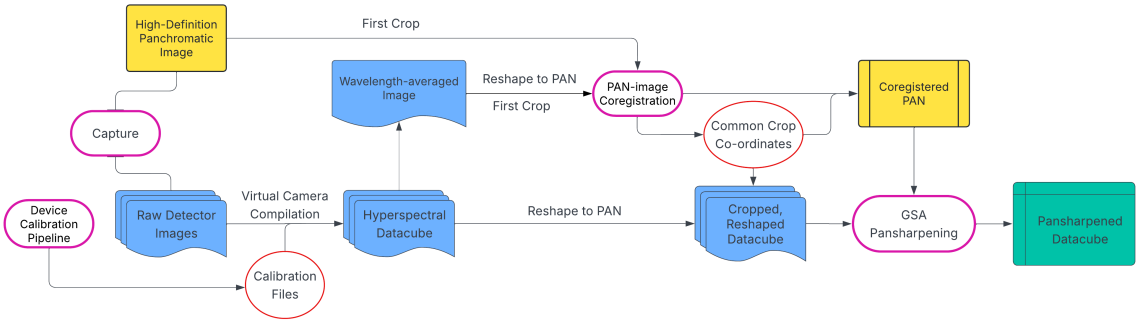

Figure 6.1: Flowchart of data processing pipeline.

directly with the camera API, frame downloads lagged behind exposure timing, leading to missed frames and gaps in capture at short integration times. This problem prevented stable operation at the fast scan rates required for outdoor datasets with ample sunlight.

To circumvent this bottleneck, image slices were acquired directly using the manufacturer's ArenaView API. This approach bypassed the Python layer, allowing stable operation exposures of 17ms and below, and a capture frequency of 58 Hz, rates not achievable with the OpenHSI capture scripts. Exposure times were selected such that the brightest clearly resolved feature reached approximately 75% of the detector's maximum DN (digital number - raw pixel intensity). This practice balances signal-to-noise optimisation with the need to prevent saturation. Frames were saved as uncompressed TIFFs to prevent compression artefacts. These frames are chronologically ordered in their save folder by timestamps in the filename.

To retain compatibility with the OpenHSI calibration files and follow-on image processing pipeline, a virtual camera interface was written to compile the uncompressed TIFF files into a standard netCDF4 datacube. To do this, the script was written as an alternative device class "FileCamera" as shown in Figure 6.2. At initialisation the class establishes the file location and recognises the files inside, before loading the camera settings stored in calibration files for the HyPan device. In existing device classes in the OpenHSI repository, the get_img command directs the connected device to take a capture from the detector plane, and move to the next. In the FileCamera script, this command was altered to pull the earliest captured TIFF file in the folder, apply the windowing settings from the calibration file, crop adhering to these settings and then flip the captured data across left-to-right. This flip was a leftover alteration as part of the calibration process. The script then moves to the next produced frame and performs this across all files in the folder, saving each across a single dimension of a data array. This command is driven by the cam.collect() inherent in the OpenHSI pipeline, through which smile correction and DN-to-radiance conversion can be pulled from the calibration pkl file. Further processing such as wavelength binning and range calibration can also be applied in this collection step. After compilation, the datacube is then saved through the cam.save function which deposits the data in a netCDF4 file for use in the following data preparation pipeline.

```python
class FileCamera(OpenHSI):
    """
    A camera class that reads data from a set of files.

    Args:
        filepaths (list): A list of filepaths to read data from.
        n_lines (int): Number of lines to simulate. Defaults to the number of files.
        **kwargs: Keyword arguments to be passed to the parent class.
    """
    def __init__(self, directory, settings_file, **kwargs):
        super().__init__(**kwargs)
        # Get a list of all filepaths in the directory
        self.filepaths = [os.path.join(directory, f) for f in os.listdir(directory) if f.endswith('.tiff')]
        self.filepaths.sort()  # Optional: Sort the files if order matters
        self.n_lines = self.n_lines if self.n_lines is not None else len(self.filepaths)
        self.current_frame = 0

        # Load camera settings from the JSON file
        with open(settings_file, 'r') as f:
            settings = json.load(f)

        # Extract windowing settings
        self.win_offset = tuple(settings["win_offset"])  # (row_offset, col_offset)
        self.win_resolution = tuple(settings["win_resolution"])  # (height, width)

    def start_cam(self):
        """Starts the camera (no action needed for file reading)."""
        pass

    def stop_cam(self):
        """Stops the camera (no action needed for file reading)."""
        pass

    def get_img(self):
        """
        Gets the next image from the file list.

        Returns:
            ndarray: The image data.
        """
        if self.current_frame < len(self.filepaths):
            # print(f"Processing file {self.current_frame + 1}/{len(self.filepaths)}")
            data = Image.open(self.filepaths[self.current_frame]).convert('L')
            data_array = np.array(data)

            # Apply windowing (cropping the image)
            row_start, col_start = self.win_offset
            row_end = row_start + self.win_resolution[0]
            col_end = col_start + self.win_resolution[1]

            # Crop the image to the windowed region
            windowed_data = data_array[row_start:row_end, col_start:col_end]

            #Flip LR
            flipped_data = np.fliplr(windowed_data)

            self.current_frame += 1
            return flipped_data
        else:
            raise StopIteration("All files have been read.")
```

Figure 6.2: Virtual camera interface code written to compile TIFF files from direct ArenaView capture

6.2.2 Cropping and Normalisation

Preparation of the hyperspectral and panchromatic data required a structured preprocessing workflow to ensure both spatial and spectral alignment prior to pansharpening. To reflect the physical sampling of several detector pixels across the slit and reduce computational demands, the 1152 spectral columns of the windowed datacube were averaged into 130 bins of approximately 4 nm. This binning reduced RAM requirements from over 100 GB to roughly 10 GB for full-cube pansharpening, making the data manageable for downstream analysis. This processing was conducted using the OpenHSI post-processing package, alongside wavelength and radiance calibration of the data, and smile correction.

Following calibration, the datacubes were imported into MATLAB for additional refinement. Spatial binning was applied along the vertical (spatial y) axis at a 2:1 ratio. While this reduced input file size (approx. 440 MB to 220 MB) and data-fusion RAM requirements, the primary motivation was to establish a lower-resolution spatial baseline to more easily judge the impact of the pansharpening process.

Where available, a reflectance target was incorporated into the scene to normalise radiance values. A fixed 5×5 pixel region on the target was averaged to derive a reference radiance spectrum. The entire datacube was then divided by this reference, effectively setting the target's reflectance to unity (1.0) across all bands. For rigorous reflectance data retrieval and future work, it is recommended to scale this reference by the panel's wavelength-dependent calibration coefficients $C(\lambda)$. However, for this research, the panel was treated as a perfect reflector with a flat unity response. While the Spectralon puck used is not a perfect Lambertian reflector and has a nominal reflectance of approximately 99%, this first-order approximation was adopted for consistency across captures and was deemed sufficient for validating relative spatial contrast. In scenes without a target, the cubes were retained in radiance units, with calibration performed using the procedures described in Chapter 5.

Optical corrections were then applied to account for vignetting and throughput variation. A flat-field calibration frame was acquired by imaging a LabSphere uniform radiance source (model CT-1000-S, operated under 1000 cd/m^2 at 350μs exposure) and dividing the raw panchromatic image by this reference. This correction accounted for systematic variations across the field, including field lens vignetting, beamsplitter transmission differences, and detector response variation.

6.2.3 Coregistration

Following radiometric and optical correction, the hyperspectral and panchromatic datasets were spatially aligned through cropping, feature matching, and interpolation. To begin this process, a representative image of the datacube was created (averaged across all wavelength bins) and the panchromatic image would be registered to this in the two spatial dimensions. Because the pushbroom hyperspectral scan produced additional scene content in the along-track direction (set by scan duration) and less coverage across-track (set by the spectrometer field of view), both images were first manually cropped to their region of overlap. This ensured a common spatial domain before registration. As the datacube along-track dimension is

significantly shorter than its across-track, this image was then interpolated to create a static reference with the same shape (y:x ratio) as the panchromatic dataset. This step was required for the coregistration application toolbox in the MATLAB Image Registration package.

Although the two detectors share the front lens and beam splitter optics (Section 5.1.3), software-based registration was chosen for image-to-cube alignment. The split optical paths introduce slight disparities, primarily due to the inherent magnification factor of the spectrometer relay optics and micron-level offsets in sensor positioning. Consequently, feature-based matching was used to resolve these affine transformations to sub-pixel accuracy.

Registration was carried out using MATLAB's Registration Viewer application, which provides feature-based methods including Speeded-Up Robust Features (SURF) [115], Oriented FAST and Rotated BRIEF (ORB) [116], and KAZE [117]. SURF is a widely used detector that identifies features by approximating Gaussian smoothing, making it robust to scale changes but susceptible to blurring sharp details. ORB is an efficient alternative designed for high-speed processing, using binary descriptors to match keypoints quickly. KAZE differs from these by employing non-linear filtering; rather than blurring the image uniformly, it adapts locally to smooth noise while preserving distinct object boundaries. Consequently, KAZE was selected as the primary method, as it provided the most stable match density and spatial accuracy across these contrasting domains. Registration was refined by adjusting the number and quality of feature matches until the fused magenta-green overlays (Figure 6.3) showed consistent alignment across vegetation and built structures. In Figure 6.3, the matched features do not necessarily correspond to high-contrast corners. This is a result of the KAZE algorithm, which prioritises stable regions of texture and contrast over sharp geometric edges. This method allows for effective matching within the complex and repetitive textures of foliage where distinct corners are often missing.

The transformation model applied was affine, because it preserves straight lines and parallelism, which are critical for maintaining the geometric integrity of the slit-imaged hyperspectral data. Higher-order models such as polynomial warps were tested but introduced distortions. Conversely, rigid transformations, which are restricted to rotation and translation, were insufficient as they could not account for subtle differences in aspect ratio, resulting in fewer matched regions.

Registration accuracy was quantified by residual keypoint error and image similarity. For the building-vegetation scene, the mean alignment error was 0.57 pixels (RMS = 0.64, P95 = 1.00), confirming sub-pixel correspondence across modalities. Structural similarity between the panchromatic and band-averaged hyperspectral images reached Structural Similarity Index Measure (SSIM) = 0.815 (full frame) and 0.852 (overlap only). These values are consistent with the sub-pixel registration accuracy generally considered sufficient for pansharpening and fusion tasks in remote sensing [30]. Typical registration runtime was under 10 s on a standard workstation (AMD Ryzen 9, 16 GB RAM) once features were identified.

Following registration, the cropping and interpolation parameters were applied uniformly across the full datacube. The panchromatic image was then resampled with a slight adjustment to accommodate the new data shape, ensuring that the image

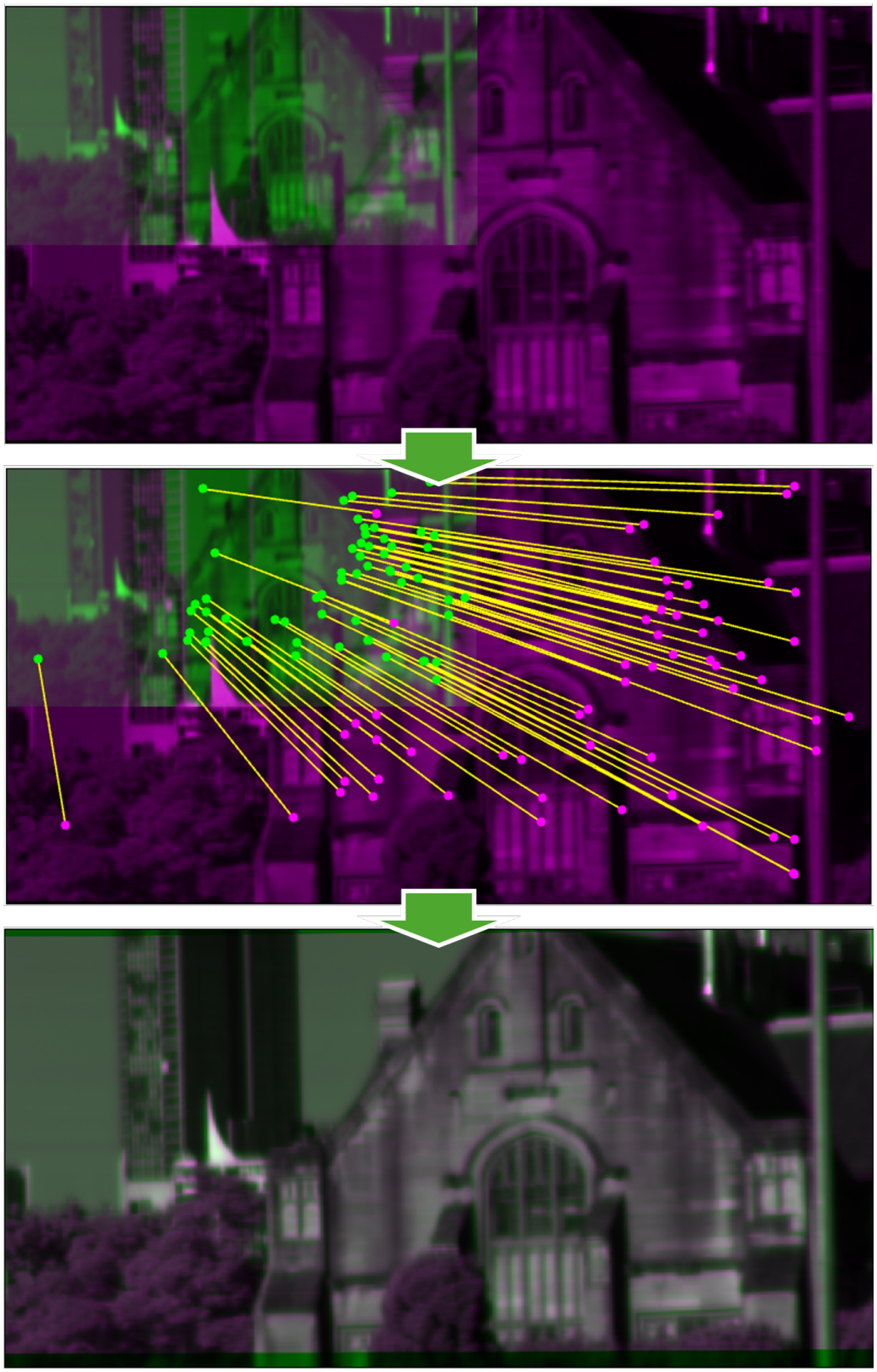

Figure 6.3: The coregistration pipeline showing pre-registration overlay (top), feature recognition between datasets showing 68 matched areas (middle) and the final green-magenta overlay after registration.

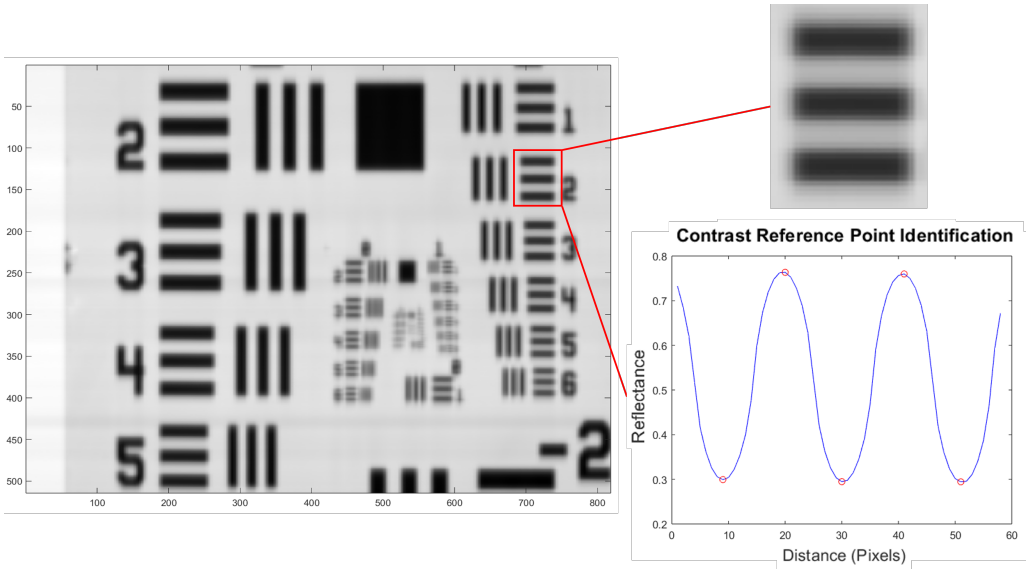

Figure 6.4: The process of local maxima and minima identification is shown here by examining the cross-section of bar-groups from the datacube image.

is exactly twice the spatial resolution of the hyperspectral data. This step is a strict requirement of the Gram-Schmidt Adaptive (GSA) pipeline used in this study, which mandates an integer resolution ratio between modalities to ensure precise pixel alignment during the fusion process. Upscaling was performed using a Finite Impulse Response (FIR) filter, specifically the `interptap23` function. These filters operate by convolving the input signal with a finite set of coefficients, such as a windowed sinc function, to reconstruct intermediate values [118]. This approach is preferred over simple linear interpolation as it preserves high-frequency spatial detail while suppressing aliasing artifacts [119]. Polyphase FIR implementations rely on a fixed number of neighbouring pixels (taps) to generate new samples, using an integer ratio ensures consistent pixel alignment and prevents sub-pixel shifting errors that would otherwise degrade the spatial integrity of the fused datacube. From here, the GSA algorithm was run to inject the datacube with the higher contrast and resolution spatial information.

6.3 Result Processing and Evaluation

6.3.1 Quantitative Evaluation of Spatial Resolution Enhancement

MTF Analysis and Results

The USAF 1951 target acquisition enabled quantitative assessment of spatial resolution via modulation transfer function (MTF) analysis. The datacubes were imported into MATLAB where bar groups were manually identified and marked out. The reflectance profiles of the cross-sections of these bar groups were then plotted against reflectance and local maxima/minima identified, shown in Figure 6.4. The difference in reflectance is then normalised to the maximum contrast difference; here taken as an area of the glass target with no features, against the centre of the dark square.

These data were used to construct MTF curves across 130, 4nm-binned spectral bands. From these curves, two primary metrics were then derived: the contrast at the highest resolvable frequency (averaged across wavelength range), and the integrated area under the curve (AUC), which captures overall contrast retention across frequencies. These metrics are introduced in 3. Wavelength-averaged spatial images of the USAF glass target can be seen in Figure 6.5 and demonstrate a visual indicator of improved contrast.

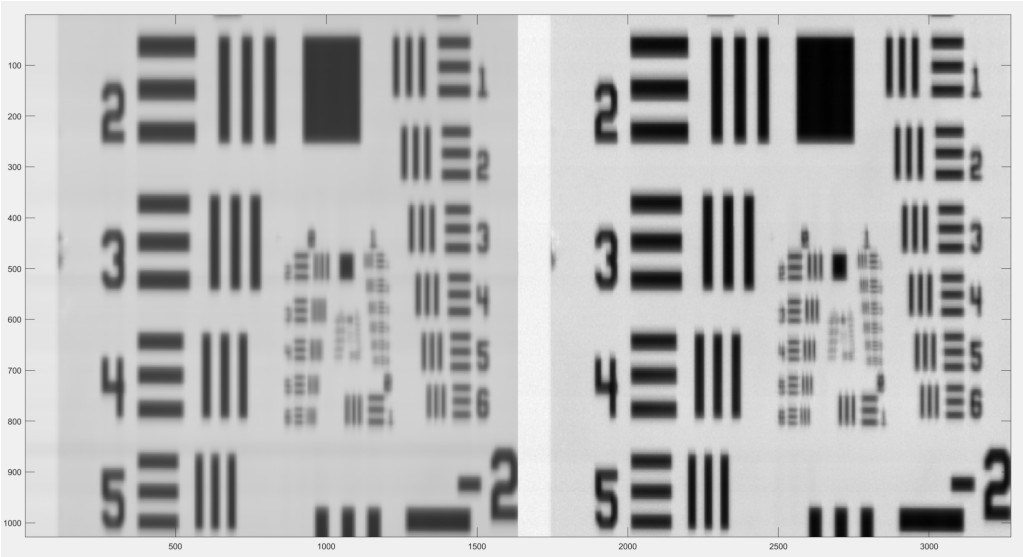

Figure 6.5: The wavelength-averaged image of the hyperspectral datacube before (left) and after (right) the pansharpening process.

MTF curves for each of the 130-binned spectral channels are presented in Figures 6.6 and 6.7. Examination of these graphs reveals an elevated MTF curve in the pansharpened datacube, especially at higher frequencies (>15 lp/mm), and a tighter dispersion across the wavelength range for more uniform spatial-spectral analysis. At the advanced metric level, the area under the curve (AUC) for the wavelength-averaged MTF increased from 0.262 before pansharpening to 0.340 after (Figure 6.8) showing a ∼30% improvement. This indicates a stronger overall contrast retention across the full spatial frequency range. Similarly, the contrast at the maximum resolvable frequency (48 lp/mm) increased from 0.0258 to 0.0472 (∼83% increase). This represents a substantial extension of the system's usable resolution range, enabling finer spatial detail to be retained in the fused data.

Wavelength-dependent analysis at a representative spatial frequency of 25.44 line pairs/mm further highlights these improvements (Figure 6.9). This spatial frequency was chosen to show fine-feature performance with near-consistent non-NaN values in both datasets. Contrast values increased across nearly all spectral regions, with important gains between 650–850 nm, corresponding to areas where signal-to-noise ratios were highest. This confirms that the fusion process not only extended the frequency at which meaningful detail could be resolved, but also improved spectral consistency in regions most relevant to vegetation and environmental monitoring applications.

Directional analysis further highlights the anisotropy inherent to the pushbroom configuration. Because across-track resolution is set by detector pixel pitch while

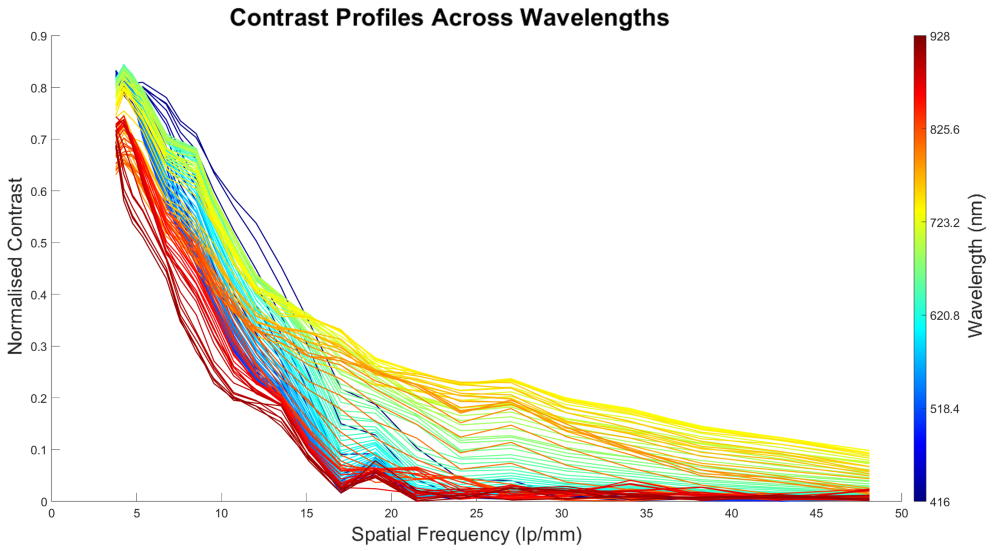

Figure 6.6: MTF results for the pre-sharpened hyperspectral datacube by 130 4nm-wavelength bins. The graph shows the rapid decline of long-wavelength spatial data and across the range at high frequencies.

along-track resolution depends on scan step size, vertical and horizontal bar groups show distinct behaviours. As shown in Fig. 6.10a, vertical line groups (corresponding to the along-track axis) exhibit an earlier fall-off in contrast, with values approaching zero at spatial frequencies > 15 lines/mm, whereas horizontal line groups retain higher contrast. The slightly higher starting contrast in vertical groups arises from a minor focusing bias toward the vertical direction during capture, visible as uneven blur in the averaged USAF image, Figure 6.5. In Figure 6.10b we can see the reduction of anisotropy in the pansharpened datacube, from the smaller dispersion between vertical and horizontal bar group MTF. This improvement in along-track resolution and blurring effect minimisation ties in to the core focus of the single-device pansharpening process, and the main success metric of this research. These quantitative metrics collectively underscore the pansharpening algorithm's effectiveness, revealing the elevation of the device's capabilities in edge contrast and more specifically along-track spatial resolution. These improvements not only expand the analytical capabilities of the system but also reinforce its functionality in precision-driven applications such as biodiversity and urban mapping, where precise spatial detail is paramount[104], [105].

6.3.2 Real Application Evaluation

Qualitative analysis of the pansharpening process when applied to more research-appropriate settings was also necessary to demonstrate the relevance of the device's real-world use. The HyPan device is targeted at small-team research applications such as UAV surveys of biodiversity and agriculture. As such the capabilites of the system in resolving spectral details in areas of foliage, and accurately identifying these areas spatially is paramount to the success of the design. The following figure (Figure 6.11) displays the averaged spatial scene of capture mentioned in chapter 5, before and after pansharpening, where the improvement in spatial contrast and

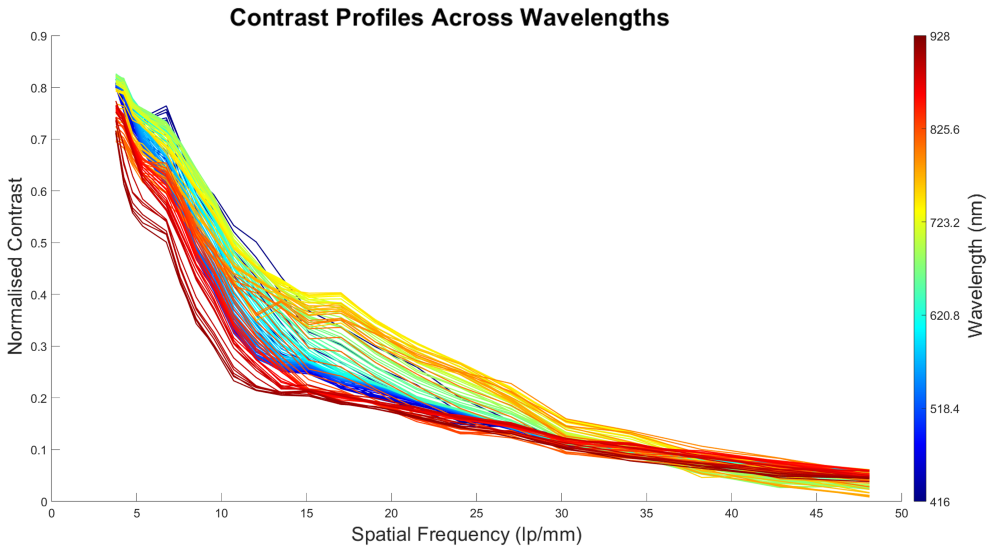

Figure 6.7: The postsharpening MTF results for each of the 4nm wavelength bins, the graph shows a marked improvement, especially in longer wavelengths, high-frequency resolution and curve spread compared to Figure 6.6.

especially finer details is shown. The areas of foliage, detailing of brickwork and structures in the distance are all more visible, and the smaller intricacies of those areas have become easily identifiable. This qualitative improvement shows at a base-level the improvement of spatial data, and allows the automatic detection of target features within the datacube frame to be gathered more reliably.

To further assess the quality of the pansharpening, the ERGAS (Erreur Relative Globale Adimensionnelle de Synthèse) metric was used. ERGAS provides a quantitative evaluation of the spectral distortion introduced during fusion by comparing the sharpened datacube to the original lower-resolution hyperspectral image. A lower ERGAS score indicates stronger preservation of spectral integrity, with scores below 10 generally considered acceptable and scores for GSA commonly found in the 6–12 range[30], [120]. The ERGAS score computed for the single-application GSA method on the HyPan dataset was **8.24**, which falls well within the range reported for standard sharpening algorithms. To ensure a fair comparison, the fused datacube was resampled to the native hyperspectral resolution following Wald's reduced-resolution protocol, which applies a smoothing step consistent with the sensor's spatial response before resizing. This ensures that both datasets are compared at the same spatial scale without introducing aliasing. This ERGAS value corroborates that the pansharpening preserved the fundamental spectral information of the hyperspectral data, while spatial contrast improvements are evidenced by MTF-based metrics and visual examination.

ERGAS was computed following Wald's reduced-resolution protocol[120], which generates a reference image by MTF-matched filtering and downsampling of the hyperspectral data. The fused image is then degraded to this same scale, allowing ERGAS to quantify spectral distortion without needing true high-resolution ground truth.

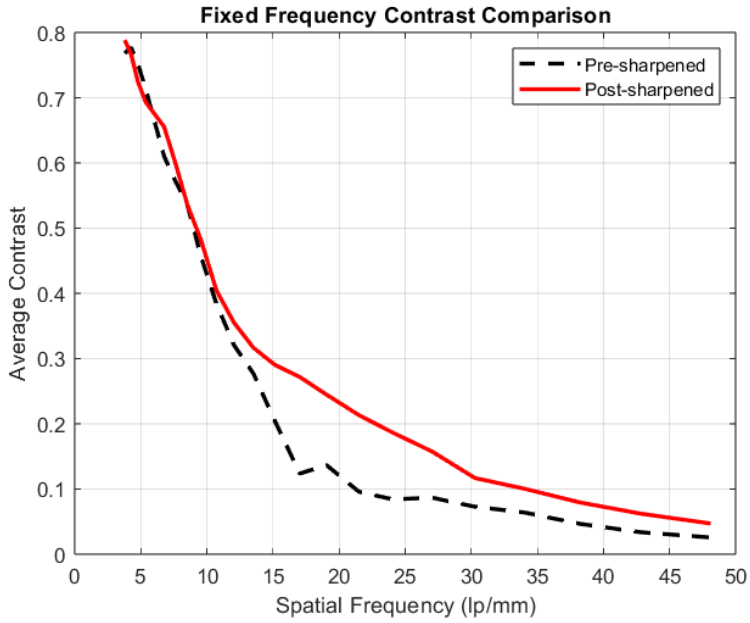

Figure 6.8: Mean contrast curves across wavelengths, comparing pre-sharpened (dashed) and pansharpened (solid) datacubes. Improvement is evident across the spatial frequency range, with higher contrast maintained at finer spatial features.

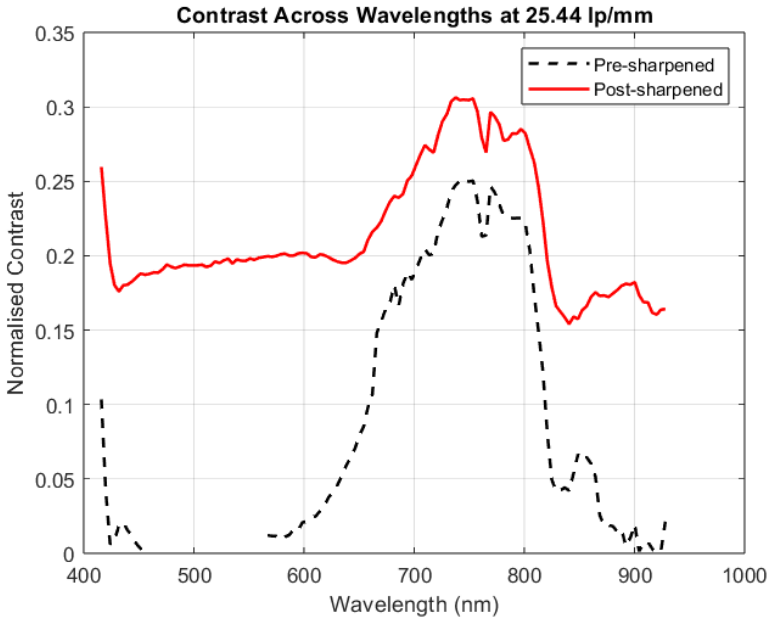

Figure 6.9: Contrast across wavelengths at 14.54 lines/mm, showing spectral dependence of resolution before and after pansharpening. Gains are consistent across the visible-NIR range, with the largest improvements observed in the red and NIR regions.

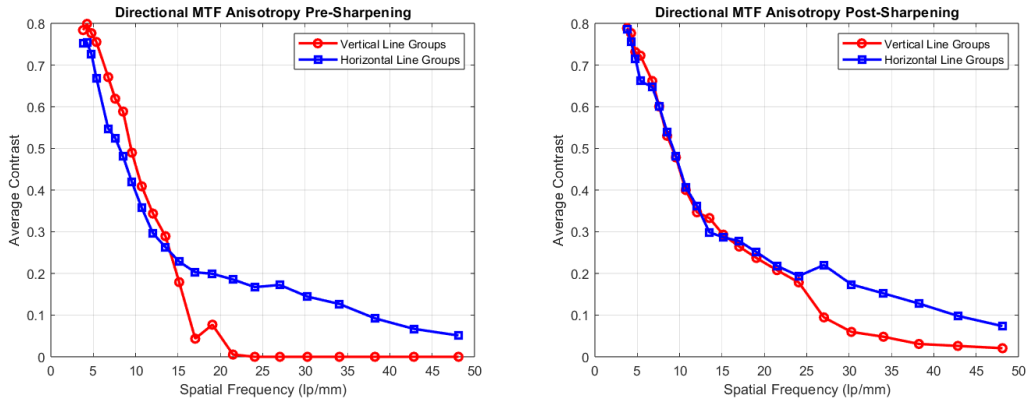

(a) Pre-sharpened MTF line-groups **(b)** Post-sharpened MTF line groups

Figure 6.10: Wavelength averaged MTF curves isolated for vertical and horizontal line groups, showing the reduction of anisotropy from the pansharpening process.

SAM Analysis for spectral preservation

To verify this preservation of spectral information, the Spectral Angle Mapper (SAM) was employed to quantitatively assess the similarity between the pre-sharpened and pansharpened datacubes. The calculated metrics yielded a mean SAM of 6.03°, with a notably lower median SAM of 1.47°, indicating that the bulk of the pixels remain spectrally consistent post-sharpening, but that some outliers significantly skew the average. Further threshold-based analysis showed that 65.8% of pixels had SAM values under 3°, and 73.5% under 5°, aligning with commonly accepted thresholds for high spectral fidelity(<5°[31]).
Interpretation of these results must be approached with nuance. In many regions, such as foliage areas, blurring in the original datacube caused spectral mixing, where a single pixel may have combined signatures from vegetation, gaps, and shadow. Following pansharpening, these areas became more spatially resolved, with distinct material signatures now appearing in different pixels. As a result, some areas exhibit larger SAM values not due to spectral distortion, but due to spatial unmixing, where the same pixel location in the sharpened image corresponds to a more spectrally specific material than in the original. This effect is most evident in the gaps between foliage clusters visible in the SAM map (Figure 6.13), which appear with elevated angle differences but reflect improved spatial and spectral discrimination. Therefore, SAM should be interpreted alongside visual and spatial metrics, as increases in angular difference may signify improved material separability rather than degraded performance. Additionally, areas of the scene in shadow where we expect low signal (building roof and lower-right of the image) lead to greater shot noise contributions and increased spectral distortion as a result. This is an acceptable compromise for the intended applications of this research, which focus on high-reflectance targets under well-lit conditions.

To validate the spectral consistency of the targeted areas of the datacube, regions of interest were selected per Figure 6.14 as part of the well-lit target scene. These regions showed strong qualitative spatial contrast improvement over the pansharpening process, and so were inspected to validate that spectral consistency was pre-

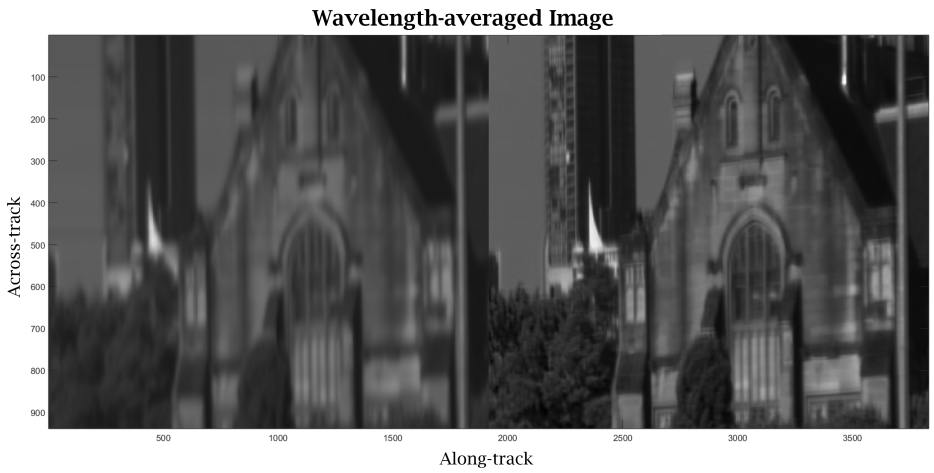

Figure 6.11: Wavelength-averaged spatial-by-spatial image representations of datacube contrast enhancement before (left) and after (right) pansharpening. Enhanced contrast is most notable in finer structures in both the building facade and vegetation.

served. Areas of intricate glass window borderings in the mid-ground and background were selected, and were found to have median SAM angles of 0.37° and 2.93° respectively, affirming the significance of contrast enhancements.

NDVI calculation

To verify this preservation of spectral data, an additional layer of evaluation was introduced through NDVI analysis. Normalised Difference Vegetation Index (NDVI) is a ratio particularly sensitive to chlorophyll content and leaf cellular structure, and is thus a widely used proxy for vegetation health. In this case, NDVI maps were generated for both the original and pansharpened datacubes. The post-sharpened NDVI map showed an increase in mean NDVI value from 0.379 to 0.402, indicating improved vegetation delineation and signal strength. The standard deviation also increased slightly from 0.135 to 0.152, suggesting enhanced spatial variability now resolved within the vegetation regions. This improvement is structurally meaningful when compared with the NDVI difference map (see Figure 6.15), where boundaries of foliage clusters and fine-scale transitions between canopy and ground become more distinct.

Importantly, these gains in NDVI and spatial clarity may partially explain observed discrepancies in SAM scores. As noted previously, certain areas within the datacube, particularly in regions of dense foliage, exhibited a notable change in spectral angle after sharpening. This is largely due to spatial unmixing: areas that were previously represented by blended pixel signatures (e.g., foliage and shadow or foliage and ground) are now more accurately separated into their constituent materials. This process inherently modifies the spectral vector per pixel, which can increase SAM values despite representing a truer spectral composition.

While the NDVI map effectively highlights regions of dense foliage, some areas within the scene are incorrectly classified as vegetation. These false positives are attributable to the presence of oxidised metal roofing, which exhibits a green hue

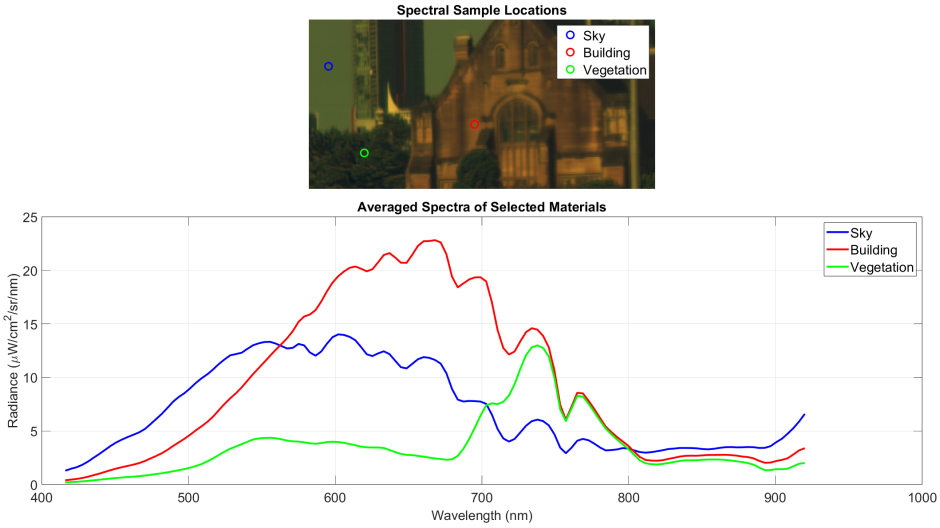

Figure 6.12: Selected areas of the datacube spatial scene and their corresponding spectra. The spectra correspond to an approximate red (building), blue (sky) and green (vegetation) profile. Spectra are presented as at-sensor radiance (μW/cm^2/sr/nm) as a calibrated reference target was not present in this scene.

and corresponding radiance characteristics in the visible and near-infrared range. Areas of shadow also produce higher contrast due to noise effects. This highlights a known limitation of NDVI, where spectral ambiguity between vegetation and certain man-made materials can lead to classification errors in the absence of more detailed spectral examination.

Spectral Characterisation of Vegetation

The spectral radiance profiles of a few chosen areas of foliage were examined, to further test the application-readiness of the device. These data patches were chosen manually from an area of the image, and contain the spectrum of a 5x5 averaged square of pixels, as seen in Figure 6.16. The data exhibited characteristic features of healthy green vegetation:

- Visible Spectrum (400–700 nm): Absorption in the blue (~450 nm) and red (~670 nm) wavelengths due to chlorophyll pigments, with a peak in the green (~550 nm) region are visible, signifying typical green colouration to foliage.
- Red Edge (700–750 nm): A sharp increase in radiance, marking the transition from chlorophyll absorption to strong NIR radiance, is indicative of healthy plant tissue.
- Near-Infrared Region (750–900 nm): The radiance profile beyond 750 nm shows a pronounced dip around 760 nm, followed by a gradual decline extending toward 900 nm. This spectral pattern is consistent with the influence of atmospheric absorption features commonly encountered in field-collected hyperspectral imagery. In particular, the sharp decrease near 760 nm corresponds to the oxygen-A absorption band, a well-documented feature of atmo-

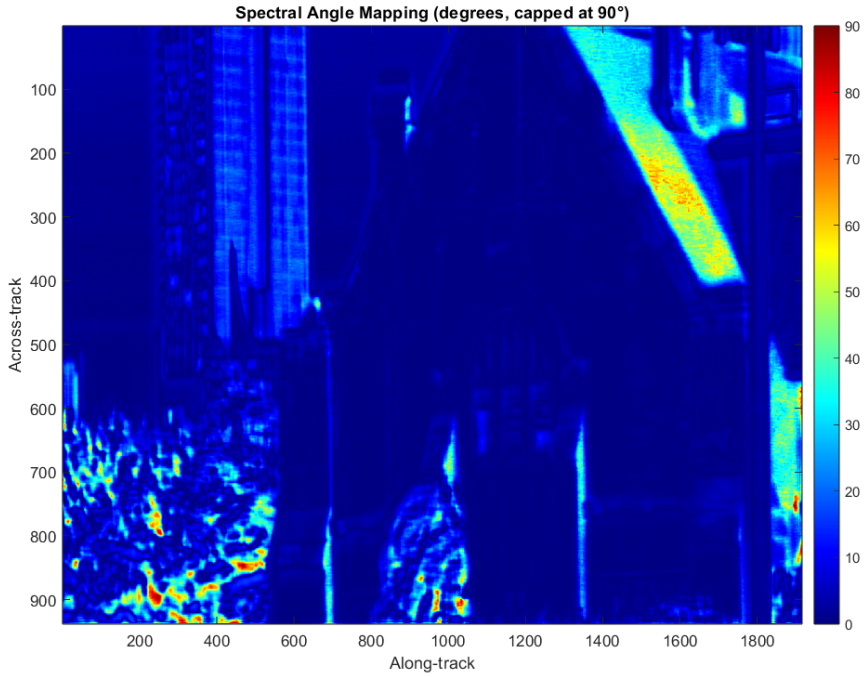

Figure 6.13: SAM image showing spectral shift observed due to pansharpening across the spatial domain.

spheric transmittance [4], [121].

- Upper IR limit (>900 nm): At the IR edge of the detector there is an increase in signal, that can be attributed to second-order diffraction effects from the grating. High-intensity radiance from the blue spectral region (450–460 nm) create a constructive interference ghost signal at double the wavelength (900–920 nm) [122]. This artifact is reinforced in Figure 6.12, where the blue sky spectrum shows a more pronounced rise at 900 nm than the vegetation and building spectra. As the current optical design does not incorporate an order-sorting filter for simplicity, radiometric data in this region should be considered qualitative only without digital correction.

These atmospheric effects are evident in the presented dataset due to the absence of atmospheric correction during preprocessing. While these absorption features can distort spectral shape, their presence is expected under field conditions and should be accounted for in future application-driven testing. For practical use in environmental or agricultural monitoring, the implementation of atmospheric correction models (e.g., MODTRAN or empirical line methods) would be necessary to recover accurate surface radiance. Nevertheless, the overall form of the spectrum, including the distinct red edge rise and elevated NIR radiance, remains characteristic of healthy vegetation. These findings suggest that the uncorrected data still retains robust physiological information for spectral analysis.

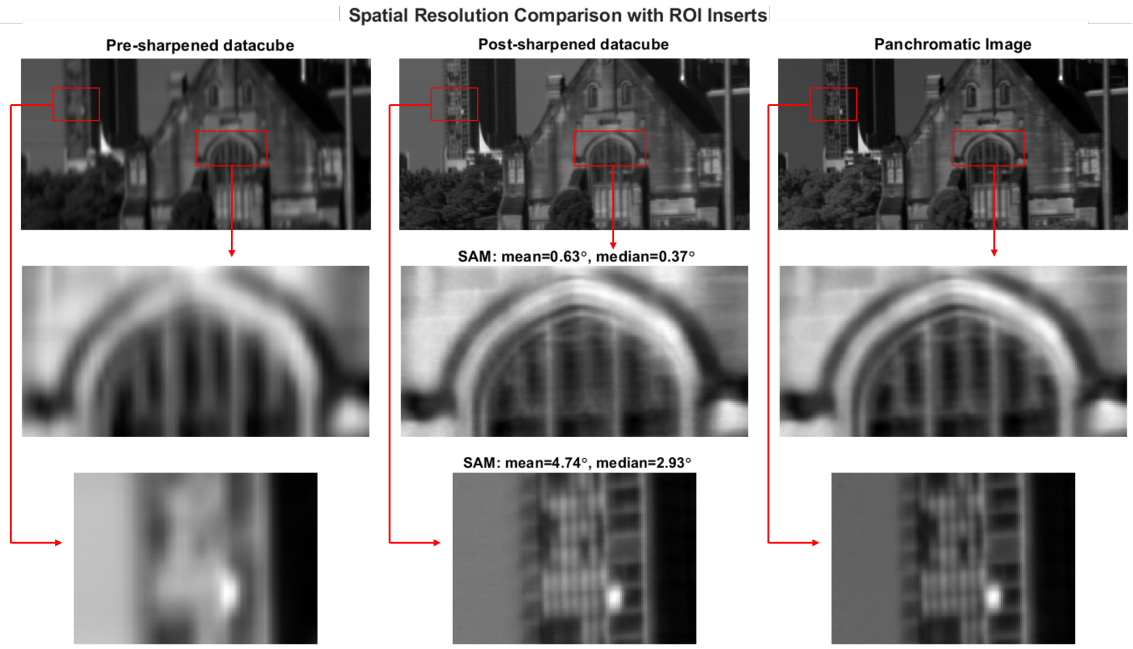

Figure 6.14: Spatial contrast ROI comparison between the captured datacube, sharpened datacube, and the panchromatic image used for pansharpening. Regions of increased contrast in the sharpened datacube are shown alongside SAM values for the same ROI for validation of spectral integrity.

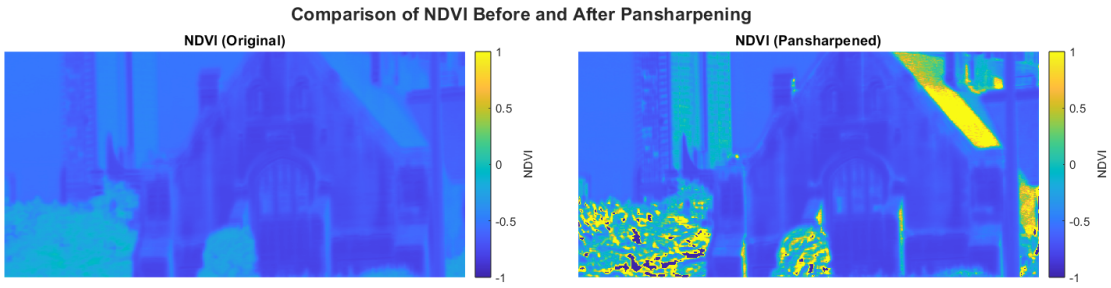

Figure 6.15: NDVI vegetation highlighted results showing increased capability in detection.

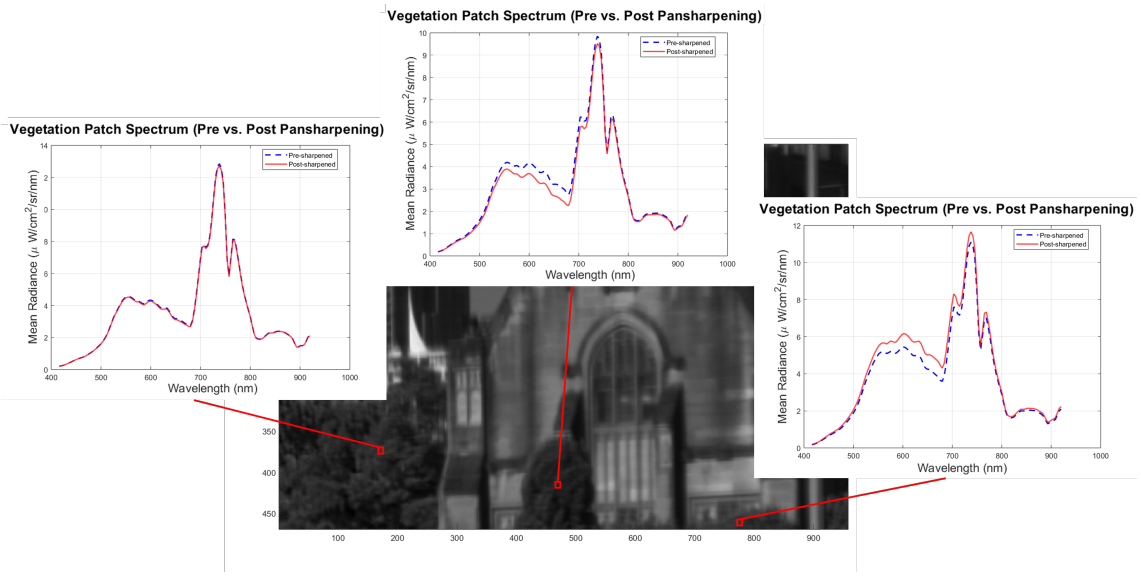

Figure 6.16: The spectral signature of 3 areas of vegetation from the datacube scene showing the minimal shift in spectrum after pansharpening. Median SAM values for these patches were 0.95° (left), 2.79° (middle) and 2.61° (right).

6.4 Targeted Hyperspectral Imaging via 3D Rotational Systems

This section outlines a proposed operational framework where the dual-modality system is deployed to solve the efficiency bottlenecks of traditional pushbroom scanning. The dual-modality imaging approach presented throughout this thesis opens avenues for advancements beyond traditional imaging scenarios. One compelling application area for this technology lies in its integration with multi-axis rotational imaging platforms, akin to the 3D rotational optical systems developed by companies such as Ocular Robotics.

These multi-axis rotational stages are tailored to fit consumer hyperspectral imagers, but lack the advanced scene-scanning capabilities of a co-aligned high-resolution imaging detector. Pairing these two technologies allows the panchromatic imagery to act as a real-time ”viewfinder” for the spectrometer. For targeting, an area or object of interest can be identified with initial high-speed spatial scanning, before activating the hyperspectral spectrometer and acquiring detailed spectral datacubes of specific regions.

The high-resolution panchromatic imaging capability significantly reduces the time required for scanning and locating regions of interest, a particularly important advantage in dynamic environments or fast-acquisition scenarios. Furthermore, by limiting hyperspectral imaging exclusively to pre-identified targets, data acquisition time and computational load are dramatically reduced. In relation to the research presented in this thesis, the integration of dual-modality imaging with 3D rotational stages represents a logical extension of the technology developed here.

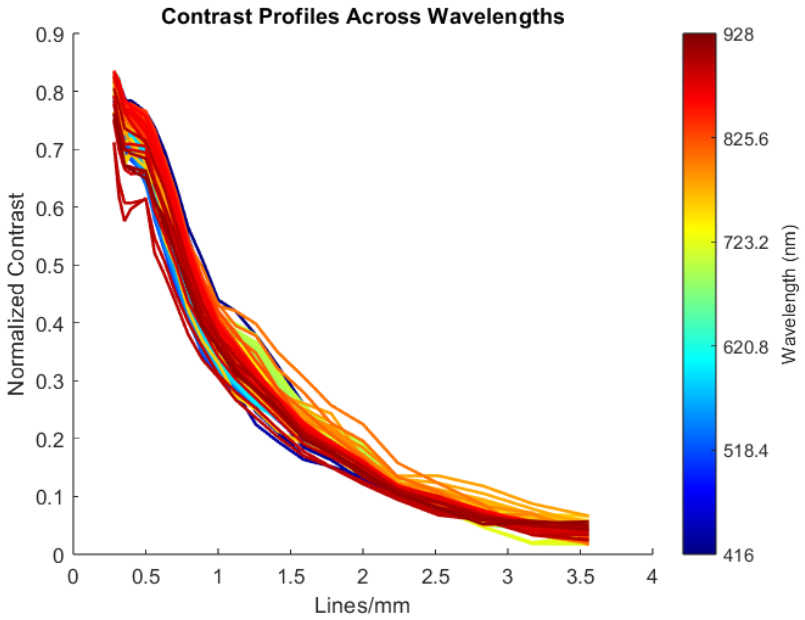

Figure 6.17: MTF of datacube sharpened per-band to one panchromatic image.

6.5 Multi-spectral enhancement of hyperspectral data

In order to further push the spatial resolution enhancement from the pansharpening process, several alternate strategies for applying the Gram-Schmidt Adaptive (GSA) algorithm were investigated. One approach was to sharpen the datacube on a per-band basis, applying GSA sequentially to each of the 130 wavelength bins using the same panchromatic image. This method was analogous to synthetic multispectral sharpening strategies used by some research groups to validate fusion algorithms on satellite hyperspectral data[31]. The resulting spatial contrast improvement appeared to arise from the differential weighting of spatial features, particularly in spectral bands with lower signal-to-noise ratios.

Figure 6.17 shows the MTF analysis of a USAF target acquired under this regime, where enhancement across the spectral range is clearly evident when compared with Figure 6.7. This is shown in the tightened dispersion of MTF lines across the wavelength range, and collective ”flattening” of the curves toward the ideal. However, this gain in spatial performance came at the cost of spectral integrity. The effect was not immediately obvious in USAF target captures, as their spectra are essentially binary across the wavelength range (white-black image targets). When applied to real-world imagery, however, the method produced severe spectral degradation. As illustrated in Figure 6.18, the “by-chunk to PAN” approach introduced artificial peaks and troughs, resulting in spectral signatures unsuitable for feature recognition.

To address this limitation, a modified capture strategy was attempted. Rather than relying on a single broadband panchromatic image, a multispectral panchromatic image stack was constructed by capturing nine high-resolution images through band-pass filters mounted in front of the telescopic lens. This approach aimed to provide

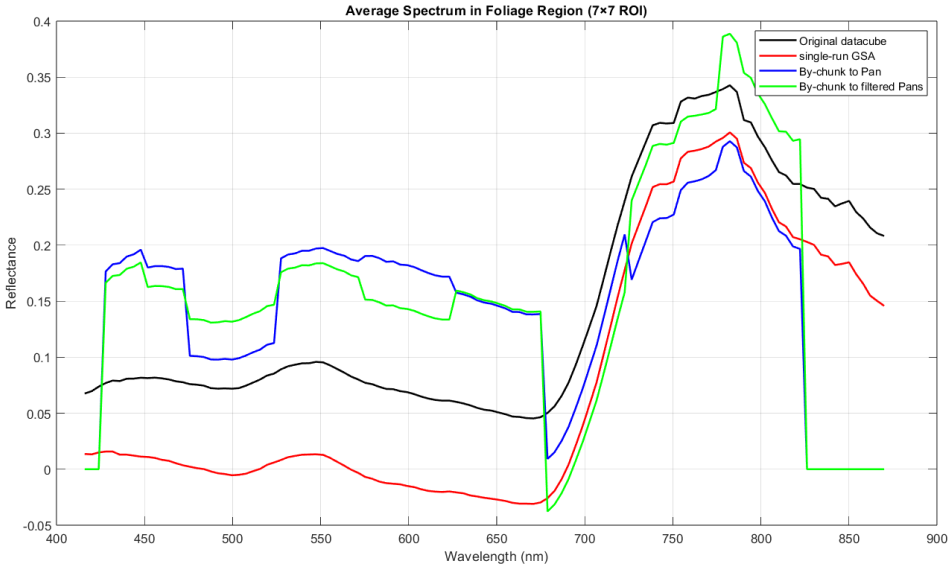

Figure 6.18: Spectrum of a foliage ROI comparing different pansharpening approaches

band-specific spatial detail for sharpening the hyperspectral cube in nine larger chunks, with the goal of reducing spectral distortion while keeping spatial gains. Thorlabs 40 nm FWHM hard-coated VIS-NIR filters were employed, covering the range 416–870 nm. A custom optical rig, shown in Figure 6.19, was assembled for sequential panchromatic image acquisition. The hyperspectral datacube was also truncated to match the filter coverage. As can be seen in Figure 6.18, this method yielded promising signal reflectance values, however similar distortion, especially at filter boundaries was observed.

This spectral distortion was attributed to the limited flexibility of the GSA algorithm, and the further development of this imaging technique would require more complex, possibly machine-learning trained data fusion. This research avenue, along with more advanced pansharpening application is discussed further in Section 7.1.

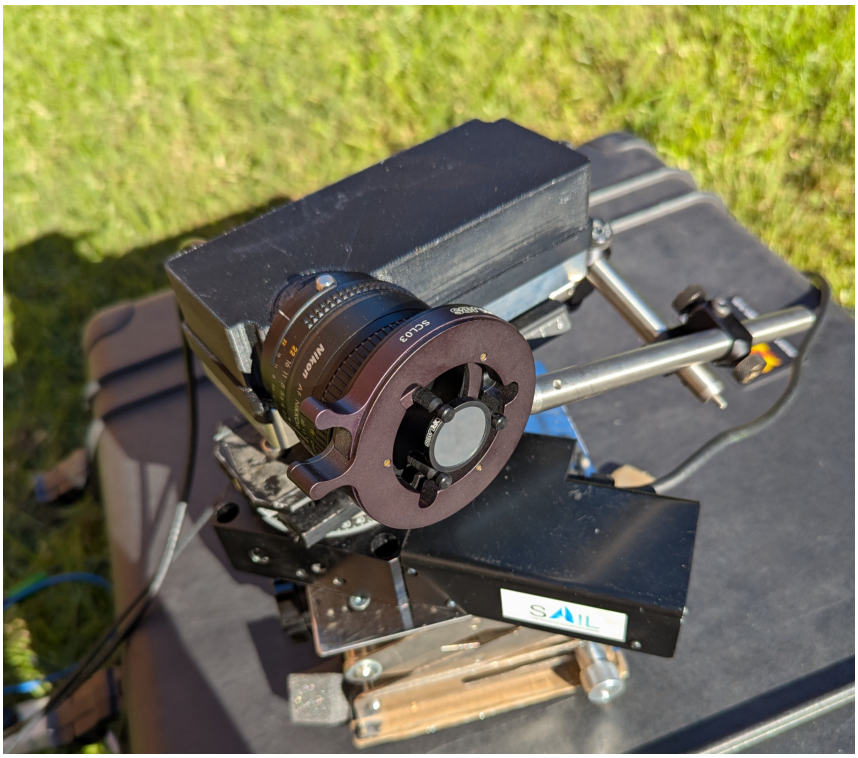

Figure 6.19: Multi-spectral panchromatic image capture setup showing the small circular filter held in place in front of the field lens.

Chapter 7

Conclusion

This thesis set out to address the fundamental limitation of spatial anisotropy in compact hyperspectral imagers. Pushbroom spectrometers, while efficient in photon throughput and spectral fidelity, inherently produce datacubes with unbalanced resolution: across-track sampling is defined by detector geometry with the slit, while along-track sampling depends on platform motion and exposure time among others. Commercial instruments can minimise this issue with custom optics and high-end detectors, but their cost and integration requirements place them beyond the reach of many research groups. The aim of this work was therefore to demonstrate intra-device pansharpening as a practical strategy to combat these spatial-spectral trade-offs, enabling compact and accessible systems to deliver datacubes with improved spatial isotropy.

To pursue this aim, three major contributions were made to form the core chapters of this research. First, optical design was examined through Zemax simulations of both a throughput-optimised theoretical model and a low-cost redesign of the open-source OpenHSI. The "custom" model was designed without the limitation of commercially-available components and demonstrated much improved photon throughput alongside a significant improvement of 92% theoretical contrast at the detector limit. The COTS (commercial-off-the-shelf) redesign then notably delivered more uniform spot confinement across the wavelength range and length of the slit, and comparable theoretical MTF spatial performance. Second, mechanical integration of the COTS model was designed around the dual-detector functionality, enabling the simultaneous capture of hyperspectral and panchromatic data. This design preserved compactness while integrating the co-aligned dual-arm layout, ensuring that both modalities shared the same field of view. This model was then calibrated for wavelength and radiance standardisation, and baseline datacubes captured for data-enhancement-benchmarking. Third, a complete data-processing pipeline was implemented, spanning raw datacube capture, image co-registration, and Gram-Schmidt Adaptive (GSA) pansharpening. A "virtual-camera" interface was developed alongside the OpenHSI software package, to allow higher bitrate captures demanded by fast exposure times. Analysis was performed over the pansharpened datacubes to verify the quantitative contrast improvement via MTF inspection, and application-driven assessment alongside spectral consistency measures.

Through a range of approaches, the device design and ideology was verified. Quan-

titative spatial resolution evaluation on a USAF contrast target revealed that the intra-device pansharpening had increased the modulation transfer function normalised area under the curve (AUC) from 0.262 to 0.340 (∼30% increase). Alongside this, the contrast at the finest resolvable spatial frequency (48 lp/mm) improved from 0.0258 to 0.0472 (∼83% increase) demonstrating gains in contrast retention and resolvable detail. Anisotropy between across- and along-track sampling was reduced, with the sharpened datacubes showing more balanced spatial fidelity across the scene. Spectral preservation was then validated by ERGAS (8.24), SAM (median 1.47°, mean 6.03°), and NDVI consistency (mean increase from 0.379 to 0.402 with improved delineation of vegetation boundaries). These values align with thresholds widely regarded as strong performance, confirming that spatial gains were achieved at little cost to spectral integrity. Qualitative scene analyses reinforced these results, showing sharper delineation of foliage, urban structures, and fine features critical to ecological and environmental monitoring.

The contributions of this work are twofold. Technically, it demonstrates the feasibility of intra-device pansharpening in a compact, reproducible hyperspectral system, bridging the gap between high-performance commercial imagers and low-cost open hardware. It also provides a framework for balancing manufacturability, accessibility, and performance: design compromises in optics and mechanics can be offset by fusion-based post-processing. Together, these advances extend the reach of hyperspectral imaging to small-team research contexts, UAV platforms, and resource-constrained applications.

7.1 Future Work

Several directions for future work arise naturally. Mechanically, integration with targeting systems could further optimise acquisition efficiency, enabling selective hyperspectral capture guided by live panchromatic scans. The device described here was designed with future iterations in mind for installation inside a robotic tracking telescope assembly, allowing real-time video tracking using the panchromatic detector. This added modality would allow full scene scanning before target confirmation, where the hyperspectral imaging device could be engaged for pushbroom-sweep capture. This application pushes the bounds of traditional hyperspectral imaging to a far more real-time scenario. In addition to this adaptation was a proposed method to improve throughput of both imaging modalities, by use of a beam-switching mirror to be deployed via mechanism inside the device. This mechanism could be engaged manually when switching between imaging modes to ensure 100% of incoming light could be used for each detector. GPU-accelerated or embedded implementations of GSA and learning-based methods could open the door to real-time sharpening in UAV deployment. As part of this optical redesign, an order filter could also be added to physically remove the artifact in the >900 nm region of the detector. Alternatively a correction for this signal could be added to the data processing pipeline, as outlined in the ”Removing Second Order Diffraction Effects” chapter of the Mao thesis[122]. Finally, expanded validation across field testing, including vegetation surveys, aquatic monitoring, and built-environment mapping, would benchmark performance against commercial instruments and under diverse conditions.

Deep-learning trained pansharpening models have proven to achieve significant re-

sults over older, simpler algorithms such as GSA. HyperPNN[94] and other convolutional neural network (CNN) models have found remarkable results in datacube sharpening, by training deep learning models. Groups such as Guarino et al.[95] have proposed simplified model-trained methods using un-supervised pansharpening that show sharp qualitative contrast improvement alongside low SAM scores ($>4°$). Methods like these are either trained or weighted with coefficients from aerial-view datasets and as such were difficult to implement within the bounds of this research. This also represents a clear future motive to apply the device in UAV flight, where aerial-view trained algorithms can be applied to practically captured data.

Finally, advanced sharpening techiques were briefly explored in this thesis through the use of band-pass filtered panchromatic images to create a high-resolution proxy multispectral stack. Fusing these images with hyperspectral datacubes showed promise in enhancing contrast but introduced significant spectral artefacts. Data fusion of multispectral and hyperspectral data has been reported, with newer machine-learning algorithms proving strong data enhancement[123]. Applying these more advanced models, and in-house training of unsupervised models could be adapted to fit these datasets and preserve spectral integrity.

In summary, this thesis has shown that intra-device pansharpening is a viable and effective strategy for overcoming spatial anisotropy in compact hyperspectral imagers. By integrating optical, mechanical, and computational design, it establishes a pathway for creating accessible instruments that deliver both spectral fidelity and enhanced spatial resolution at low cost. The approach offers not only a practical tool for small research teams, but also a broader paradigm for coupling open hardware with computational enhancement to democratise advanced imaging capabilities.

References

[1] J. R. Irons, J. L. Dwyer, and J. A. Barsi, "The next landsat satellite: The landsat data continuity mission," *Remote Sensing of Environment*, vol. 122, pp. 11–21, 2012, Landsat Legacy Special Issue. DOI: 10.1016/j.rse.2011.08.026.

[2] G. Vane, A. F. H. Goetz, and J. B. Wellman, "Airborne imaging spectrometer: A new tool for remote sensing," *IEEE Transactions on Geoscience and Remote Sensing*, vol. GE-22, no. 6, pp. 546–549, 1984. DOI: 10.1109/TGRS.1984.6499168.

[3] R. O. Green, M. L. Eastwood, C. M. Sarture, *et al.*, "Imaging spectroscopy and the airborne visible/infrared imaging spectrometer (aviris)," *Remote Sensing of Environment*, vol. 65, no. 3, pp. 227–248, 1998. DOI: 10.1016/S0034-4257(98)00064-9.

[4] A. Goetz, G. Vane, J. Solomon, and B. Rock, "Imaging spectrometry for earth remote sensing," *Science*, vol. 228, no. 4704, pp. 1147–1153, 1985. DOI: 10.1126/science.228.4704.1147.

[5] D. Wang, Z. Chen, X. Zhang, *et al.*, "A high optical throughput spectral imaging technique using broadband filters," *Sensors*, vol. 20, no. 16, 2020, ISSN: 1424-8220. DOI: 10.3390/s20164387.

[6] J. A. Richards and X. Jia, *Remote Sensing Digital Image Analysis*, 4th ed. Springer, 1986. DOI: 10.1007/3-540-29711-1.

[7] R. A. Schowengerdt, *Remote Sensing, Models and Methods for Image Processing*, 3rd ed. Academic Press, 2007. DOI: 10.1016/B978-0-12-369407-2.X5000-1.

[8] B.-C. Gao, M. J. Montes, C. O. Davis, and A. F. H. Goetz, "Atmospheric correction algorithms for hyperspectral remote sensing data of land and ocean," *Remote Sensing of Environment*, vol. 113, no. S1, S17–S24, 2009. DOI: 10.1016/j.rse.2007.12.015.

[9] C.-I. Chang, *Hyperspectral Imaging: Techniques for Spectral Detection and Classification*. Springer, 2003. DOI: 10.1007/978-1-4419-9170-6.

[10] F. D. van der Meer and S. M. De Jong, *Imaging Spectrometry: Basic Principles and Prospective Applications*. Springer, 2001. DOI: 10.1007/978-0-306-47578-8.

[11] A. M. Melesse, Q. Weng, P. S. Thenkabail, and G. B. Senay, "Remote sensing sensors and applications in environmental resources mapping and modelling," *Sensors*, vol. 7, no. 12, pp. 3209–3241, 2007. DOI: 10.3390/s7123209.

[12] F. Sigernes, M. Syrjäsuo, R. Storvold, J. Fortuna, M. E. Grøtte, and T. A. Johansen, "Do it yourself hyperspectral imager for handheld to airborne op-

erations," *Optics Express*, vol. 26, no. 5, pp. 6021–6035, 2018. DOI: 10.1364/OE.26.006021.

[13] P. S. Thenkabail, R. B. Smith, and E. De Pauw, "Hyperspectral vegetation indices and their relationships with agricultural crop characteristics," *Remote Sensing of Environment*, vol. 71, no. 2, pp. 158–182, 2000. DOI: 10.1016/S0034-4257(99)00067-X.

[14] M. B. Stuart, A. J. S. McGonigle, and J. R. Willmott, "Hyperspectral imaging in environmental monitoring: A review of recent developments and technological advances in compact field deployable systems," *Sensors*, vol. 19, no. 14, p. 3071, 2019. DOI: 10.3390/s19143071.

[15] G. Lu and B. Fei, "Medical hyperspectral imaging: A review," *Journal of Biomedical Optics*, vol. 19, no. 1, p. 010 901, 2014. DOI: 10.1117/1.JBO.19.1.010901.

[16] P. Mouroulis, R. O. Green, and T. G. Chrien, "Design of pushbroom imaging spectrometers for optimum recovery of spectroscopic and spatial information," *Applied Optics*, vol. 39, no. 13, pp. 2210–2220, 2000. DOI: 10.1364/AO.39.002210.

[17] Z. Wang, H. Li, S. Wang, L. Song, and J. Chen, "Methodology and modeling of uav push-broom hyperspectral brdf observation considering illumination correction," *Remote Sensing*, vol. 16, no. 3, 2024, ISSN: 2072-4292. DOI: 10.3390/rs16030543.

[18] J. R. Jensen, *Remote Sensing of the Environment: An Earth Resource Perspective*, 2nd ed. Prentice Hall, 2007.

[19] P. Mouroulis, R. O. Green, and T. G. Chrien, "Optical design of a compact imaging spectrometer for planetary mineralogy," *Optical Engineering*, vol. 46, no. 6, F85–F93, 2008. DOI: 10.1117/1.2749499.

[20] M. T. Eismann, *Hyperspectral Remote Sensing*. SPIE Press, 2012. DOI: 10.1117/3.899758.

[21] P. S. Thenkabail, J. G. Lyon, and A. Huete, *Hyperspectral remote sensing of vegetation*. Boca Raton: CRC Press, 2012, ISBN: 978-1-4398-4537-0. DOI: 10.1201/b11222.

[22] A. Plaza, J. A. Benediktsson, J. W. Boardman, *et al.*, "Recent advances in techniques for hyperspectral image processing," *Remote Sensing of Environment*, vol. 113, no. S1, S110–S122, 2009. DOI: 10.1016/j.rse.2007.07.028.

[23] A. Rogalski, "Infrared detectors: Status and trends," *Progress in Quantum Electronics*, vol. 27, pp. 59–210, 2 2003. DOI: 10.1016/S0079-6727(02)00024-1.

[24] Headwall Photonics, "Nano-hyperspec datasheet," Headwall Photonics, Tech. Rep., 2018, Product datasheet. [Online]. Available: https://www.polytec.com/fileadmin/website/optical-systems/spezialkameras/pdf/PH_HWP_NanoHyperspec_VNIR_0118.pdf.

[25] Y. Mao, C. H. Betters, B. Evans, *et al.*, "Openhsi: a complete open-source hyperspectral imaging solution for everyone," *Remote Sensing*, vol. 14, no. 9, p. 2244, 2022. DOI: 10.3390/rs14092244.

[26] P. S. Chavez, S. C. Sides, and J. A. Anderson, "Comparison of three different methods to merge multiresolution and multispectral data: Landsat tm and spot panchromatic," *Photogrammetric Engineering and Remote Sensing*, vol. 57, no. 3, pp. 295–303, 1991.

[27] L. Wald, "Some terms of reference in data fusion," *IEEE Transactions on Geoscience and Remote Sensing*, vol. 37, no. 3, pp. 1190–1193, 1999. DOI: 10.1109/36.763269.

[28] T.-M. Tu, S.-C. Su, H.-C. Shyu, and P. S. Huang, "A new look at IHS-like image fusion methods," *Information Fusion*, vol. 2, no. 3, pp. 177–186, 2001. DOI: 10.1016/S1566-2535(01)00036-7.

[29] I. Amro, J. Mateos, M. Vega, R. Molina, and A. K. Katsaggelos, "A survey of classical methods and new trends in pansharpening of multispectral images," *EURASIP Journal on Advances in Signal Processing*, vol. 2011, no. 79, pp. 1–22, 2011. DOI: 10.1186/1687-6180-2011-79.

[30] G. Vivone, L. Alparone, J. Chanussot, *et al.*, "A critical comparison among pansharpening algorithms," *IEEE Transactions on Geoscience and Remote Sensing*, vol. 53, no. 5, pp. 2565–2586, 2015. DOI: 10.1109/TGRS.2014.2361734.

[31] L. Loncan, L. B. de Almeida, J. M. Bioucas-Dias, *et al.*, "Hyperspectral pansharpening: A review," *IEEE Geoscience and Remote Sensing Magazine*, vol. 3, no. 5, pp. 27–46, 2015. DOI: 10.1109/MGRS.2015.2440094.

[32] G. Masi, D. Cozzolino, L. Verdoliva, and G. Scarpa, "Pansharpening by convolutional neural networks," *Remote Sensing*, vol. 8, no. 7, p. 594, 2016. DOI: 10.3390/rs8070594.

[33] X. Meng, H. Shen, H. Li, L. Zhang, and R. Fu, "Review of the pansharpening methods for remote sensing images based on the idea of meta-analysis: Practical discussion and challenges," *Information Fusion*, vol. 46, pp. 102–113, 2019. DOI: 10.1016/j.inffus.2018.05.006.

[34] A. Lowe, N. Harrison, and A. P. French, "Hyperspectral image analysis techniques for the detection and classification of the early onset of plant disease and stress," *Plant Methods*, vol. 13, p. 80, 2017. DOI: 10.1186/s13007-017-0233-z.

[35] Y. Wang, N. Reder, S. Kang, A. Glaser, and J. Liu, "Multiplexed optical imaging of tumor-directed nanoparticles: A review of imaging systems and approaches," *Nanotheranostics*, vol. 1, pp. 369–388, Aug. 2017. DOI: 10.7150/ntno.21136.

[36] N. Hagen and M. W. Kudenov, "Review of snapshot spectral imaging technologies," *Optical Engineering*, vol. 52, no. 9, p. 090 901, 2013. DOI: 10.1117/1.OE.52.9.090901.

[37] M.-F. Cheng, A. Mukundan, R. Karmakar, M. A. E. Valappil, J. Jouhar, and H.-C. Wang, "Modern trends and recent applications of hyperspectral imaging: A review," *Technologies*, vol. 13, no. 5, p. 170, 2025. DOI: 10.3390/technologies13050170.

[38] J. J. Sousa, P. Toscano, A. Matese, *et al.*, "Uav-based hyperspectral monitoring using push-broom and snapshot sensors: A multisite assessment for precision viticulture applications," *Sensors*, vol. 22, no. 17, p. 6574, 2022. DOI: 10.3390/s22176574.

[39] N. Gat, "Imaging spectroscopy using tunable filters: A review," in *Wavelet Applications VII*, ser. Proceedings of SPIE, SPIE, vol. 4056, 2000, pp. 50–64. DOI: 10.1117/12.381686.

[40] C. Royer, C. Pilorget, V. Hamm, J.-P. Bibring, and F. Poulet, "A new concept of acousto-optic tunable filter-based near-infrared hyperspectral imager

for planetary surface exploration," *Review of Scientific Instruments*, vol. 93, no. 4, p. 044 501, 2022. DOI: 10.1063/5.0075256.

[41] J. S. Pearlman, S. Barry, C. Segal, J. Shepanski, D. Beiso, and S. L. Carman, "Hyperion, a space-based imaging spectrometer," *IEEE Transactions on Geoscience and Remote Sensing*, vol. 41, no. 6, pp. 1160–1173, 2003. DOI: 10.1109/TGRS.2003.815018.

[42] Z. Jiang, Z. Yu, Y. Yu, Z. Huang, Q. Ren, and C. Li, "Spatial resolution enhancement for pushbroom-based microscopic hyperspectral imaging," *Applied Optics*, vol. 58, no. 4, pp. 850–862, 2019. DOI: 10.1364/AO.58.000850.

[43] G. Gamez, D. Frey, and J. Michler, "Push-broom hyperspectral imaging for elemental mapping with glow discharge optical emission spectrometry," *Journal of Analytical Atomic Spectrometry*, vol. 27, no. 1, pp. 50–55, 2012. DOI: 10.1039/C1JA10241A.

[44] X. Prieto-Blanco, C. Montero-Orille, B. Couce, and R. de la Fuente, "Analytical design of an offner imaging spectrometer," *Optics Express*, vol. 14, no. 20, pp. 9156–9168, 2006. DOI: 10.1364/OE.14.009156.

[45] T. Rasmussen, "The benefits of transmission grating based spectroscopy," Ibsen Photonics A/S, White Paper Version 1.0, 2010. DOI: 10.22184/1993-7296.2017.64.4.50.59.

[46] *Transmission gratings*, Accessed: 2025-09-26, Edmund Optics, 2025. [Online]. Available: https://www.edmundoptics.com/f/transmission-gratings/13496/.

[47] *Reflective ruled diffraction gratings*, Accessed: 2025-09-26, Edmund Optics, 2025. [Online]. Available: https://www.edmundoptics.com/f/Reflective-Ruled-Diffraction-Gratings/12220/.

[48] K. M. Harrison, "Prisms, gratings and spectroscopes," in *Astronomical Spectroscopy for Amateurs*. New York, NY: Springer New York, 2011, pp. 35–44, ISBN: 978-1-4419-7239-2. DOI: 10.1007/978-1-4419-7239-2_4.

[49] Specim, Spectral Imaging Ltd., *Smile and keystone*, https://www.specim.com/smile-and-keystone/, Accessed: 26 September 2025, 2021.

[50] W. Bakker, H. van der Werff, and F. van der Meer, "Determining smile and keystone of lab hyperspectral line cameras," in *2019 10th Workshop on Hyperspectral Imaging and Signal Processing: Evolution in Remote Sensing (WHISPERS)*, IEEE, Amsterdam, Netherlands, 2019, pp. 1–5. DOI: 10.1109/WHISPERS.2019.8921045.

[51] J. M. Bioucas-Dias, A. Plaza, G. Camps-Valls, P. Scheunders, N. Nasrabadi, and J. Chanussot, "Hyperspectral remote sensing data analysis and future challenges," *IEEE Geoscience and Remote Sensing Magazine*, vol. 1, no. 2, pp. 6–36, 2013. DOI: 10.1109/MGRS.2013.2244672.

[52] E. J. Hochberg and M. J. Atkinson, "Capabilities of remote sensors to classify coral, algae, and sand as pure and mixed spectra," *Remote Sensing of Environment*, vol. 85, no. 2, pp. 179–189, 2003. DOI: 10.1016/S0034-4257(02)00202-X.

[53] D. Z.-Y. Ting, A. Soibel, L. Höglund, *et al.*, "Type-ii superlattice infrared detectors," in *Semiconductors and Semimetals*, vol. 84, Elsevier, 2011, pp. 1–57. DOI: 10.1016/B978-0-12-381337-4.00001-2.

[54] B.-L. Hu, S.-J. Hao, D.-X. Sun, and Y.-N. Liu, "A novel scene-based non-uniformity correction method for swir push-broom hyperspectral sensors,"

ISPRS Journal of Photogrammetry and Remote Sensing, vol. 131, pp. 160–169, 2017, ISSN: 0924-2716. DOI: 10.1016/j.isprsjprs.2017.08.004.

[55] S. Yamamoto, S. Tsuchida, M. Urai, H. Mizuochi, K. Iwao, and A. Iwasaki, "Initial analysis of spectral smile calibration of hyperspectral imager suite (hisui) using atmospheric absorption bands," *IEEE Transactions on Geoscience and Remote Sensing*, vol. 60, pp. 1–13, 2022. DOI: 10.1109/TGRS.2022.3190486.

[56] Y. Angel, D. Turner, S. D. Parkes, Y. Malbeteau, A. Lucieer, and M. F. McCabe, "Automated georectification and mosaicking of uav-based hyperspectral imagery from push-broom sensors," *Remote Sensing*, vol. 12, no. 1, p. 34, 2019. DOI: 10.3390/rs12010034.

[57] Specim, Spectral Imaging Ltd., "Aisafenix technical datasheet," Specim, Spectral Imaging Ltd., Tech. Rep., 2020, Product datasheet. [Online]. Available: https://www.specim.com/wp-content/uploads/2020/03/AisaFENIX-ver1-2020.pdf.

[58] Specim, Spectral Imaging Ltd., "Specim fx10 technical datasheet," Specim, Spectral Imaging Ltd., Tech. Rep., 2024, Product datasheet. [Online]. Available: https://www.specim.com/wp-content/uploads/2024/06/Specim-FX10-Technical-Datasheet-08.pdf.

[59] Headwall Photonics, "Micro-hyperspec swir-640 datasheet," Headwall Photonics, Tech. Rep., 2023, Product datasheet. [Online]. Available: https://headwallphotonics.sharefile.com/share/view/sd72591b3b714490d8edbc25cf6c96071.

[60] BaySpec Inc., "Oci-1000/2000 hyperspectral camera datasheet," BaySpec Inc., Tech. Rep., 2022, Product datasheet. [Online]. Available: https://www.bayspec.com/wp-content/uploads/2022/12/New-BaySpec-Datasheet-OCI-1000-2000-Hyperspectral-Camera-.pdf.

[61] M. B. Henriksen, E. F. Prentice, C. M. van Hazendonk, F. Sigernes, and T. A. Johansen, "Do-it-yourself vis/nir pushbroom hyperspectral imager with c-mount optics," *Optics Continuum*, vol. 1, no. 2, pp. 427–441, 2022. DOI: 10.1364/OPTCON.450693.

[62] W.-Q. Chang, H.-Y. Hou, P.-Y. Li, *et al.*, "Hyper spectral camera analyzer (hyperscan)," *Remote Sensing*, vol. 17, no. 5, 2025. DOI: 10.3390/rs17050842.

[63] K. Salesin, D. Seyb, S. Friday, and W. Jarosz, "Diy hyperspectral imaging via polarization-induced spectral filters," in *IEEE International Conference on Computational Photography (ICCP)*, 2022, pp. 1–12. DOI: 10.1109/ICCP54855.2022.9887696.

[64] E. M. Pechlivani, A. Papadimitriou, S. Pemas, N. Giakoumoglou, and D. Tzovaras, "Low-cost hyperspectral imaging device for portable remote sensing," *Instruments*, vol. 7, no. 4, p. 32, 2023. DOI: 10.3390/instruments7040032.

[65] A. Moghimi, C. Yang, and J. A. Anderson, "Aerial hyperspectral imagery and deep neural networks for high-throughput yield phenotyping in wheat," *Computers and Electronics in Agriculture*, vol. 172, p. 105 299, 2020, ISSN: 0168-1699. DOI: 10.1016/j.compag.2020.105299.

[66] K. Nagasubramanian, S. Jones, S. Sarkar, A. K. Singh, and B. Ganapathysubramanian, "Hyperspectral band selection using genetic algorithm and support vector machines for early identification of charcoal rot disease in soybean

stems," *Plant Methods*, vol. 14, no. 1, p. 86, 2018. DOI: 10.1186/s13007-018-0349-9.

[67] J. Salazar-Vazquez and A. Mendez-Vazquez, "A plug-and-play hyperspectral imaging sensor using low-cost equipment," *HardwareX*, vol. 7, e00087, 2019. DOI: 10.1016/j.ohx.2019.e00087.

[68] M. L. Clark, D. A. Roberts, and D. B. Clark, "Hyperspectral discrimination of tropical rain forest tree species at leaf to crown scales," *Remote Sensing of Environment*, vol. 96, no. 3, pp. 375–398, 2005. DOI: 10.1016/j.rse.2005.03.009.

[69] F. E. Fassnacht, H. Latifi, K. Stereńczak, *et al.*, "Review of studies on tree species classification from remotely sensed data," *Remote Sensing of Environment*, vol. 186, pp. 64–87, 2016. DOI: 10.1016/j.rse.2016.08.013.

[70] H. Aasen, E. Honkavaara, A. Lucieer, and P. J. Zarco-Tejada, "Quantitative remote sensing at ultra-high resolution with uav spectroscopy: A review of sensor technology, measurement procedures, and data correction workflows," *Remote Sensing*, vol. 10, no. 7, p. 1091, 2018. DOI: 10.3390/rs10071091.

[71] S. R. Phinn, C. Roelfsema, A. G. Dekker, and V. E. Brando, "Mapping seagrass species, cover and biomass in shallow waters: An assessment of satellite multispectral and airborne hyperspectral data imaging systems in moreton bay (australia)," *Remote Sensing of Environment*, vol. 112, no. 8, pp. 3413–3425, 2008. DOI: 10.1016/j.rse.2007.09.017.

[72] E. J. Hochberg, M. J. Atkinson, and S. Andrefouet, "Spectral reflectance of coral reef bottom-types worldwide and implications for coral reef remote sensing," *Remote Sensing of Environment*, vol. 85, no. 2, pp. 159–173, 2003. DOI: 10.1016/S0034-4257(02)00201-8.

[73] C. Laukamp, T. Cudahy, J. S. Cleverley, N. H. Oliver, and R. Hewson, "Airborne hyperspectral imaging of hydrothermal alteration zones in granitoids of the eastern fold belt, mount isa inlier, australia," *Geochemistry: Exploration, Environment, Analysis*, vol. 11, no. 1, pp. 3–24, 2011. DOI: 10.1144/1467-7873/09-231.

[74] E. Bedini, "Mapping lithology of the sarfartoq carbonatite complex, southern west greenland, using hymap imaging spectrometer data," *Remote Sensing of Environment*, vol. 113, no. 6, pp. 1208–1219, 2009. DOI: 10.1016/j.rse.2009.02.007.

[75] HyVista Corporation, *Hymap™ airborne hyperspectral scanner*, https://hyvista.com/, Accessed: 29 September 2025, 2024.

[76] D. Krupnik and S. Khan, "Close-range, ground-based hyperspectral imaging for mining applications at various scales: Review and case studies," *Earth-Science Reviews*, vol. 198, p. 102 952, 2019. DOI: 10.1016/j.earscirev.2019.102952.

[77] L. Ptacek, A. Strauss, B. Hinterstoisser, and A. Zitek, "Curing assessment of concrete with hyperspectral imaging," *Materials*, vol. 14, no. 14, p. 3848, 2021. DOI: 10.3390/ma14143848.

[78] J. K. Delaney, J. G. Zeibel, M. Thoury, *et al.*, "Visible and infrared imaging spectroscopy of paintings and improved reflectography," *Applied Spectroscopy*, vol. 64, no. 6, pp. 584–594, 2010. DOI: 10.1186/s40494-016-0075-4.

[79] C. Cucci, J. K. Delaney, and M. Picollo, "Reflectance hyperspectral imaging for investigation of works of art: Old master paintings and illuminated manuscripts," *Accounts of Chemical Research*, vol. 49, no. 10, pp. 2070–2079, 2016. DOI: 10.1021/acs.accounts.6b00048.

[80] R. Leon, B. Martinez-Vega, H. Fabelo, *et al.*, "Non-invasive skin cancer diagnosis using hyperspectral imaging for in-situ clinical support," *Journal of Clinical Medicine*, vol. 9, no. 6, p. 1662, 2020. DOI: 10.3390/jcm9061662.

[81] M. A. Calin, S. V. Parasca, D. Savastru, and D. Manea, "Hyperspectral imaging in the medical field: Present and future," *Applied Spectroscopy Reviews*, vol. 49, no. 6, pp. 435–447, 2014. DOI: 10.1080/05704928.2013.838678.

[82] J. Xing and J. De Baerdemaeker, "Bruise detection on 'jonagold' apples using hyperspectral imaging," *Postharvest Biology and Technology*, vol. 37, no. 2, pp. 152–162, 2005. DOI: 10.1016/j.postharvbio.2005.02.015.

[83] M. Kamruzzaman, Y. Makino, and S. Oshita, "Non-invasive analytical technology for the detection of contamination, adulteration, and authenticity of meat, poultry, and fish – a review," *Food Control*, vol. 72, pp. 255–266, 2016. DOI: 10.1016/j.aca.2014.08.043.

[84] R. Bacon, M. Accardo, L. Adjali, *et al.*, "The muse second-generation vlt instrument," *Proc. SPIE*, vol. 7735, p. 773 508, 2010. DOI: 10.1117/12.856027.

[85] S. Murchie, R. Arvidson, P. Bedini, *et al.*, "Compact reconnaissance imaging spectrometer for mars (crism) on mars reconnaissance orbiter (mro)," *Journal of Geophysical Research: Planets*, vol. 112, no. E5, 2007. DOI: 10.1029/2006JE002682.

[86] A. Garzelli, F. Nencini, L. Alparone, B. Aiazzi, and S. Baronti, "Pan-sharpening of multispectral images: A critical review and comparison," in *IGARSS 2004. 2004 IEEE International Geoscience and Remote Sensing Symposium*, vol. 1, 2004, p. 84. DOI: 10.1109/IGARSS.2004.1368950.

[87] B. Aiazzi, L. Alparone, S. Baronti, A. Garzelli, and M. Selva, "Mtf-tailored multiscale fusion of high-resolution ms and pan imagery," *Photogrammetric Engineering & Remote Sensing*, vol. 72, no. 5, pp. 591–596, 2006. DOI: 10.14358/PERS.72.5.591.

[88] G. Dial, H. Bowen, F. Gerlach, J. Grodecki, and R. Oleszczuk, "Ikonos satellite, imagery, and products," *Remote Sensing of Environment*, vol. 88, no. 1, pp. 23–36, 2003, IKONOS Fine Spatial Resolution Land Observation, ISSN: 0034-4257. DOI: 10.1016/j.rse.2003.08.014.

[89] Y. Ke, L. J. Quackenbush, and J. Im, "Synergistic use of quickbird multispectral imagery and lidar data for object-based forest species classification," *Remote Sensing of Environment*, vol. 114, no. 6, pp. 1141–1154, 2010, ISSN: 0034-4257. DOI: 10.1016/j.rse.2010.01.002.

[90] R. Molina, M. Vega, J. Mateos, and A. K. Katsaggelos, "Bayesian and regularization methods for hyperparameter estimation in image restoration," *IEEE Transactions on Image Processing*, vol. 8, no. 2, pp. 231–246, 1999. DOI: 10.1109/83.743857.

[91] Q. Wei, N. Dobigeon, and J.-Y. Tourneret, "Bayesian fusion of hyperspectral and multispectral images," in *2014 IEEE International Conference on Acoustics, Speech and Signal Processing (ICASSP)*, IEEE, 2014. DOI: 10.1109/ICASSP.2014.6854186.

[92] G. Scarpa, S. Vitale, and D. Cozzolino, "Target-adaptive cnn-based pansharpening," *IEEE Transactions on Geoscience and Remote Sensing*, vol. 56, no. 9, pp. 5443–5457, 2018. DOI: 10.1109/TGRS.2018.2817393.

[93] J. Yang, X. Fu, Y. Hu, Y. Huang, X. Ding, and J. Paisley, "Pannet: A deep network architecture for pan-sharpening," in *2017 IEEE International Conference on Computer Vision (ICCV)*, 2017, pp. 1753–1761. DOI: 10.1109/ICCV.2017.193.

[94] L. He, J. Zhu, J. Li, A. Plaza, J. Chanussot, and B. Li, "Hyperpnn: Hyperspectral pansharpening via spectrally predictive convolutional neural networks," *IEEE Journal of Selected Topics in Applied Earth Observations and Remote Sensing*, vol. PP, pp. 1–9, Jun. 2019. DOI: 10.1109/JSTARS.2019.2917584.

[95] G. Guarino, M. Ciotola, G. Vivone, and G. Scarpa, "Band-wise hyperspectral image pansharpening using cnn model propagation," *IEEE Transactions on Geoscience and Remote Sensing*, pp. 1–1, 2023. DOI: 10.1109/TGRS.2023.3339337.

[96] B. Aiazzi, L. Alparone, S. Baronti, and A. Garzelli, "Context-driven fusion of high spatial and spectral resolution images based on oversampled multiresolution analysis," *IEEE Transactions on Geoscience and Remote Sensing*, vol. 40, no. 10, pp. 2300–2312, 2002. DOI: 10.1109/TGRS.2002.803623.

[97] B. Aiazzi, L. Alparone, S. Baronti, and A. Garzelli, "Improving component substitution pansharpening through multivariate regression of ms+pan data," *IEEE Transactions on Geoscience and Remote Sensing*, vol. 45, no. 10, pp. 3230–3239, 2007. DOI: 10.1109/TGRS.2007.901007.

[98] G. Sech, G. Poggi, M. Ljubenovic, M. Fiorucci, and A. Traviglia, "Pansharpening of prisma products for archaeological prospection," in *IGARSS 2024 - 2024 IEEE International Geoscience and Remote Sensing Symposium*, IEEE, 2024. DOI: 10.1109/IGARSS53475.2024.10642261.

[99] J. Gilbertson, J. Kemp, and A. van Niekerk, "Effect of pan-sharpening multi-temporal landsat 8 imagery for crop type differentiation using different classification techniques," English, *Computers and Electronics in Agriculture*, vol. 134, pp. 151–159, Mar. 2017. DOI: 10.1016/j.compag.2016.12.006.

[100] M. Perretta, G. Delogu, C. Funsten, A. Patriarca, E. Caputi, and L. Boccia, "Testing the impact of pansharpening using prisma hyperspectral data: A case study classifying urban trees in naples, italy," *Remote Sensing*, vol. 16, no. 19, 2024, ISSN: 2072-4292. DOI: 10.3390/rs16193730.

[101] D. Abriha, Z. Kovács, S. Ninsawat, L. Bertalan, B. Bertalan-Balazs, and S. Szabo, "Identification of roofing materials with discriminant function analysis and random forest classifiers on pan-sharpened worldview-2 imagery – a comparison," *Hungarian Geographical Bulletin*, vol. 67, pp. 375–392, Dec. 2018. DOI: 10.15201/hungeobull.67.4.6.

[102] P. Trevisiol, E. Tarantino, S. Pagliara, and L. Bruzzone, "An object-oriented approach to the classification of roofing materials from very high resolution satellite images," *Remote Sensing*, vol. 14, no. 4, p. 849, 2022. DOI: 10.3390/rs14040849.

[103] G. Guarino, M. Ciotola, G. Poggi, G. Vivone, and G. Scarpa, "Hybrid gsa-cnn method for hyperspectral pansharpening," in *IGARSS 2024 - 2024 IEEE*

International Geoscience and Remote Sensing Symposium, 2024, pp. 901–904. DOI: 10.1109/IGARSS53475.2024.10641593.

[104] I. S. Helfenstein, F. D. Schneider, M. E. Schaepman, and F. Morsdorf, "Assessing biodiversity from space: Impact of spatial and spectral resolution on trait-based functional diversity," *Remote Sensing of Environment*, vol. 275, p. 113 024, 2022, ISSN: 0034-4257. DOI: 10.1016/j.rse.2022.113024.

[105] Z. Hu, Y. Chu, Y. Zhang, *et al.*, "Scale matters: How spatial resolution impacts remote sensing based urban green space mapping?" *International Journal of Applied Earth Observation and Geoinformation*, vol. 134, p. 104 178, 2024, ISSN: 1569-8432. DOI: 10.1016/j.jag.2024.104178.

[106] L. Alparone, B. Aiazzi, S. Baronti, A. Garzelli, F. Nencini, and M. Selva, "Multispectral and panchromatic data fusion assessment without reference," *Photogrammetric Engineering & Remote Sensing*, no. 2, pp. 193–200, 2008. DOI: 10.14358/PERS.74.2.193.

[107] "Iso 12233:2024 digital cameras — resolution and spatial frequency responses," International Organization for Standardization, Geneva, Switzerland, Tech. Rep. ISO 12233:2024, 2024, Published September 2024. Reference number: 88626. [Online]. Available: https://www.iso.org/standard/88626.html.

[108] L. R., A. C., R. Guarini, E. Lopinto, C. L., and A. R. Pisani, "The prisma hyperspectral mission," May 2016.

[109] D. Cerra, D. Marshall, U. Heiden, *et al.*, "The spaceborne imaging spectrometer desis: Data access, outreach activities, and scientific applications," in *IGARSS 2022 - 2022 IEEE International Geoscience and Remote Sensing Symposium*, 2022, pp. 5395–5398. DOI: 10.1109/IGARSS46834.2022.9883119.

[110] M. L. Henriksen, J.-C. Pedersen, B. B. E. Jensen, B. Jørgensen, R. L. Eriksen, and M. Hinge, "A direct comparison of a next generation hyperspectral camera to state-of-the-art," *Spectrochimica Acta Part A: Molecular and Biomolecular Spectroscopy*, vol. 325, p. 125 068, 2025, ISSN: 1386-1425. DOI: 10.1016/j.saa.2024.125068.

[111] N. Koren, "Correcting misleading image quality measurements," *Electronic Imaging*, vol. 2020, pp. 242–1, Jan. 2020. DOI: 10.2352/ISSN.2470-1173.2020.9.IQSP-242.

[112] F. Kruse, A. Lefkoff, J. Boardman, *et al.*, "The spectral image processing system (sips)—interactive visualization and analysis of imaging spectrometer data," *Remote Sensing of Environment*, vol. 44, no. 2, pp. 145–163, 1993. DOI: 10.1016/0034-4257(93)90013-N.

[113] Thorlabs Inc., *Broadband VIS-NIR Anti-Reflection Coatings*, https://www.thorlabs.com/newgrouppage9.cfm?objectgroup_id=5840, 2024.

[114] Thorlabs, Inc., *Gr25-0610 600 lines/mm ruled reflective diffraction grating*, https://www.thorlabs.com, 600 lines/mm, 25×25 mm soda-lime grating, blaze 1000 nm, 2025.

[115] H. Bay, T. Tuytelaars, and L. Van Gool, "Surf: Speeded up robust features," in *Computer Vision – ECCV 2006*, A. Leonardis, H. Bischof, and A. Pinz, Eds., Berlin, Heidelberg: Springer Berlin Heidelberg, 2006, pp. 404–417.

[116] E. Rublee, V. Rabaud, K. Konolige, and G. Bradski, "Orb: An efficient alternative to sift or surf," in *2011 International Conference on Computer Vision*, 2011, pp. 2564–2571. DOI: 10.1109/ICCV.2011.6126544.

[117] P. F. Alcantarilla, A. Bartoli, and A. J. Davison, "Kaze features," in *Computer Vision – ECCV 2012*, A. Fitzgibbon, S. Lazebnik, P. Perona, Y. Sato, and C. Schmid, Eds., Berlin, Heidelberg: Springer Berlin Heidelberg, 2012, pp. 214–227. DOI: 10.1007/978-3-642-33783-3_16.

[118] A. V. Oppenheim, R. W. Schafer, and J. R. Buck, *Discrete-Time Signal Processing*, 2nd. Upper Saddle River, NJ: Prentice Hall, 1999.

[119] M. Unser, "Splines: A perfect fit for signal and image processing," *IEEE Signal Processing Magazine*, vol. 16, no. 6, pp. 22–38, 1999. DOI: 10.1109/79.799930.

[120] L. Wald, T. Ranchin, and M. Mangolini, "Fusion of satellite images of different spatial resolutions: Assessing the quality of resulting images," *Photogrammetric Engineering and Remote Sensing*, vol. 63, pp. 691–699, Nov. 1997.

[121] R. Clark, G. Swayze, A. Gallagher, T. King, and W. Calvin, "Imaging spectroscopy: Earth and planetary remote sensing with the usgs tetracorder and expert systems," *Journal of Geophysical Research: Planets*, vol. 108, no. E12, p. 5131, 2003. DOI: 10.1029/2002JE001847.

[122] Y. Mao, "Open-source imaging spectroscopy for the remote sensing practitioner: From instrumentation to new applications," PhD Thesis, The University of Sydney, Sydney, Australia, May 2024.

[123] G. Vivone, "Multispectral and hyperspectral image fusion in remote sensing: A survey," *Information Fusion*, vol. 89, pp. 405–417, 2023, ISSN: 1566-2535. DOI: 10.1016/j.inffus.2022.08.032.